UNIVERSITY OF CALIFORNIA, SAN DIEGO

# An Extensive Analysis of Modified Nanotube Surfaces for Next-Generation Orthopedic Implants

A dissertation submitted in partial satisfaction of the
requirements for the degree
Doctor of Philosophy

in

Materials Science and Engineering

by

Christine Jeanette Frandsen

Committee in charge:

Professor Sungho Jin, Chair
Professor Jennifer Cha
Professor Ratnesh Lal
Professor Vlado Lubarda
Professor Joanna McKittrick

2012

The Dissertation of Christine Jeanette Frandsen is approved, and it is acceptable in quality and form for publication on microfilm and electronically:

---

---

---

---

---

Chair

University of California, San Diego

2012

## DEDICATION

*To my husband, Allen, for encouraging me every step of the way.*

*I could not have done it without you.*

*And to my parents, for teaching me (among countless other things)*

*to love math and science.*

## EPIGRAPH

*"Always bear in mind that your own resolution to succeed is more important than any other."*

-Abraham Lincoln

*"Education is an admirable thing, but it is well to remember from time to time that nothing that is worth knowing can be taught."*

-Oscar Wilde

"*Genius is 1 percent inspiration and 99 percent perspiration."*

-Thomas A. Edison

## TABLE OF CONTENTS

## LIST OF FIGURES

## ACKNOWLEDGEMENTS

I am sincerely grateful to many people who made the work herein possible. First and foremost I would like to thank my advisor, Professor Sungho Jin. From the first time I met him, he believed in my potential as a Ph.D. candidate. Without his guidance and support, I would not be here today. I also owe a debt of gratitude to my mentor, colleague, and friend Dr. Karla (Brammer) Khalifa, who taught, inspired and encouraged me along the way.

I am also deeply indebted to all of my colleagues from the Jin Group; in particular, Dr. Seunghan (Brian) Oh, Dr. Kunbae (Kevin) Noh, Laura Connelly, Gary Johnston, and Dr. Chulmin (Edward) Choi. I am happy to have shared many moments of laboratory research, insightful discussions, and collaborative projects with you all. I would also like to give special thanks to Charlotte Lauve, Jennifer Church, and J.V. Agnew of the MAE department, and Ryan Anderson of Nano3 (CalIT$^2$) for doing their jobs so well, and for their helpfulness throughout the years.

I am very grateful for all of my friends outside of UCSD who have helped me to enjoy life in San Diego and to keep focused on what really matters. In addition, I am especially grateful for my family: Mom and Dad, Christal and Will (and Liam!), Christopher, and Christianne. I am proud to be a member of a family of nerdy, intelligent engineers, mathematicians,

and health professionals! I'm glad to be able to share things about my research with you and not receive blank stares, but enthusiasm and interest! Thank you, Mom & Dad, for teaching me the value of education, hard work, and persistence. Most of all, I am thankful for my best friend and husband, Allen, who from the very start motivated me, encouraged me, did my laundry, made me dinner, went to the lab with me if I had a late experiment, and never tired of hearing about my research. Thank you for keeping me going!

Chapter 2 is a reprint in part of the material as it has been submitted to *The Role of Biomaterials for Regenerative Medicine* (submitted in response to invitation, June 2012) written by Christine J. Frandsen, Karla S. Brammer, and Sungho Jin. The dissertation author is a collaborating investigator and first author of the publication.

Chapter 3 is a reprint in part of the material as it appears in *Materials Science & Engineering C* Volume 31 (8), 2011, Page 1716 written by Christine J. Frandsen, Karla S. Brammer, Kunbae Noh, Laura S. Connelly, Seunghan Oh, Li-Han Chen, and Sungho Jin. The dissertation is the primary investigator and author of this publication.

Chapter 4, section 1 contains a reprint in part of the material as it appears in *Acta Biomaterialia* Volume 7 (6), 2011, Page 2697 written by Karla S. Brammer, Chulmin Choi, Christine J. Frandsen, Seunghan Oh, Gary

Johnston, and Sungho Jin. The dissertation author is a collaborating investigator and author of this publication. Chapter 4, section 2 contains a reprint in part of the material as it has been prepared for submission for publication, written by Christine J. Frandsen, Karla S. Brammer, Kunbae Noh, Gary W. Johnston, and Sungho Jin. The dissertation author is the primary investigator and author of this publication. Chapter 4, section contains a reprint in part of the material as it has been prepared for submission for publication, written by Christine J. Frandsen, Karla S. Brammer, Gary W. Johnston, Chulmin Choi, and Sungho Jin. The dissertation author is the primary investigator and author of this publication.

Chapter 5, section 1 contains a reprint in part of the material as it has been prepared for submission for publication, written by Christine J. Frandsen, Kunbae Noh, Karla S. Brammer, and Sungho Jin. The dissertation author is the primary investigator and author of this publication. Chapter 5, section 2 contains a reprint in part of the material as it has been prepared for submission for publication, written by Jiahua Ni, Christine J. Frandsen, Kunbae Noh, Gary W. Johnston, Guo He, Tingting Tang, and Sungho Jin. The dissertation author is the primary collaborating investigator and author of this publication.

Lastly, I would like to show appreciation to the financial support of this research by UC Discovery/Kinamed Grant No. ele08-128656/Jin, K. Iwama Endowed Chair fund, Powell Fellowship, and the ARCS Foundation. In particular, a special thank you to Mr. Clyde Pratt of Kinamed, Inc. for showing interest and support for the Jin Lab biomaterials research, for insightful discussions, and for providing the femoral knee implants utilized in Chapter 5 of this dissertation.

## VITA

2007 Bachelor of Science in Chemical Engineering,

University of California, Santa Barbara

2008 Master of Science in Materials Science and Engineering,

University of California, San Diego

2012 Doctor of Philosophy in Materials Science and Engineering,

University of California, San Diego

Emphasis in Nano/Biomaterials

## PUBLICATIONS AND PATENTS

CJ Frandsen, KS Brammer, GW Johnston, C Choi, S Jin. "In vitro analysis of oxidized and metallic tantalum coatings on $TiO_2$ nanotubes in terms of human osteoblast function." (In preparation)

CJ Frandsen, KS Brammer, K Noh, GW Johnston, S Jin. "Tantalum coating on $TiO_2$ nanotubes induces superior rate of matrix mineralization and osteofunctionality." (In preparation)

J Ni, CJ Frandsen, K Noh, GW Johnston, G He, T Tang, S Jin. "Fabrication of thin film $TiO_2$ nanotube arrays on Co-28Cr-6Mo alloy by anodization." (In preparation)

CJ Frandsen, K Noh, KS Brammer, S Jin. "Hybrid micro-/nano-topography of a $TiO_2$ nanotube-coated commercial zirconia femoral knee implant promotes bone cell adhesion in vitro." (In preparation)

CJ Frandsen, KS Brammer, S Jin. "Variations to the nanotube surface for bone regeneration." Invited Review by *The Role of Biomaterials for Regenerative Medicine*. (Submitted, June 2012).

J Ni, K Noh, CJ Frandsen, et al. "Preparation of near micrometer-sized $TiO_2$ nanotube arrays by high voltage anodization." (Submitted to *Materials Science & Engineering C*, May 2012)

KS Brammer, CJ Frandsen, S Jin. "$TiO_2$ nanotubes for bone regeneration." Invited Review by *Trends in Biotechnology*. 2012 June; 30(6).

J Khamwannah, SY Noh, CJ Frandsen, et al. "Nanocomposites of $TiO_2$ and double-walled carbon nanotubes for improved dye-sensitized solar cells." *Journal of Renewable and Sustainable Energy*. 2012 Apr; 4(023116).

J Khamwannah, Y Zhang, SY Noh, H Kim, CJ Frandsen, SD Kong, S Jin. "Enhancement of dye sensitized solar cell efficiency by composite $TiO_2$ nanoparticle/8 nm $TiO_2$ nanotube paper-like photoelectrode." *Nano Energy*. 2012 Mar; 1(3).

CJ Frandsen, KS Brammer, K Noh, L Connelly, LH Chen, and S Jin. "Zirconium oxide nanotube surface prompts increased osteoblast functionality and mineralization." *Materials Science and Engineering: C*. 2011 Dec; 31(8).

K Noh, KS Brammer, C Choi, SH Kim, CJ Frandsen, and S Jin. "A new nano-platform for drug release via nanotubular aluminum oxide." *J. of Biomater. and Nanobiotech*. 2011 Jul; 2(3).

KS Brammer, C Choi, CJ Frandsen, S Oh, G Johnston, S Jin. "Comparative cell behavior on carbon coated $TiO_2$ nanotube surfaces for osteoblasts and vs. osteo-progenitor cells" *Acta Biomater*. 2011 Jun; 7(6).

KS Brammer, SH Kim, CJ Frandsen, et al. "Novel 8nm $TiO_2$ nanotube fibers elicit enhanced bone cell response." *Advanced Biomater*. 2011 Mar; 13(3).

KS Brammer, C Choi, CJ Frandsen, S Oh, and S Jin. "Hydrophobic nanopillars initiate mesenchymal stem cell aggregation and osteo-differentiation." *Acta Biomater*. 2011 Feb; 7(2).

KS Brammer, S Oh, CJ Frandsen, S Jin. Invited Book Chapter "Biomaterials and biotechnology schemes utilizing $TiO_2$ nanotube arrays." *Biomaterials Science & Engineering*. Ed. Rosario Pignatello. InTech, 2011.

KS Brammer, S Oh, CJ Cobb, and S Jin. Invited Book Chapter "Enhanced cell growth, function, and differentiation by $TiO_2$ nanotube surface

structuring." *Nanotechnology in Tissue Engineering and Regenerative Medicine*. Ed. Ketul C. Popat. Taylor & Francis Group, LLC, 2011.

CS Rustomji, CJ Frandsen, S Jin, MJ Tauber. "Dye-sensitized solar cell constructed with titanium mesh and 3-D array of $TiO_2$ nanotubes," *J. Phys. Chem. B*. 2010 Jun; Article ASAP.

KS Brammer, S Oh, CJ Frandsen, and S Jin. "$TiO_2$ nanotube structures for enhanced cell and biological functionality," *JOM*. 2010 Apr; 62(4).

KS Brammer, S Oh, CJ Frandsen, S Varghese, and S Jin. "Nanotube surface triggers increased chondrocyte extracellular matrix production," *Mater. Sci. Eng. C*. 2010 Jan; 30(4).

KS Brammer, C Choi, S Oh, CJ Cobb, et al. "Antibiofouling, sustained antibiotic release by Si nanowire templates," *Nano Lett*. 2009 Oct; 9(10).

KS Brammer, S Oh, CJ Cobb, et al. "Improved bone-forming functionality on diameter-controlled $TiO_2$ nanotube surface," *Acta Biomater*. 2009 Oct; 5(8).

S Oh, KS Brammer, CJ Cobb et al. Invited Book Chapter "$TiO_2$ nanotubes for enhanced cell and bone growth." *Recent developments in advanced medical and dental materials using electrochemical methodologies*. Ed. RL Karlinsey. Research Signpost, 2009.

NA Fichtenbaum, C Schaake, TE Mates, C Cobb, S Keller, SP DenBaars, UK Mishra. "Electrical characterization of p-type N-polar and Ga-polar GaN grown by metalorganic chemical vapor deposition," *Appl. Phys. Lett*. 2007 Oct; 91(17).

S Jin and C Frandsen. "Products of manufacture having tantalum coated nanostructures, and methods of making and using them," United States Provisional Patent, No. 61/596,143.

S Jin, MJ Tauber, C Frandsen, C Rustomji. "Three dimensional dye-sensitized solar cells with nanoscale architectures," United States Patent, No. 13/263,745.

A Hampp and C Cobb. "The application of a self-assembled monolayer as an indium oxide inhibitor", United States Patent, No. 2009062334.

E Smith and C Cobb. "Self-aligned photolithography for simplified focal plane array (FPA) fabrication", Raytheon Patent Evaluation Committee reviewed and rated as Trade Secret Invention Disclosure, No. 06W116.

## ABSTRACT OF THE DISSERTATION

### An Extensive Analysis of Modified Nanotube Surfaces for Next-Generation Orthopedic Implants

By

Christine Jeanette Frandsen

Doctor of Philosophy in Materials Science and Engineering

University of California, San Diego, 2012

Professor Sungho Jin, Chair

The biological response to implant materials has been a topic of extensive research and discussion throughout the years. More recently, the field has become particularly exciting due to advances in nanotechnology, and the indications and belief that living cells sense and respond to cues on the nanoscale. A nanostructured material of special interest for orthopedic implant applications is the vertically aligned, laterally spaced titanium oxide ($TiO_2$) nanotube arrays formed via

electrochemical anodization techniques. Foundational work in the Jin Lab has demonstrated the advantages of the $TiO_2$ nanotube surface due to indications that the nanotube architecture significantly accelerates osteoblast cell growth [1], improves bone-forming functionality [2], and even directs mesenchymal stem cell fate [3]. However, these findings raise questions such as whether the same nano-architecture can be equally effective when exhibiting different surface chemistries. In addition, the feasibility of fabricating the nanotube structure from a thin film of titanium on the surface of an orthopedic implant composed of another material as a bioactive coating has been uncertain. The work reviewed in this dissertation attempts to answer these questions by providing in-depth experimental analysis of (a) comparative osteogenic behavior on nanotube surfaces of varying surface chemistries including $ZrO_2$, $TiO_2$, Ta, and $Ta_2O_5$, and (b) optimized anodization parameters for thin film $TiO_2$ nanotube layers applied to industry-supplied orthopedic implant materials (i.e. zirconia and CoCr alloy), and initial osteoblast cell response to such coatings. The research of this dissertation conveys substantial contributions towards the field of orthopedic surface technology, and for furthered understanding of cellular interactions with complex nano-interfaces.

# CHAPTER 1

# 1. Introduction

## 1.1 Characteristics and Function of Normal Bone

Bone is a complex tissue that has the ability to heal and regenerate itself [4], and is continuously in the cycle of remodeling from before birth until death [5]. The process of bone modeling and remodeling typically occurs to help the bone adapt to mechanical forces or to replace microdamaged bone with new, stronger bone [5]. Bone modeling is the process of new bone formation due to physiological influences and mechanical forces, which usually occurs in adolescents. The remodeling of bone occurs in adults more than in children, and is the process in which old bone is removed and new bone is formed in order to maintain bone strength and mineral homeostasis.

The process of bone remodeling is composed of four distinct phases: activation, resorption, reversal, and formation [5]. Each of these phases is a result of complex physiological and cellular reactions, which have been briefly described here for the purpose of giving a basic understanding of bone remodeling. During the activation phase, osteoclast precursors are recruited and activated, leading to the resorption phase. Osteoclasts are responsible for resorbing (breaking down) bone during the resorption phase. The cycle is then reversed

(reversal phase) when monocytes and osteocytes are released from bone matrix and begin to recruit pre-osteoblasts. Lastly, new bone is formed by osteoblasts which synthesize new collagenous organic matrix and regulate mineralization of matrix. The process of bone formation takes approximately 4 to 6 months to complete [5].

Occasionally bone defects will form that are unable to heal on their own, either due to bone disease or trauma. In these cases, bone reconstruction is necessary, which requires osteoproduction (colonization of osteogenic stem cells at defect site), osteoinduction (induced bone formation), osteoconduction (growth of bone on a surface), osseointegration (stable anchorage of an implant achieved by direct bone-to-implant contact), mechanical stimulation, and vascularization [4, 6-7]. In many cases an orthopedic (bone) implant is needed in order to stabilize the defect and provide support for new bone to grow.

## The Clinical Need for Improved Orthopedic Implants

Although current technology in the field of orthopedic implants is highly advanced when compared to even 20 years ago, there remains to be room for improvement. To date, an estimated 5-15 % of bone implant (including dental and orthopedic) failures still occur, causing pain and frustration with the patient when the need for revision surgery is realized [8]. In addition, the average bone implant lifetime is less than 15 years [9].

The need for improved orthopedic materials surfaces is well-recognized by patients, surgeons, and researchers alike, especially for young patients who will outlive their orthopedic implants by many years, thus requiring multiple revision surgeries throughout their lives.

There are many causes for bone implant failure, such as:

- Insufficient initial bone growth on the implant surface
- Production of wear debris at the articulating surface, which becomes lodged between the implant and surrounding tissue, leading to cell death
- Imbalanced stress and strain between the implant and surrounding tissue, leading to implant loosening and fracture [9]

These modes of failure are no doubt a result of combined issues, likely sometimes including poor patient bone quality, which prevents the ability of the bone to securely interlock into the implant. However, as was suggested by Sato & Webster [9], by designing an implant material surface that stimulates rapid bone regeneration, thus filling any voids or deficiencies at the bone-implant interface, many of these problems could be overcome. Additionally, if bone tissue was able to quickly form a secure connection with the implant surface, there would be less chance for bone cell death as a result of wear debris, since there would be no spaces for debris particles to accumulate.

## 1.2 The Evolution of Biomedical Materials Technology

The technology and design of materials for bone implants have evolved tremendously over the past 50 years, through what Hench, et al. defines as three generations of biomedical materials [10]. First-generation biomedical materials were developed in the 1960s and 1970s, for which the main goal was to "achieve a suitable combination of physical properties to match those of the replaced tissue with a minimal toxic response in the host" [10]. The most important feature of biomaterials then was their biological inertness (minimum immune response to the foreign material), and this is still an extremely valuable requirement today. In general, biomaterials were traditionally designed to *macroscopically* match the properties of the tissue into which they would be implanted [11].

In the late 70s to early 80s, the focus of biomaterials design shifted from solely a bioinert tissue response to include a bioactive tissue response which would trigger a controlled reaction *in vivo* [10]. Bioactive materials reached clinical use by the mid-1980s for orthopedic and dental applications, including bioactive glasses, ceramics, and composites [10]. Resorbable biomaterials (which dissolve into the body) were also introduced to the market, and resorbable polymer sutures became routinely used. At this point, biomaterials properties were beginning to be

designed to match the body tissue at the microscale. The bioinert, bioactive, and resorbable implants have provided great success in clinical practice over the years, and remain to be the basis of many biomaterials in use today. However, the life-expectancy of our population has increased considerably in recent decades, and the U.S. is presented with a growing population of elderly with diminished bone regeneration capacity [12]. One-third to one-half of current orthopedic implant prostheses are said to fail within 10 to 25 years of implantation, requiring revision surgery [10]. Although substantial progress has been made in the area of orthopedic materials, the failure rates of such implants have not been significantly improved.

As the search continues for an orthopedic implant technology that provides a stable osseointegration that out-lives the patient, the third generation of biomaterials has evolved. The aim of third-generation biomaterials is that the material is designed in such a way that it would stimulate certain cellular responses at the *molecular* level [10]. By modifying the surfaces at the molecular and nanoscale levels, researchers have been able to direct cell proliferation, differentiation, and extracellular matrix (ECM) production and organization [10].

## 1.3 Engineering the Cell-Surface Interface

One of the most critical factors for bone implant success is implant stability at the interface. A loose bone implant at any stage will lead to failure. Thus, it is important to obtain a secure implant-to-bone interface as soon as possible after surgery. There are two approaches in use today to reduce mobility: cemented implants or press-fit implants. For cemented bone implants, bone cement is used to provide immediate chemical fusion between the bone and implant [13]. The use of bone cement has some complications including being difficult to apply and cure at the correct implant location [13]. The second approach is to use press-fit implants, which are placed in tight contact with the bone by securely wedging the implant into the bone [14]. The research applications considered in this dissertation focus on press-fit implants, since this method provides direct material-to-bone contact which, with an optimal material surface design, can promote bone formation and implant integration.

### 1.3.1 The Hierarchical Structure of Bone

The trend that biomaterials research has taken over the years from macro to nano is entirely logical when one examines the hierarchical structure of bone (or any living system, for that matter), from the macro to nano scale. **Figure 1.3-1**depicts a schematic of the hierarchical structure

of bone, illustrating the intricate nature of the smallest elements, i.e. collagen molecules and hydroxyapatite crystals in the extracellular matrix (ECM) [11]. A very important part of orthopaedic implant design is choosing or engineering the implant material to match the macro scale characteristics of bone (i.e. strength, Young's Modulus). A considerable amount of research has focused on advanced alloying techniques (particularly with titanium) in order to achieve lower elastic moduli that are more on the level of the modulus of cortical bone (~15-25 GPa) [15]. This approach to advance orthopaedic implant materials is a key part of this field of research. However, **Figure 1.3-1**lays emphasis on the need to consider not only the macro scale of the structure of bone, but components in the micro and nano regime as well. Within the scope of this dissertation, we consider the cellular level and smaller to be of utmost importance when contemplating orthopaedic implant design.

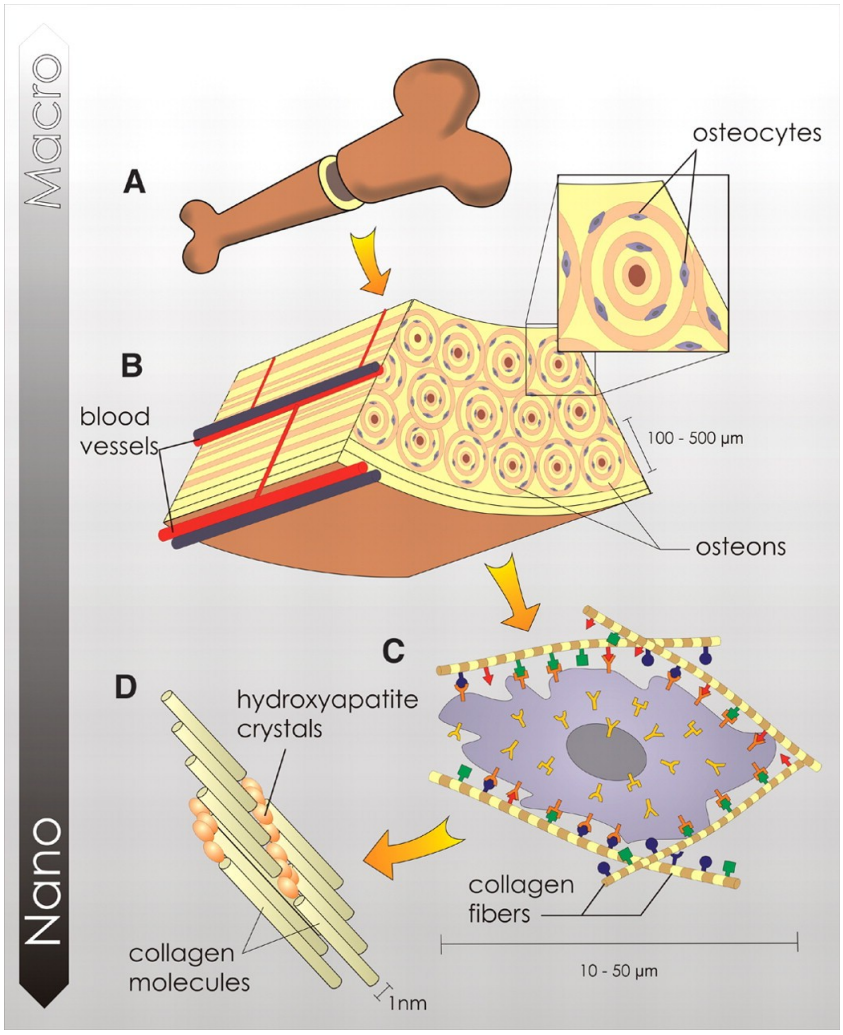


**Figure 1.3-1.** Schematic illustration of the hierarchical organization of bone, from the macro to nano scale [11]. Bone is composed of a strong calcified outer compact layer **(A)**, which consists of many cylindrical osteons **(B)**. Bone cells respond to interactions with various extrinsic factors from the micro to nano regime **(C)**, including the well-defined nanoarchitecture of the surrounding extracellular matrix **(D)**.

It is worthy to note that although the cell is the smallest living unit of the body, cells are guided and influenced by factors at the molecular level both intrinsically (inside the cell) and extrinsically (outside the cell) [11]. Cells are readily influenced by external factors due to the direct connection between the cytoskeleton components (actin microfilaments)

and the extracellular matrix through integrins, which are embedded in the cell membrane, as illustrated in **Figure 1.3-2**. The normal cell environment is composed of a complex network of biomolecules and collagen fibers on the nanoscale. The cell's ability to properly function in terms of proliferation, differentiation, and cell-specific operations intimately depends on the cells capability to create and maintain an intact ECM [16]. Cells are predisposed to interact with and gain guidance from nanostructured features outside of the cellular environment [17]. Consequently, one of the most important parts of biomaterials design is the features of the surface on the nanoscale. By examining the intricate relationship between the cell and a nano-surface will provide information crucial to the future of materials science for tissue regeneration and beyond.

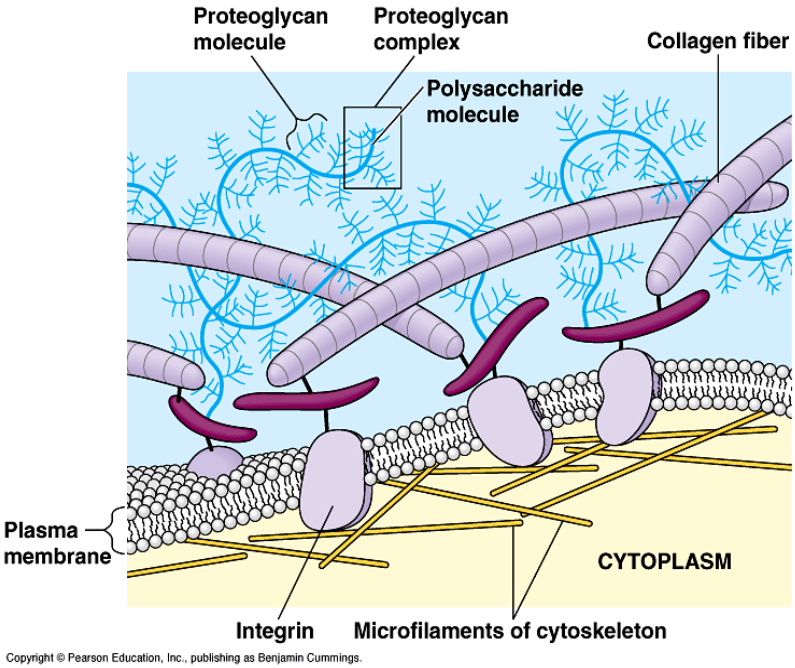


**Figure 1.3-2.** Illustration of the cross-section of the cell membrane, revealing the intricate nature of the extracellular matrix and intracellular components (integrins and microfilaments of cytoskeleton) connecting to the ECM [18].

### 1.3.2 The Importance of the Surface

The fact that cells can be regulated by extrinsic signals to the cell from the surrounding extracellular matrix (ECM) has triggered an entirely new level of biomaterials design, in which researchers attempt to promote or mimic the natural extracellular matrix of a cell in order to guide cell response. The implant surface has been shown to play an important role in the rate and extent of implant osseointegration [19-23]. Events leading to either implant acceptance or rejection occur at the tissue-biomaterial interface. The surface plays a vital role in the biological response to a material for four reasons: (1) the surface is uniquely reactive, (2) the surface is usually very different in morphology and chemistry than the bulk,

(3) the surface is the only part of the implant that is in direct contact with the biological environment, and (4) surfaces readily contaminate (especially in biological fluids). Material surface properties such as chemistry [24], roughness [25-26], wettability [27], surface energy [28-29], surface charge [30], surface oxidation [31], and surface features and shape [32] are among some of the most critical factors which affect cell and tissue-materials interactions [33]. The reason that cells are so sensitive to such minute materials characteristics has to do with the complex mechanism with which a cell adheres to and senses a surface.

The initial event at the surface of a material *in vitro* or *in vivo* is the adsorption of proteins from surrounding culture media or biological fluids, which occurs in less than 1 second. The arrangement and adhesion of proteins to a surface is highly dependent on the surface properties. Cells then come into contact with proteins, not the bare surface. Therefore, a clear understanding of the adsorption of proteins onto a surface is vital for understanding cell behavior. The basic sequence of events at the surface can be summarized by **Figure 1.3-3**:

a) Contact of the cell with a layer of adsorbed proteins.
b) Cell surface receptors (integrins) form bonds with protein functional groups (ligands).

c) Cytoskeletal reorganization as the cell spreads and adheres to the substrate.

This series of events makes it evident that the body interprets cues from a material through the organization and quantity of proteins on the surface. It can thus be concluded that for advancing biomaterials design, it is imperative that the surface be considered and designed with protein adhesion and cellular response in mind.

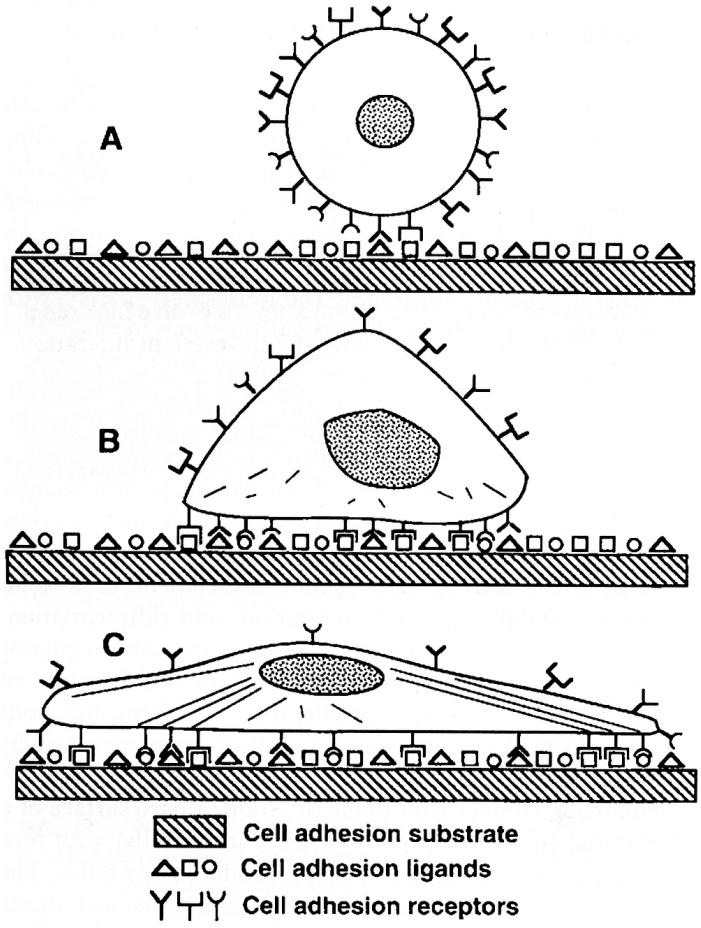


**Figure 1.3-3.** The sequence of events at the surface [34]. **(a)** The cell comes into contact with protein layer. **(b)** Bonds form between the cell (integrins) and the proteins (ligands). **(c)** The cell cytoskeleton reorganizes as the cell stretches and adheres.

Clearly, the surface of a medical device has major implications on how the body responds to the implant. Advances in technology have provided a variety of methods to modify or alter surfaces by chemical, electrochemical, mechanical, or thermal means in order to enhance, facilitate or promote a more bioactive or favorable biological response.

### 1.3.3 Common Surface Modification Techniques

Various techniques have been investigated for modifying implant surfaces in order to improve tissue response. The techniques can be categorized into two subgroups: (1) additive processes or (2) subtractive processes [34]. Additive surface modification techniques include the application of a coating onto the implant surface, via methods such as sputtering, plasma spraying, ion deposition, hydroxyapatite coating, or attaching bone binding biomolecules to the surface. Subtractive processes involve the removing of surface material in order to modify the surface structure or surface energy. Such subtractive processes include mechanical polishing, sand-blasting (a.k.a. gritblasting), chemical etching, or electrochemical anodization. These techniques introduce modifications to the surface such as surface texture (roughness), chemical composition, and surface energy (also hydrophilicity). Often one mode of surface modification will introduce a combination of results, because certain characteristics such as roughness and surface energy are

interrelated. Thus, it is important to examine all aspects of the material surface characteristics when a surface is modified.

One of the most popular and effective surface properties for bone implant materials is the introduction of surface roughness or topography. Micron rough surfaces are known to provide for better adhesion of biomolecules, and stronger fixation of bone or connective tissue, and prevent microorganism adhesion and inflammatory response when compared to smooth surfaces [35]. A systematic review in 2009 by Wennerber, et al. indicates a common conclusion in the literature that micron rough surfaces enhance bone formation and interlocking [36].

Orthopedic devices on the market today generally utilize a micron rough surface structure with dimensions on the scale of <10 μm [9]. Common surface technologies in industry implement roughening methods such as sand-blasting, etching, machining, and micron-sized metal bead coatings. Many studies have demonstrated enhanced osteoblast functions on such micron rough materials. Moreover, increased osteoinduction has been shown on microporous surface structures, which allows strong anchoring of the bone to the implant [37].

However, as was pointed out in Section 1.1, these micron surface structures available in the current marketplace are not sufficient for the long implant lifetimes required by the increasingly younger patient

population. Therefore, other means of manipulating the osteogenic response are being investigated.

## 1.4 Advanced Nanostructured Surface Technology

The hierarchical structure of bone described in detail in Section 1.3.1 indicates the feasibility of utilizing surface features on the sub-micron scale. Since bone is composed of nanostructured components, a relatively new approach in orthopedic implant materials research places emphasis on surfaces of nanometer roughness, topography, or features less than 100 nm in at least one direction [Sato].

Nanotechnology became an especially hot topic amongst researchers and engineers in the late 90s and early 2000s, and even began to be introduced into commercial settings [Miyazaki]. Since then, countless articles, journals, and books have been published with a multitude of techniques for the formation of nanostructured material surfaces. As a result, many methods have been investigated for the purpose of applying nanostructured coatings to biomaterial surfaces. The main challenge faced by biomaterials researchers is finding the appropriate combination of material features such as composition, topography (i.e. geometry, size, structure), and properties (i.e. elasticity, toughness, stiffness). Biomaterial surface topographies that have been utilized for tissue engineering include three general categories:

1) Lithographic surfaces, which are generally fabricated in a cleanroom environment using photolithography, e-beam lithography, and related techniques, and consist of highly organized surface structures such as grooves, islands, pillars, and holes [38]. These methods are usually very costly, since they require a cleanroom environment and highly complex equipment. Although the methods may not be very applicable in industry due to high expense, they provide unmatched avenues for furthering the understanding of cellular response to precise features such as geometry and organization.
2) Porous, roughened or textured surfaces, which are usually formed via chemical (etching) or mechanical (grinding, blasting) methods introduce a uniform topography with very little precision necessary. Highly porous and rough biomaterial surfaces have shown great promise for bone in-growth and mechanical interlocking, to prevent implant mobility [39]. These techniques are attractive because they are generally inexpensive and simple to carry out in a general laboratory environment.
3) Fibrous surfaces are formed using techniques such as electrospinning, phase separation, and self-assembly [38]. The

process of electrospinning is highly versatile because it can be used to create nanofibers of varying materials including biodegradable polymers and biological polymers such as collagen. Electrospinning can also be used to produce both 2D and 3D fibrous constructs. Nanofibrous surfaces are attractive because they closely mimic features of the extracellular matrix, and thus have great promise in the field of tissue regeneration [38].

It is clear that nanostructured biomaterial surfaces are at the forefront of next-generation orthopedic implants. With such a wide range of techniques available for the formation of a variety of surface structures, there are many possibilities for nanomaterials for bone regeneration. However, with the vast nanofabrication techniques available, careful and systematic experiments are required in order to fully understand the affect of substrate morphology on cell behavior. This field of research is still in its infancy, and further research is necessary in order to bring the next-generation orthopedic implant to the market.

## 1.5 The Scope of the Dissertation

The goal of the dissertation is to provide a clearer understanding of the behavior of osteoblast cells *in vitro* in response to particular chemical modifications of nanostructured surfaces, in particular the metal oxide

nanotubular architecture. Prior investigations have indicated that the $TiO_2$ nanotube surface is capable of inducing bone formation and even directing stem cell fate [2-3]. However, these findings raise questions such as whether the same nano-architecture can be equally effective when composed of different surface chemistries. In addition, the feasibility of fabricating the nanotube structure from a thin film of titanium on the surface of an orthopedic implant composed of another material (i.e. zirconia or CoCr) as a bioactive coating has been uncertain. The work reviewed in this dissertation attempts to answer these questions by providing in-depth experimental analysis of the osteogenic behavior on nanotube surfaces of varying surface chemistries, as well as thin film $TiO_2$ nanotube layers applied to industry-supplied orthopedic implant materials. In order to achieve the purpose of this dissertation, the more specific aims are:

1. To optimize anodization techniques for the formation of $TiO_2$ and $ZrO_2$ nanotube surface structures of defined characteristics from bulk and thin film materials.

2. To characterize the nanotube surfaces in terms of nanotube dimensions, hydrophilicity, crystallinity, biocompatibility, and osteogenic induction.

3. To evaluate the *in vitro* osteogenic response to structural and chemical nano-modifications to various implant materials.

# CHAPTER 2

## 2. Titanium Oxide Nanotubes

Owing to attractive properties such as the high surface-to-volume ratios and size dependent properties, nanostructured materials have been at the center of a large body of innovative research in science and technology. In particular, nanostructured surfaces are at the focal point of tissue engineering research due to findings which have demonstrated that cells will respond to and be directed by dimensions in the nanometer regime (< 100 nm), even as small as 10 nm height [40-41]. Although there are many methods for the fabrication of precisely defined nanostructured surfaces as mentioned in Section 1.4, one of the most simple and inexpensive processes for nanostructure formation is electrochemical anodization. In addition, other common procedures for nanostructure fabrication involve a complicated series of steps which often can only be applied to a perfectly flat substrate (i.e. nanolithography). In contrast, electrochemical anodization can be applied to substrates of various 2- and 3-D geometries and shapes, as well as sizes ranging from very small to potentially unlimited proportions. This method is also attractive because it is most commonly applied to titanium, which is one of the most widely used materials in bone implant technology. Consequently, the research dissertation herein is specifically concentrated on variations to the

nanotube surface formed by electrochemical anodization in a fluorine containing electrolyte for orthopedic device applications.

The formation of titanium oxide ($TiO_2$) nanotube arrays via electrochemical anodization was first reported by Grimes, et al. in 2001 [42]. Since their discovery, researchers have achieved better control of nanotube formation through such methods as varying electrolyte concentration and pH, inorganic and aqueous solvents, etc. Extensive control is now possible of nanotube morphology and dimensions including diameter, length, length-to-diameter ratio, wall-thickness, tube shape (conical versus cylindrical), transparency, and even doping [43]. Such ability to precisely control nanotube formation via electrochemical anodization has great promise for their utilization in many applications ranging from solar energy, water splitting, and the biomedical materials industry [44].

In addition, researchers have been able to apply the same technique of electrochemical anodization to other metals, including zirconium (Zr) [45], niobium (Nb) [46-49], tungsten (W) [50-51], hafnium (Hf) [52], and tantalum (Ta) [53-56] thus forming nanotube arrays of these metal oxides. The work discussed in this dissertation will focus solely on titanium oxide ($TiO_2$) and zirconium oxide ($ZrO_2$) nanotubes, and the

effects of other variations in nanotube surface chemistry on osteoblast and mesenchymal stem cell growth and function.

## 2.1 Mechanistic Model of Nanotube Formation

Electrochemical anodization of titanium (Ti) or other metal foils involves a two-electrode electrochemical cell with a platinum (Pt) foil cathode and metal foil (titanium or other metal of choice) anode which are held at a constant potential (see **Figure 2.1-1(a)**). The traditional method of anodization utilizes a hydrofluoric acid (HF) based electrolyte [42, 57-58]; however these nanotube layers are not able to exceed 500-600 nm thickness. By using alternative fluorine sources in the electrolyte solution, such as ammonium fluoride ($NH_4F$) or sodium fluoride (NaF) instead of HF, increased nanotube lengths (greater than 2 μm) are possible [59-61]. Additionally, the original electrolyte solutions were aqueous-based; since then, it has been found that increased control of nanotube morphology, smoother walls, and lengths greater than 7 μm can be achieved using inorganic solvents such as ethylene glycol and glycerol [62-63]. For aqueous-based electrolytes, it was found that nanotubes of greater mechanical robustness can be achieved using the addition of acetic acid to the HF electrolyte in a 1:7 ratio [43]. A trend in nanotube growth that is consistent, no matter the electrolyte

concentration, is an increase in nanotube diameter as a result of increased applied voltage.

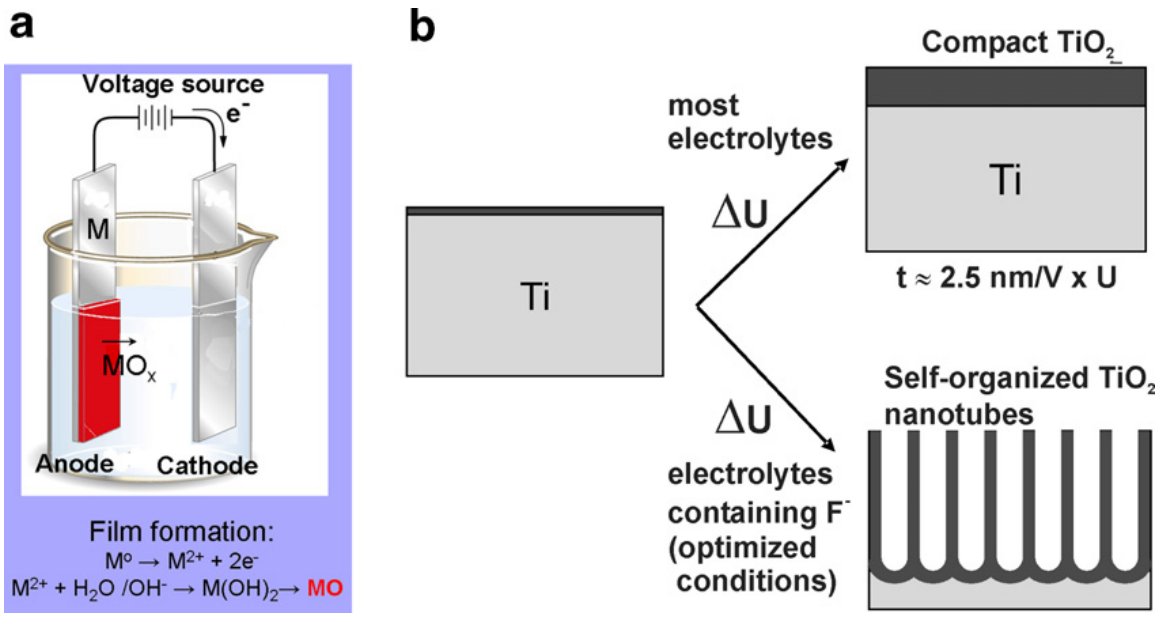


**Figure 2.1-1. (a)** Schematic drawing of the electrochemical anodization setup. **(b)** Depending on fabrication variables (i.e. voltage, electrolyte concentration, temperature, and pH), the solid oxide layer can be either compact, or nanotubular (nanoporous) [44].

There are several comprehensive review articles which present a mechanistic model of nanotube formation by electrochemical anodization, in particular the reviews by Mor, et al. and Macak, et al. [43-44]. The formation of nanotube arrays in a fluoride containing electrolyte can be summarized as the result of three simultaneously occurring processes:

**Process 1:** Field assisted oxidation of the metal to form an oxide,

**Process 2:** Field assisted dissolution of the metal ions in the electrolyte, and

**Process 3:** Chemical dissolution of the metal and metal oxide due to etching by fluoride ions.

During the first process, oxide formation occurs due to the interaction of $O^{2-}$ or $OH^-$ ions with the metallic surface. Anodic oxidation of a metal (Me) to form compact oxide or nanotubes can be most simply summarized as the competition between the anodic oxide layer formation according to reaction (1):

$$Me + 2H_2O \rightarrow MeO_2 + 4e^- + 4H^+ \quad (1)$$

and chemical dissolution of the oxide layer as soluble fluoride complexes such as shown in reaction (2):

$$MeO_2 + 6F^- \rightarrow [MeF_6]^{2-} \quad (2)$$

Chemical dissolution can also occur through direct complexation of metal cations at the oxide/electrolyte interface according to reaction (3):

$$Me^{4+} + 6F^- \rightarrow [MeF_6]^{2-} \quad (3)$$

Reaction (1) describes the oxide growth due to anodization in a fluoride-free electrolyte (e.g. $H_2SO_4$). This results in the formation of a thin oxide layer that covers the entire metal surface, as depicted in **Figure 2.1-2(a)**. As the oxide layer grows, the field within the oxide is reduced; thus the process is self-limiting, and results in a finite oxide thickness [44].

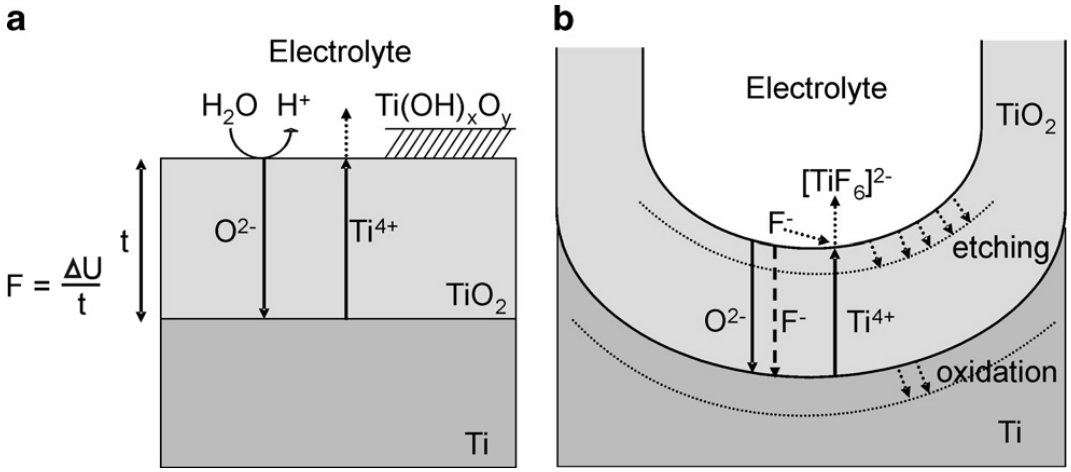


**Figure 2.1-2.** Schematic illustration of the Ti anodization **(a)** in the absence of fluorides, resulting in flat layers, and **(b)** in the presence of fluorides, resulting in tube growth [44].

In the presence of a fluoride-containing electrolyte, the process becomes a competition between the reactions (1)-(3), as depicted in **Figure 2.1-2 (b)**. Once the initial oxide layer is formed, the $O^{2-}$ and $OH^-$ anions migrate towards the metal/oxide interface where they react with the metal. At this point, Process 2 dominates over Process 3, meaning that the field-assisted dissolution of the metal occurs more rapidly than the chemical dissolution of the metal and metal oxide. As a result, small pits begin to form due to the localized dissolution of the oxide. These pits grow larger into pores due to the etching of the oxide layer at oxide/electrolyte interface of the pore bottom (barrier layer) and oxidation at the oxide/metal interface as shown schematically in **Figure 2.1-2(b)** [43]. The $Ti^{4+}$ cations migrate from the metal to the oxide/electrolyte interface and are then dissolved into the electrolyte.

A typical current–time curve of electrochemical anodization resulting in flat layers (black curve) and nanotube formation (red curve) is illustrated in **Figure 2.1-3(a)**. Based on the current transient, the tube formation process can be segmented into three phases which correspond to different surface morphologies on the surface (**Figure 2.1-3(b)**) [44]. First, a barrier oxide layer is formed, which results in an exponential decay of the current (phase I). The surface then becomes locally activated and pores begin to grow randomly, causing the current to increases again due to an increase in active area in the porous structure (phase II). As the pores grow, they start interfering with each other, competing for available current [44]. Under optimized conditions, the pores eventually begin to equally share the available current, resulting in self-ordering under steady state conditions (phase III) [44]. This sequence of events at the titanium surface can be observed by SEM [64].

As depicted in **Figure 2.1-3(c)**, the steady state tube growth occurs when the rate of oxide dissolution at the inner pore bottom ($v_1$) eventually equilibrates with the rate of oxide growth at the metal/oxide interface ($v_2$, outer pore bottom) [44]. From then on the oxide layer thickness remains the same, but moves deeper into the metal substrate.

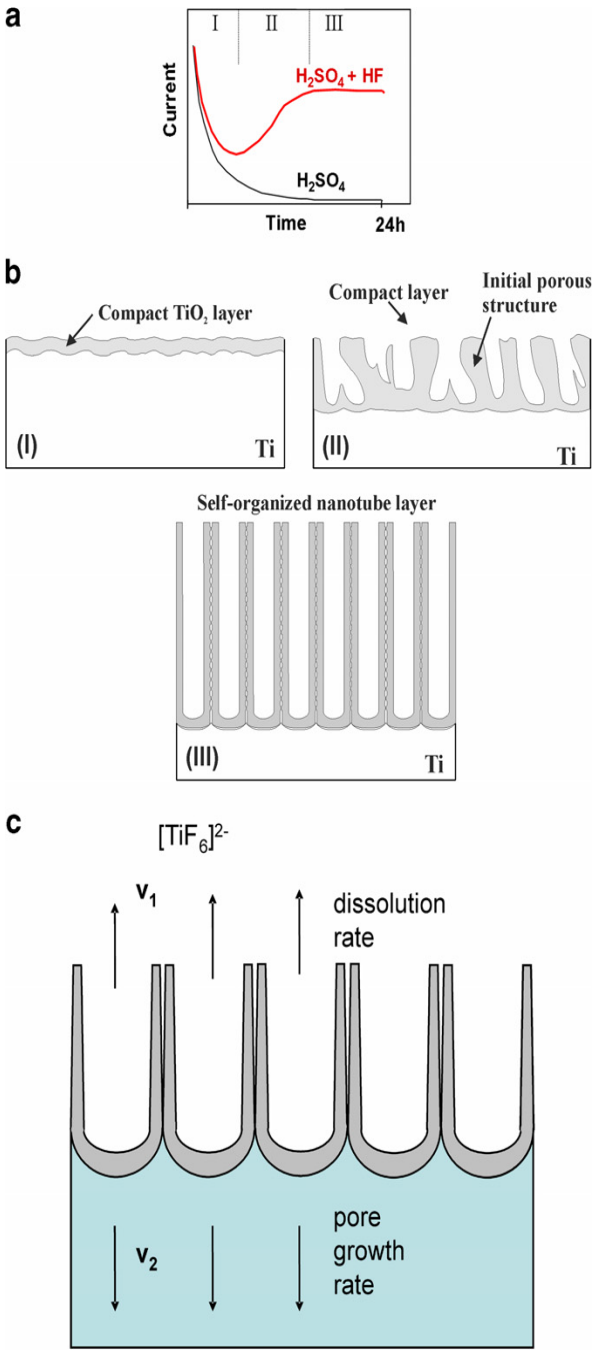


**Figure 2.1-3.** Schematic depiction of **(a)** characteristic current transients for Ti anodization with and without fluorides in the electrolyte; **(b)** corresponding evolution of the $TiO_2$ morphology; **(c)** steady state growth situation characterized by equal rates of $TiO_2$ dissolution ($v_1$) and formation ($v_2$) [44].

One phenomenon of nanotube formation that is not clearly understood is the reason for separation into tubes, as opposed to a nanoporous structure (as in the case of anodized aluminum oxide, or AAO). In order to more clearly describe the formation of the nanotube array, **Figure 2.1-4**depicts the ideal sequence of events as they occur at the surface, as described by Mor, et al. [43]. The first step is the formation of a thin oxide layer on the surface of the metal (**Figure 2.1-4(a)**). Secondly, small pits begin to form in the oxide layer due to localized dissolution of the oxide (**Figure 2.1-4(b)**). The pores continue to grow as a result of the thin barrier layer at the pore bottom which increases electric field intensity (**Figure 2.1-4(c)**). At this stage, the pore surface is not affected by field-assisted dissolution, but at the curved pore bottom, resulting in pore widening, and a scallop-shaped pore. Mor, et al. attributes the high energy of the Ti-O bond (323 kJ/mol) to the fact that $TiO_2$ nanotubes can only form with relatively thin walls due to low ion mobility and high chemical solubility, which results in un-anodized metallic portions in between pores at the beginning stages of anodization. However, as the pores become deeper, the field assisted dissolution becomes concentrated on the protruding metallic portions resulting in enhanced field-assisted oxide growth and dissolution, and thus inter-pore voids begin to form (**Figure 2.1-4(d)**). Subsequently, the pores and voids

grow in equilibrium until the electrochemical etch rate equals the chemical dissolution rate at the top surface of the nanotubes (**Figure 2.1-4(d)**). The nanotube length increases with anodization time until the chemical dissolution rate at the tube opening (top surface) and the rate of inward movement of the barrier layer at the bottom of the tube become equal. Hence, when a greater voltage is applied, the rates of oxidation and field-assisted dissolution are faster than the rate of chemical dissolution, enabling greater nanotube thicknesses to be achieved before equilibrium is reached [43]. As expected, the rate of each of the key Processes 1 – 3 must be controlled by careful control of anodization conditions in order to obtain well-organized nanotubes.

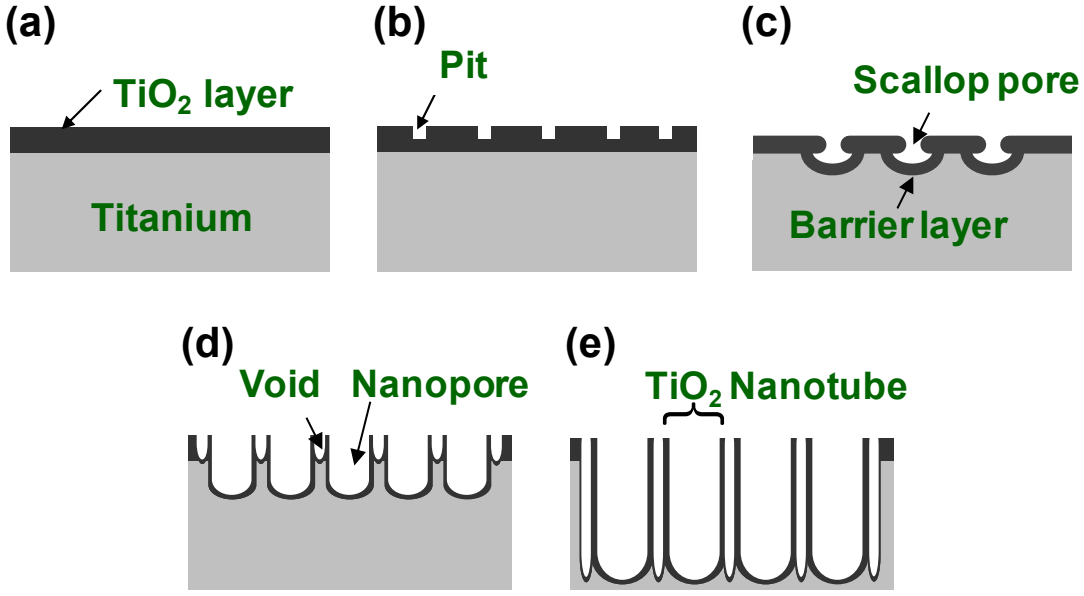


**Figure 2.1-4.** Schematic illustrating the ideal sequence of events at the titanium surface during electrochemical anodization. **(a)** Oxide layer formation; **(b)** pit formation on the oxide layer, **(c)** growth of the pit into scallop shaped pores, **(d)** metallic part between the pores becomes a void due to oxidation and field-assisted dissolution, and **(e)** a fully developed nanotube array. Schematic revised from [43].

It must be noted, however, that **Figure 2.1-4** describes *ideal* nanotube formation under perfect anodization conditions. During the actual observed process of tube formation, the chemical dissolution of $TiO_2$ occurs over the entire tube length; thus as the nanotube length increases, the tubes become increasingly V-shaped (thin walls at the top, thick walls at the bottom) due to a higher rate of chemical etching at the tube opening than at the pore bottom [44]. The tube surface morphology can be over- or under-etched due to an un-optimized chemical etching rate. This can largely be controlled by optimizing the HF concentration or experimental temperature [65]. In extreme cases, the rate of chemical dissolution at the tube opening can be too high, resulting in tubes with broken walls and disordered bundling at the top surface. Macak, et al. refers to this phenomenon as rapid breakdown anodization (RBA) [44].

Another key point regarding the formation of nanotubes via electrochemical anodization is that although tube formation is a self-organized process, the pit formation is not well organized to begin with, as mentioned earlier. The beginning stages of pore formation are not unidirectional, but may veer in any direction. However, as the pores develop, the process becomes more organized. Thus, the top surface of nanotubes may have a disorganized surface. Several approaches have been taken to achieve a very high degree of nanotube ordering, in

particular a hexagonal close-packed structure. Four factors have been found to strongly influence the degree of ordering: (i) the electrolyte solvent (the use of highly viscous organic electrolyte solutions, such as ethylene glycol or glycerol has been shown to significantly increase ordering over aqueous solutions) [44], (ii) the anodization voltage (the highest possible voltage just below dielectric breakdown) [44], (iii) the purity of the material (high purity Ti results in more ordered tubes) [44], and (iv) repeated anodization (the tube bottom imprints serve as "pre-ordering" guides for subsequent anodic tube initiation and growth) [66].

The ability to produce highly organized vertical nanotube arrays is a highly complex process in which careful optimization of each experimental parameter must be considered. Further interesting variations to the nanotube geometry, morphology, and size, as well as phenomena such as two size self-organization of the nanotube diameter [44], have been demonstrated which are not discussed herein. Due to extensive research, the formation of $TiO_2$ nanotubes has become a relatively well-understood process enabling highly tunable nanotube morphology and features using simple and inexpensive laboratory materials. The application of these unique nanostructures are thus of great interest for furthering the advancement of nanotechnology.

## 2.2 Osteoblast and Mesenchymal Stem Cell Growth and Functionality on $TiO_2$ Nanotubes

### 2.2.1 Experimental Methods

#### *$TiO_2$ Nanotube Fabrication*

$TiO_2$ nanotube surfaces were created using a two-electrode-setup anodization process, as described previously [1, 67]. Briefly, a 0.25 mm thick cp-Ti sheet (Alfa-Aesar, 99.5% metals basis, USA) was used for this process. The nanotubes were prepared in a 1:7 volumetric ratio of acetic acid (99.99% purity, Sigma–Aldrich) to 0.5% w/v hydrofluoric acid in water (48% w/v, EM Science, USA) at 5, 10, 15 and 20 V for 30 min. A platinum electrode (99.9% pure, Alfa-Aesar, USA) served as the cathode. The samples were then washed with deionized water, dried at 80 °C and heat treated at 500 °C for 2 h in order to crystallize the as-fabricated amorphous structured $TiO_2$ nanotubes into an anatase structure. The anatase phase was confirmed by Raman spectrometry using an argon laser (Horiba model iHR320 imaging spectrometer, at 514.5 nm wavelength).

The samples (1.27 X 1.27 cm2) used for all experiments were sterilized by autoclaving prior to use. A flat Ti sheet cut into identically sized pieces was used as a control after being chemically cleaned by acetone and isopropanol for 10 min in an ultrasonic cleaner, dried and autoclaved.

***Atomic Force Microscopy***

An atomic force microscope (AFM) was used to characterize the roughness of the samples. The AFM apparatus was a Veeco scanning probe multi-mode microscope with a nanoscope IV controller. The average roughness (Ra) was measured for all experimental samples (Ti and 30–100 nm $TiO_2$ nanotube surfaces) in tapping mode using Micromasch tapping cantilever tips (NSC15/NoAl) over a 1.0 $\mu m^2$ scan area.

***Contact Angle Measurement***

The measurement of contact angle for the 30–100 nm $TiO_2$ nanotube surfaces was carried out by a video contact angle measurement system (Model No. VSA 2500 XE, AST Products, Inc.).

***XRD Measurement***

Phase transition and crystallization of annealed $TiO_2$ nanotube samples were confirmed by X-ray diffraction analysis data (Rigagu Gelgerflex model D/Max-IIB) using a maximum potential of 50 kV and current of 32 mA.

***Osteoblast Cell Culture***

For these studies, MC3T3-E1 mouse osteoblast (CRL-2593, subclone 4, ATCC, USA) were used. Each 1 ml of cells was mixed with 10 ml of alpha minimum essential medium (α-MEM; Invitrogen, USA) in the presence of 10

vol. % fetal bovine serum (FBS; Invitrogen, USA) and 1 vol. % penicillin–streptomycin (PS; Invitrogen, USA). The cell suspension was plated in a cell culture dish and incubated at 37 °C in a 5 vol % $CO_2$ environment. When the concentration of the MC3T3-E1 osteoblastic cells reached ~3 X $10^5$ cells $ml^{-1}$, they were seeded onto the experimental substrate of interest ($TiO_2$ or Ti), which was placed on a 12-well polystyrene plate and stored in a $CO_2$ incubator for 24, 48 and 72 h to observe the cell morphology and count the number of viable cells attached as a function of incubation time. The concentration of the cells seeded onto the specimen substrate was 1 X $10^4$ cells per well.

***Mesenchymal Stem Cell Culture***

Human mesenchymal stem cells (hMSCs) were obtained from Lonza Corporation. The cell growth media were composed of a-MEM (Invitrogen), 10% Fetal Calf Serum (FCS) (Invitrogen), 100 units/mL penicillin, and 100 µg/mL streptomycin (Invitrogen). For preparing positive control in this research, osteogenic inducing media were also prepared by adding 10nMdexamethasone (Sigma), 150 µg/mL L-ascorbic acid (Sigma), and 10 mM β-glycerophosphate (Calbiochem) to cell growth media. The cells were cultured in a 5% $CO_2$ incubator at 37 °C. All experiments of hMSCs were conducted with cultures at passage 4.

***Cell Counting and Viability Test***

In order to count adhered osteoblasts on experimental specimens, a Coulter particle counter (Model Z-1, Beckman Coulter Inc., USA) was utilized. Fluorescein diacetate (FDA; Sigma, USA) staining was conducted to measure cell elongation. At 2 and 24 h after plating, the cells on the substrates were washed with phosphate-buffered saline (1X PBS) solution (Invitrogen, USA) and incubated for approximately 30 s with FDA stock (5 mg dissolved in 1 ml of acetone) dissolved in PBS (10 µl/10 ml), and washed once more. The samples were then inverted onto coverslips, mounted, visualized and photographed using a fluorescence microscope with a green filter (DM IRB, Leica
Co., USA).

***SEM for Substrate and Cell Morphological Examination***

After 2 and 24 h of culture, the cells on the substrates were washed with PBS and fixed with 2.5% w/v glutaraldehyde (Sigma, USA) in PBS for 1 h. After fixation, they were washed three times with PBS for 15 min each wash. The cells were then dehydrated in a graded series of ethanol (50, 70, 90 and 100 vol %) for 30 min each and left in 100% ethanol to be dried by a critical point dryer (EMS 850, Electron Microscopy Science Co., USA). Next, the dried samples were sputter-coated with gold for examination by scanning electron microscopy (SEM). The morphology of the $TiO_2$

nanotubes as well as that of the adhered cells were observed using an XL30 scanning electron microscope (FEI Co., USA).

***Data Analysis for Cell and Nuclear Elongation/Area***

To quantify the differences in cell morphology observed in the SEM results for 2 and 24 h, the major and minor axes were measured by use of the scale bar and the major/minor ratio was used as the elongation ratio. For nuclear morphology, boundaries of the DAPI-stained nuclei were outlined by using Image J software, a public domain image processing and analysis program developed by the NIH. The nucleus major and minor axes and spreading area were measured by Image J. For the purposes of this study, the major and minor axes results were displayed as a ratio for elongation.

***Real-Time PCR***

After 2 weeks of culture, total RNA of the cells on the Ti and $TiO_2$ nanotube substrates were extracted with TRIzol (Sigma), and reverse transcribed into cDNA by qScript cDNA Synthesis Kit (Quanta BioSciences). Real-time PCR was performed by Taqman Gene Expression Assays (Applied Biosystems), and the information of Taqman PCR primer is as follows: GAPDH (Hs99999905_m1; Amplicon length, 122), ALP (Hs01029141_g1; Amplicon length, 71), OCN (Hs00609452_g1; Amplicon length, 74) and OPN (Hs00960942_m1; Amplicon length, 63). Real-time

PCR was carried out by using Taqman Fast Universal PCR Master Mix and 7900 HT Fast Real-Time PCR System (Applied Biosystems). cDNA samples (1 µL for total volume of 20 µL) were analyzed for gene of interest and for house-keeping gene GAPDH. The comparison test of cycle-threshold point was used to quantify the gene expression level of each sample. In this study, all levels of expression were normalized by the level of expression of positive control (hMSCs cultured with osteogenic inducing media).

***Alkaline Phosphatase Activity Test***

After the selected incubation periods, the samples were washed by PBS and transferred to a new 12-well polystyrene culture plate. A 500 µl quantity of 0.1% w/v Triton X-100 (Sigma, USA) was added to each well to study the lysis of cells. After incubating in the 5% $CO_2$ incubator for 2 h, the solutions were transferred (2 ml) to a microcentrifuge tube and frozen at -80 °C for 2 h. After running three freeze–thaw cycles to homogenize the solutions, aliquots of the solutions were used to measure the total protein content (Bradford protein assay kit, Bio-Rad Laboratories, USA) and 350 µl of the solutions was used for the alkaline phosphatase (ALP) activity test. An equal volume (350 µl) of ALP substrate solution (ELPN-500, Bio-Assay Systems, USA) was added to each solution and the solutions were mixed at room temperature for 30 min. After this time, 350 µl of 1 M sodium hydroxide (NaOH; Fisher Scientific Co., USA) was added to stop the

reaction. The absorbance of each solution was measured at a wavelength of 405 nm by UV–vis spectrophotometer.

***Statistical Analysis and Error Bars on Graphs***

Sigma Plot software (2001), which specializes in scientific data analysis and presentation, was utilized to demonstrate the statistical significance of the assays. The graphs show the average ± standard error bars associated, with the sample size (or N values) shown in a box in the upper portion of each graph.

### 2.2.2 Results and Discussion

$TiO_2$ nanotubes were first investigated as a biomaterial for enhanced bone growth in 2006 by the Jin Lab. It was demonstrated that the nanotube surface significantly accelerated osteoblast adhesion and proliferation and enhanced bone mineral formation when compared to non-modified titanium surfaces [1]. These initial experiments were performed on $TiO_2$ nanotubes of ~100 nm diameter and ~300 nm height, with a wall thickness of ~10 nm. As was mentioned in Section 2.1, precise control of the nanotube diameter is possible by varying the applied voltage during anodization. In order to further understand the influence of the nanotube architecture on bone cell behavior, a series of studies were performed in which the lateral spacing of the nanotube system was varied by altering the nanotube diameter from 30, 50, 70, and 100 nm, as

depicted in **Figure 2.2-1**. The average surface roughness (Ra) and contact angle measurements for the corresponding flat Ti and various nanotube surfaces are reported in **Figure 2.2-1(b)**.

(a)

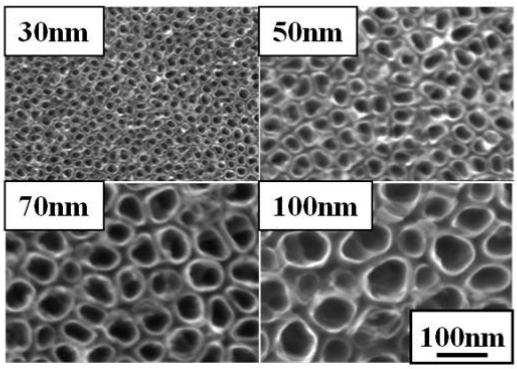


(b)

| Sample | Roughness Ra (nm) | Contact Angle (°) |
|---|---|---|
| Ti | 9.7 | 54 |
| 30nm | 13.0 | 11 |
| 50nm | 12.7 | 9 |
| 70nm | 13.5 | 7 |
| 100nm | 13.2 | 4 |

**Figure 2.2-1.** Physical characterization of different size nanotube surfaces. **(a)** SEM micrographs of self-aligned $TiO_2$ nanotubes with different diameters. The images show highly ordered nanotubes with four different pore sizes between 30-100nm. **(b)** Table with average roughness (Ra) and surface contact angle measurements for Ti and 30-100nm $TiO_2$ nanotube surfaces.

As described in Section 2.2.1, the as-formed $TiO_2$ nanotubes were heat treated at 500° C for 2 h in order to reduce residual fluorides, and to crystallize the as-fabricated amorphous $TiO_2$ nanotubes into anatase. X-ray diffraction (XRD) measurements were performed to confirm the crystal structure after annealing. The XRD pattern (**Figure 2.2-2)** indicates that both Ti (blue) and anatase $TiO_2$ (green) and are present. The intense peaks indicating a large amount of Ti are reasonable considering that the nanotubes are a thin film on an underlying bulk Ti substrate. The peak intensity ratios of the Ti pattern differ largely from the intensity ratios of the experimental pattern. This is likely due to insufficient randomness present

in the bulk Ti underlying substrate, since the scan area of the diffractometer used is relatively small. The anatase form of $TiO_2$ has a tetragonal crystal structure with $a = b = 3.784$ Å, and $c = 9.515$ Å [68]. It has been shown previously that osteoblast cells are able to distinguish between rutile and anatase forms of $TiO_2$, and that they prefer the anatase phase of nanostructured surfaces [1, 69]. Thus all $TiO_2$ nanotubes utilized in this study were of anatase phase.

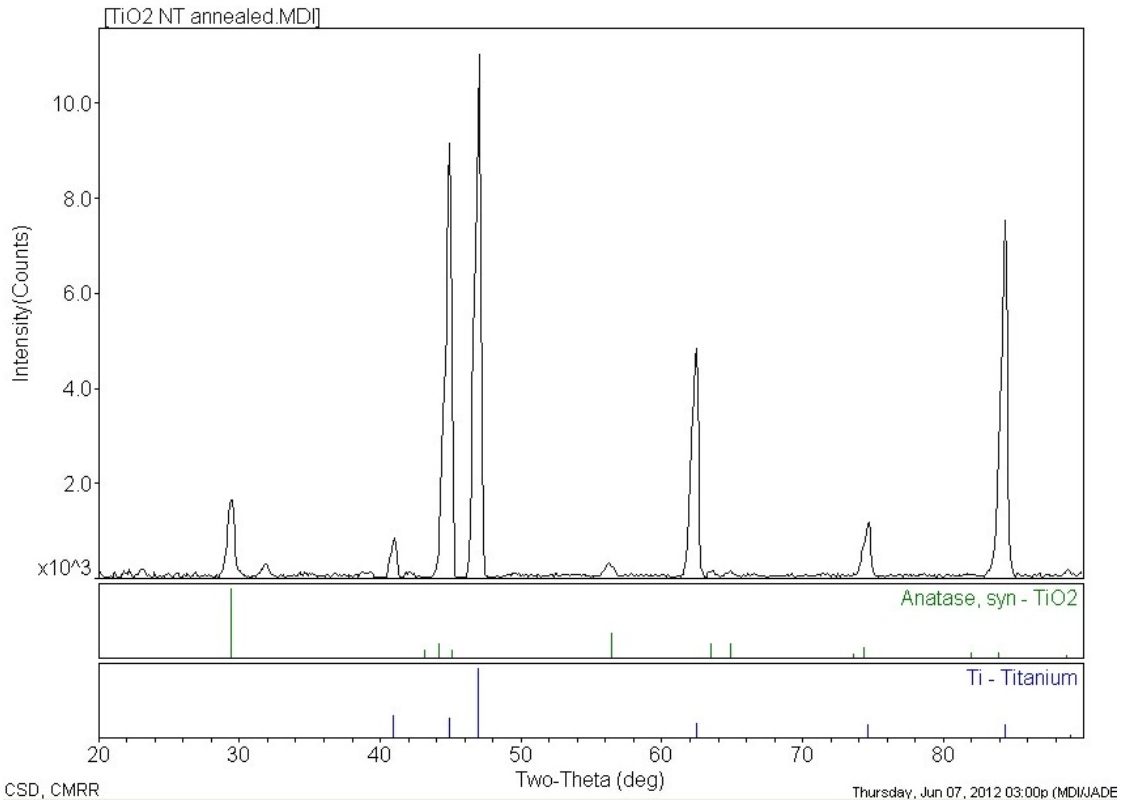


**Figure 2.2-2.** X-ray diffraction pattern of $TiO_2$ nanotubes after annealing at 500 °C for 2 h reveals the presence of anatase (green peaks) and titanium (blue peaks) crystal structures. The intensity of the titanium peaks is very high due to the underlying bulk Ti substrate.

### 2.2.3 Effect of Nanotube Size on Osteogenic Behavior

Most bone implant materials are placed in direct contact with both adult bone and bone marrow tissue, and thus are exposed to two main cell types: osteoblasts (bone cells) and mesenchymal stem cells (bone marrow cells). In order to develop an understanding of the role of the $TiO_2$ nanotube surface *in vitro*, the behavior of osteoblast cells and mesenchymal stem cells (MSCs) was studied on a series of nanotube sizes shown in **Figure 2.2-1**. Experimental conditions and sample preparation techniques were held constant in both studies, while only the cell type was varied. The cell morphology of both osteoblast and MSCs were analyzed using scanning electron microscopy (SEM). In both studies, an increase in cell elongation was observed as a function of nanotube diameter, as shown in **Figure 2.2-3**. On the flat Ti substrate, both cell types are flat, spread out, and round-shaped; they are somewhat flat and rounded on 30 nm nanotubes, and they become progressively elongated as the nanotube diameter is increased to 50 nm diameter and beyond. It is evident that the nanotubes with diameters of 70 and 100 nm induce extraordinary cell elongation (see red arrows and brackets) after 24 h of culture. In addition, the elongated leading edges of lamellipodia (yellow arrows) of both cell types indicate that the cell morphologies are more mobile on the 70 and 100 nm nanotubular surfaces.

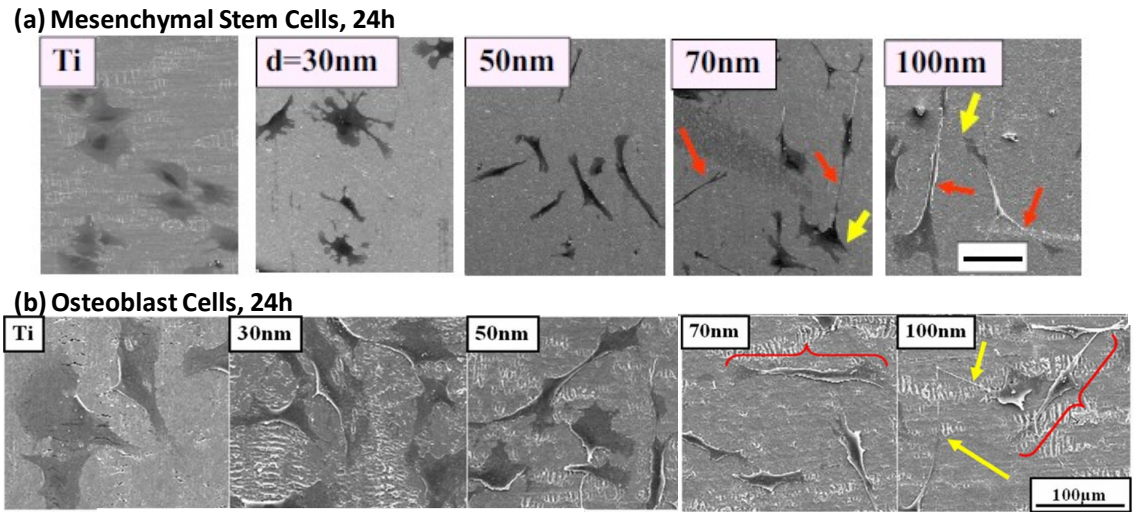


**Figure 2.2-3.** SEM micrographs of **(a)** human mesenchymal stem cells (hMSCs) and **(b)** mouse osteoblast cells (MC3T3-E1) on flat Ti and 30, 50, 70, and 100 nm diameter $TiO_2$ nanotube surfaces after 24 h of culture (scale bar, 100 µm). Red arrows **(a)** and brackets **(b)** emphasize extraordinary cell elongation; yellow arrows indicate elongated leading edges of lamellipodia.

The number of cells that adhered to each surface was measured as a function of incubation time. The results of the MSC study are shown in **Figure 2.2-4(a)**, and the results of the osteoblast study are shown in **Figure 2.2-4(c)**. The highest number of adhered cells in both studies was found on the 30 nm diameter nanotube surface. In addition, the cell elongation of both experiments was quantified by calculating the ratio of cell length to width; the data of the MSC experiment is shown in **Figure 2.2-4(b)**, and the data from the osteoblast experiment is shown in **Figure 2.2-4(d)**. As was observed in the SEM images in **Figure 2.2-3**, both cell types become increasingly elongated as the nanotube pore size increases. However, comparing the cell adhesion versus the cell elongation in **Figure 2.2-4**, it is

apparent that these phenomena follow opposite trends as a function of nanotube diameter.

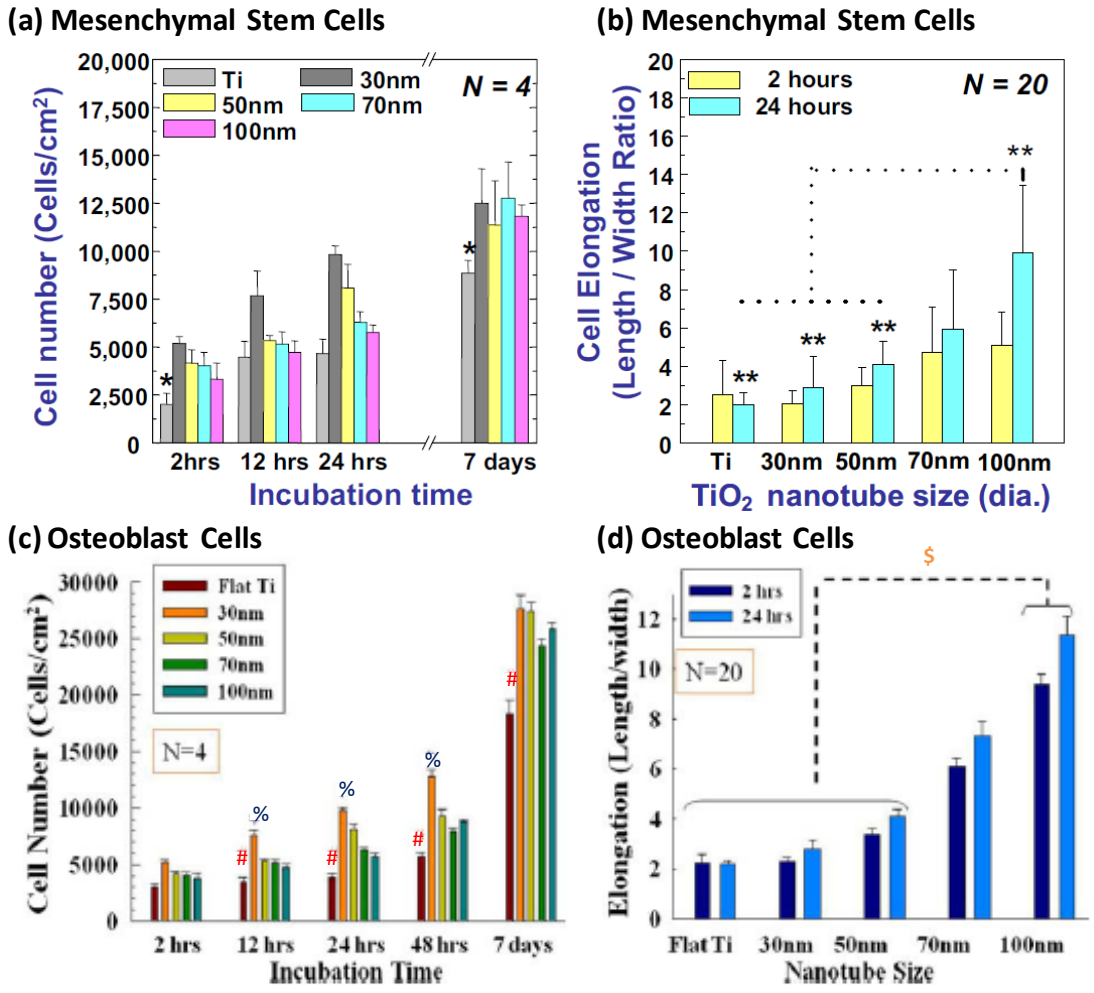


**Figure 2.2-4.** Comparative graphs showing the influence of nanotube diameter on cell number and elongation at early incubation time points. MSC cell number versus incubation time **(a)**, and MSC elongation (length to width ratio) as a function of nanotube diameter at 2 and 24 h **(b)**. Osteoblast cell number versus incubation time on each substrate **(c)** and osteoblast cell elongation as a function of nanotube diameter at 2 and 24 h **(d)**.

The results of the osteoblast and MSC cell studies indicate that the nanotube dimensions play an important role in the initial cell response to the surface, as indicated by the cell adhesion and elongation behavior.

As was emphasized in Section 1.3, the mechanism through which a cell senses and attaches to a surface is through integrins, which in fact do not sense the surface, but proteins adhered to the surface. Thus, in order to understand the behavior of cells on the nanotube topography, it is important to investigate the manner with which proteins adsorb onto the substrates. **Figure 2.2-5** shows scanning electron microscope (SEM) images of proteins adsorbed onto the flat Ti, and 30, 50, 70, and 100 nm diameter nanotube surfaces after 2 hours of incubation in cell culture medium. While the presence of protein aggregates is infrequent on Ti, there is an abundance of aggregates on the 30 nm nanotubes. However, the proteins on the larger-diameter 70 and 100 nm nanotubes are few and spaced farther apart. It is evident from these micrographs that the nanotube diameter causes distinct differences in the number and placement of proteins on the surface.

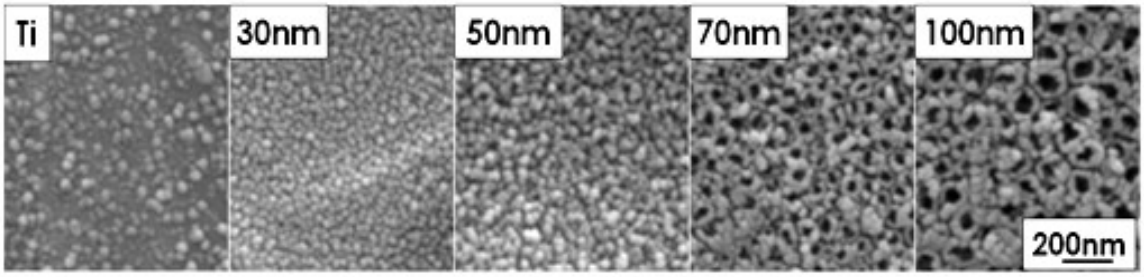


**Figure 2.2-5.** SEM micrographs showing protein adsorption on the surfaces of flat Ti and 30, 50, 70, and 100 nm diameter $TiO_2$ nanotubes after 2 h incubation in growth medium.

The phenomena of cell adhesion vs. elongation on the nanotube surfaces can be explained by the pattern of protein adsorption on each

of the substrates. The small pore size of the 30 nm surface allows for proteins to adsorb in a more tightly knit fashion, which enables the cells to adhere easily. Additionally, the 30 nm substrate does not direct the cells to move/stretch in any specific direction since proteins are everywhere. In contrast, the placement of proteins on the larger (70 and 100 nm) nanotube topographies encourages cell spreading due to the adsorption of proteins only on the nanotube wall rims, thus inducing a fixed distance between proteins and encouraging the cell to spread in order to find adhesion proteins. It is probable that the cells are required to expand their filopodia across larger distances, thus inducing the elongated cell shape. This would also affect the ability of the cell to adhere to the surface, which explains the lower number of adhered cells on the larger diameter substrates.

In addition to the observations of cell adhesion and elongation, the MSC and osteoblast cell behavior was also analyzed in terms of bone-forming functionality. In the MSC study, quantitative polymerase chain reaction (PCR) analysis was performed in order to estimate the relative transcript levels of alkaline phosphatase (ALP), osteocalcin (OCN), and osteopontin (OPN) gene expressions. The presence of these three genes is important because ALP is an enzyme produced by cells which indicates their bone-forming ability, while OCN and OPN are proteins found in bone.

The data from the PCR analysis, shown in **Figure 2.2-6(a)**, demonstrates significantly higher gene expression of all three genes on the larger diameter (70 and 100 nm) substrates when compared to the flat Ti and smaller diameter (30 and 50 nm) substrates, indicating osteogenic differentiation. Similarly, alkaline phosphatase activity of the osteoblast cells was measured on each of the experimental culture substrates. The results from the osteoblast study portray the same trend of increasing ALP activity with increasing nanotube diameter (**Figure 2.2-6(b)**). These results are evidence that the nanotube diameter causes an up-regulation in the markers of bone formation.

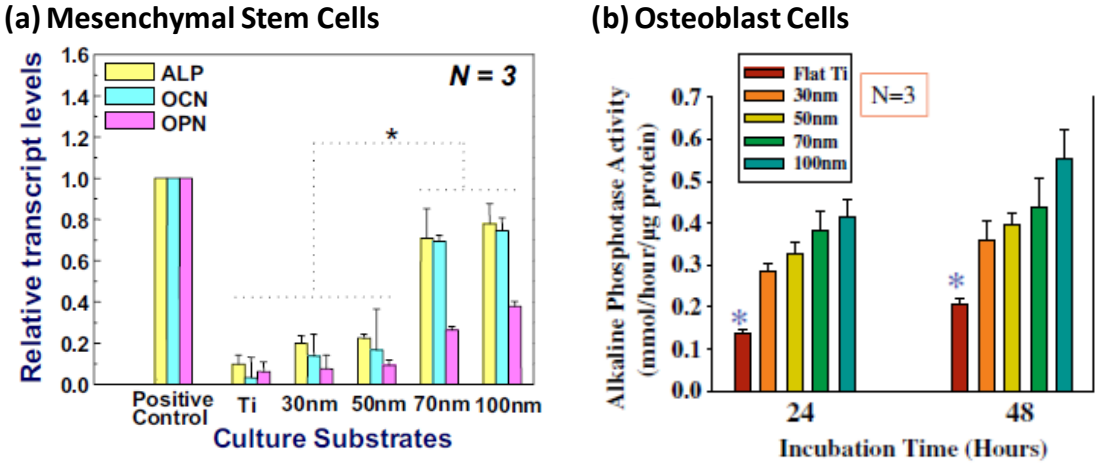


**Figure 2.2-6.** Comparative graphs showing the trend of MSC and osteoblast cell functionality with increasing nanotube diameter. **(a)** Quantitative PCR analysis for ALP, OCN, and OPN after 3 wk mesenchymal stem cell culture. Plastic cell culture plate with osteogenic inducing media was used as a positive control for osteogenic differentiation. **(b)** ALP activity after 24 and 48 h osteoblast incubation.

Since the cell elongation and cell functionality followed the same increasing trends as a function of nanotube diameter, it can be

speculated that there is a correlation between the two phenomena. Interestingly, in addition to the highly elongated cell shape on the large diameter nanotube surfaces, the cell nuclei on these surfaces were also elongated (by 20-25 %, data not shown). It is likely that the elongation of the cell nuclei is a result of the stretching of the cytoskeletal morphology of the cell. Researchers have indicated that cytoskeletal reorganization can cause nuclei distortion, which may promote differences in DNA behavior due to mechanical restraints within the nuclei [70-71]. Therefore, it is evident that the large diameter nanotube substrate induces cell elongation, and thus nuclei distortion, which may cause osteoblast and MSCs to produce markers of bone formation and osteogenic differentiation more readily than on a flat substrate.

The overall trends of the nano cue effects on osteoblast and stem cell morphology and fate can be summarized by the schematic illustration in **Figure 2.2-7**. It was observed that with increasing nanotube diameter cell adhesion and growth decreased (solid red line), in a similar manner as protein particle density (broken red line). In contrast, both osteoblast and MSCs demonstrated a higher degree of osteogenic differentiation (solid blue line) with increasing nanotube size, analogous to the trend of cell elongation (broken blue line).

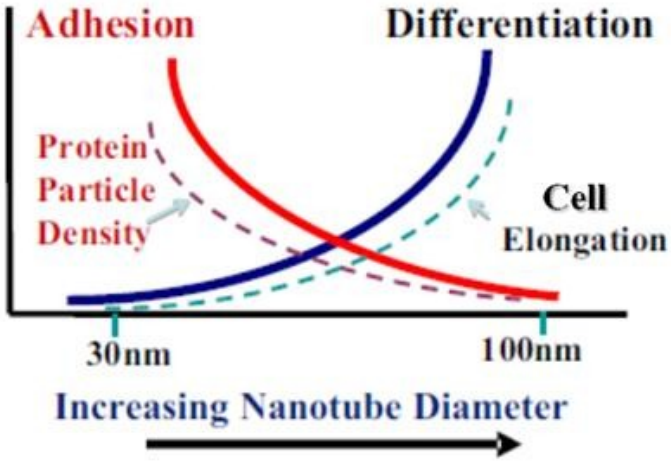


**Figure 2.2-7.** Schematic illustration of the overall trends of nano cue effects on cell fate and morphology. The change in cell adhesion and growth without differentiation (solid red line) has the same trend as protein particle density (broken red line), whereas that of differentiation (solid blue line) has the same trend as cell elongation (broken blue line).

## 2.3 Conclusions & Future Directions

The findings of these two studies give light to increased understanding of the role of nanostructure dimensions for enhanced biomaterial surface design. However, the nanotube size in these studies was restrained to a maximum diameter of 100 nm due to the limitations of $TiO_2$ anodization in an aqueous hydrofluoric acid electrolyte as was used for preparation of these surfaces. Anodization methods that enable the fabrication of larger diameter nanotube arrays have been reported, even to as large as 350 nm diameter using an electrolyte consisting of diethylene glycol with low concentrations of hydrofluoric acid (HF) [72]. However, attempts in our laboratory to utilize such large diameter

nanotube arrays for cell culture studies have determined that arrays fabricated in such inorganic electrolyte solutions tend to be extremely fragile, with a tendency to delaminate. Nevertheless, with careful control of anodization protocols, eventual progress may be made which enables the growth of mechanically strong nanotubes with large diameter pore openings. It is recommended that with such surfaces, further investigation be made into the osteoblast and MSC behavior at diameters beyond 100 nm.

The size effect of the nano dimensions of $TiO_2$ nanotube surfaces raises the question of whether the trend is unique to the $TiO_2$ nanoarchitecture fabricated via electrochemical anodization, or if osteogenic behavior would be similar on various sizes of nanotubes of different surface chemistries. In 2009 an interesting study was published by Bauer, et al. in which the size selective behavior of MSCs was analyzed on $ZrO_2$ nanotubes as well as $TiO_2$ nanotubes coated with a conformal layer of AuPd [73]. Bauer, et al. observed that the different surface chemistries did not affect the diameter dependence of cell adhesion or proliferation. However, Bauer, et al.'s study only included brief time points, and did not assess the osteogenic behavior of the cells on the nanotubes of different surface chemistries. We believe that in order to provide a more complete understanding of the osteogenic affects of the nanotube substrate *in vitro*

and *in vivo*, it is necessary to investigate the cell behavior on surface chemistries aside from $TiO_2$ at advanced time points. The focus of the following sections of this dissertation is to investigate the bone-forming ability of osteoblast and mesenchymal stem cells on the nanotube architecture possessing additional surface chemistries, including zirconium oxide ($ZrO_2$), carbon, tantalum, and tantalum oxide ($Ta_2O_5$). The Jin lab has demonstrated that various surface chemistries on the same nanotube architecture do affect multiple cell types differently [74], as will be described in detail in the following sections.

*Chapter 2 is a reprint in part of the material as it has been submitted to The Role of Biomaterials for Regenerative Medicine (submitted in response to invitation, June 2012) written by Christine J. Frandsen, Karla S. Brammer, and Sungho Jin. The dissertation author is a collaborating investigator and first author of the publication.*

# CHAPTER 3

## 3. Zirconium Oxide Nanotubes

To date, a large part of the interest has remained on titanium oxide ($TiO_2$) nanotubes because it is well known that titanium (Ti) is a biocompatible orthopedic material which provides an excellent osseointegrative surface. However, little notice has been given to zirconium oxide ($ZrO_2$) nanotubes, which are formed via the similar self-assembled mechanism as $TiO_2$ nanotubes, through an electrochemical anodization process [75]. Zirconium (Zr) is similar to titanium in that it possesses a thin passivation oxide layer which makes it highly resistant to corrosion in bodily fluids [76]. In fact, while the corrosion resistance and biocompatibility of certain Zr alloys are as good as those of Ti alloys, the mechanical properties have been found to be superior to those of the commonly used Ti-6Al-4V alloy [77]. Furthermore, a recent study by Bauer and co-workers demonstrated that mesenchymal stem cells react in the same manner to $ZrO_2$ nanotubes, AuPd-coated $TiO_2$ nanotubes, and as-formed $TiO_2$ nanotubes [73]. Their results indicate that the cell response is chiefly due to nanotopographical cues instead of a specific surface chemistry pertaining only to $TiO_2$.

## 3.1 $ZrO_2$ Nanotube Surface Prompts Increased Osteoblast Functionality and Mineralization

A more recent advancement in orthopedic biomaterials research has been made with the introduction of oxidized zirconium metal (for example, Oxinium by Smith & Nephew, Memphis, TN), a new material composed of a metallic zirconium alloy core with a very smooth oxidized zirconium ($ZrO_2$) ceramic surface [78]. This advanced hybrid biomaterial provides excellent wear resistance, e.g., as an articulating knee implant surface, without the brittleness of other ceramics [79]. However, the backside of the implant which attaches to the femur bone may not osseointegrate as well as is necessary when a cementless fixation technique is used, as indicated by a voluntary product withdrawal in August 2003 [80]. Cementless fixation can be a preferred fixation method in the knee, since the use of bone-cement has been identified as one of the contributing factors leading to debris at the articulating surface, which produces scratching of the femoral head and accelerated implant wear [78]. Thus an improved surface technology that would eliminate the need for bone-cement would be preferred. Based on prior studies on the interaction of osteoblast cells with $TiO_2$ nanotube surfaces [1-3, 67, 81-82], we hypothesize that the employment of a $ZrO_2$ nanotube surface on the bone-integrating surfaces of an oxidized zirconium implant may promote osteoblast cell growth and support ossification.

### 3.1.1 Experimental Methods

#### *$ZrO_2$ Nanotubes Fabrication*

$ZrO_2$ nanotube surfaces were created using a two-step electrochemical anodization process in order to create a more ordered final nanotube structure [75]. The zirconium foil (thickness, 0.25 mm; purity, 99.8 %, Goodfellow, UK) was first cleaned by rinsing in acetone, isopropanol, and distilled water, and finally air dried. Anodization was performed using a two-electrode-setup consisting of a platinum electrode (thickness, 0.1 mm; purity, 99.99 %; Alfa-Aesar, USA) as the cathode, and the zirconium foil as the anode. The first anodization step was performed using 0.75 mol/L ammonium fluoride (Sigma, USA) in 1 mol/L ammonium sulfate (Sigma, USA) in deionized water at 20 V for 30 min at room temperature. The first anodization layer was thoroughly removed by peeling away with adhesive tape, followed by 30 min of ultrasonic cleaning in an acetone bath. The second anodization step was performed using 0.15 mol/L ammonium fluoride (Sigma, USA) in 1 mol/L ammonium sulfate (Sigma, USA) in deionized water at 20V for 15 min at room temperature. The samples were then washed with deionized water, dried at 80° C and heat treated at 300° C for 6 h in order to reduce residual fluorides, and to crystallize the as-fabricated amorphous structured $ZrO_2$ nanotubes into a cubic $ZrO_2$ structure [45]. The samples

(1.27 × 1.27 $cm^2$) used for all cell culture experiments were sterilized by autoclaving prior to use. A flat Zr sheet cut into identically sized pieces was used for a non-textured comparison after being chemically cleaned by acetone and isopropanol for 15 min in an ultrasonic cleaner, dried, and autoclaved.

***SEM for Substrate and Cell Morphological Examination***

After 24 h of culture, the cells on the substrates were washed with PBS and fixed with a mass fraction of 2.5 % glutaraldehyde (Sigma, USA) in PBS for 1 h. After fixation, they were washed three times with PBS for 15 min each wash. The cells were then dehydrated in a graded series of ethanol (volume fractions of 50, 75, 90 and 100 %) for 30 min each and left in 100 % ethanol to be dried by a critical point dryer (EMS 850, Electron Microscopy Science Co., USA). Next, the dried samples were sputter-coated with palladium metallization for examination by scanning electron microscopy (SEM). The morphology of the $ZrO_2$ nanotubes as well as that of the adhered cells was observed using a Phillips XL30 field emission environmental scanning electron microscope (FEI Co., USA).

***Contact Angle Measurement***

The static contact angle of a water droplet on the sample surface was measured by placing 3 µl of water on the sample surface (CAM100, KSV instruments). The water droplet was spread over the sample surface

immediately after being placed on it, evident that $ZrO_2$ nanotube surface is of superhydrophilic nature as expected based on similar observation on $TiO_2$ nanotubes [2].

***XRD Measurement***

Phase transition and crystallization of annealed $ZrO_2$ nanotube samples were confirmed by X-ray diffraction analysis data (Rigagu Gelgerflex model D/Max-IIB) using a maximum potential of 50 kV and current of 32 mA.

***Osteoblast Cell Culture***

For these studies, MC3T3-E1 mouse osteoblast cells (CRL-2593, subclone 4, ATCC, USA) were used. Each 1 ml of cryo-conserved stock was mixed with 10 ml of alpha minimum essential medium (αMEM; Invitrogen, USA) in the presence of a volume fraction of 10 % fetal bovine serum (FBS; Invitrogen, USA) and a volume fraction of 1 % penicillin-streptomycin (PS; Invitrogen, USA). The cell suspension was plated in a polystyrene cell culture dish and incubated at 37° C in a volume fraction of 5 % $CO_2$ environment. Each 1.27 × 1.27 $cm^2$ experimental substrate ($ZrO_2$ nanotubes or flat Zr) was placed into individual wells of a 12-well polystyrene plate. The polystyrene (PS) culture dish was used as a control. When the cells reached confluency, the MC3T3-E1 osteoblastic cells were seeded at a concentration of $5\times10^4$ cells per well onto the experimental

substrates and stored in a $CO_2$ incubator for the experimental time durations. For experimental time points of 14 d of culture, cell media was changed at 7 d to osteogenic induced media, aMEM containing a volume fraction of 10 % FBS, a volume fraction of 1 % PS, 10 nmol/L dexamethasone (Sigma, USA), 150 µg/ml ascorbic acid (Sigma, USA) and 10 mmol/L β-glycerol phosphate (Sigma, USA). All experimental substrates were moved to a new 12-well dish before cell assays were performed in order to isolate the cells on the substrate of interest from cells on the surrounding polystyrene dish.

***Cell Spreading and Viability Test***

Fluorescein diacetate (FDA; Sigma, USA) staining was conducted to visualize viable cells and to measure cell spreading. At 24 and 48 h after plating, the cells on the substrates were washed with phosphate-buffered saline (PBS, pH 7.4, Invitrogen, USA) and incubated for approximately 30 seconds with FDA stock (5 mg dissolved in 1 ml of acetone) dissolved in PBS (10 µl/10 ml), and washed once more. The samples were then inverted onto coverslips, mounted, visualized and photographed using a fluorescence microscope with a FITC (494 nm excitation) filter (DM IRB, Leica, Co., USA).

***Data Analysis for Adhered Cell Count and Cell Spreading Area***

To quantify the number of adhered cells and the differences in cell morphology observed in the FDA staining results, the stained cells were outlined by using Image J software, a public domain image processing and analysis program developed by the NIH. The number of adhered cells and the total cell spreading area were measured by Image J analysis functions. The experiment was repeated in triplicate, and each sample was analyzed in six distinct areas.

***Immunofluorescence of Cytoskeletal Actin***

After 48 h of culture, the cells were fixed in 4 % paraformaldehyde in PBS for 15 min at room temperature. Once fixed, the cells were washed twice with wash buffer (PBS containing a volume fraction of 0.05 % Tween-20). To permeabilize the cells, 0.1 % Triton X-100 in PBS was added for 10 min, followed by washing twice with wash buffer. TRITC-conjugated phalloidin (1:1000 Chemicom International) in PBS was added and incubated for 1 h at room temperature, after which the cells were washed three times with wash buffer for 5 min each wash. Samples were then inverted onto coverslips with a dab of Fluoromount-G (Electron Microscopy Sciences, USA), visualized and photographed using a Rhodamine (536 nm excitation) filter by a fluorescence Leica, Co. DM IRB microscope.

***MTT Assay***

To estimate the metabolic activity of the cells, an MTT (3-(4,5-dimethylthiazole-2-yl)-2,5-diphenyl tetrazolium bromide) assay was employed. After the selected incubation periods, the samples were washed by PBS and transferred to a new 12-well polystyrene culture plate. Fresh cell culture media was added to each well, and the MTT dye agent was added in an amount equal to 10 % of the culture media volume, according to manufacturer's instructions (MTT kit, Sigma, USA). After 2 h of incubation in a 5 % $CO_2$ incubator, 1 ml of solubilizing solution was added to each well and the polystyrene plate was shaken for 30 sec. The fluorescent absorbance of each solution was measured at a wavelength of 570 nm with the subtraction of the 650 nm background by ultraviolet-visible (UV-vis) spectrophotometer (Biomate™ 3, Thermo Electron Co., USA).

***Alkaline Phosphatase Activity Test***

In order to measure the bone forming ability of cells on the experimental surfaces, the alkaline phosphatase (ALP) activity was detected using a colorimetric assay kit. Briefly, after the selected incubation periods, the samples were washed by PBS and transferred to a new 12-well polystyrene culture plate. Cells were then gently washed twice with phosphate buffer provided by the kit supplier, followed by the

addition of a volume fraction of 0.2 % triton X-100 in phosphate buffer. The adherent cells were further scraped off of the sample substrate and collected in a microcentrifuge tube. Cell suspension was incubated on ice for 10 min under agitation, and then centrifuged at 2500 × g for 10 min at 4° C. The supernatants were stored at -80° C until further analysis by AnaSpec SensoLyte pNPP Alkaline Phophatase Assay Kit colorimetric assay (AnaSpec, Inc., USA) following the manufacturer's instructions. The ALP values were normalized by protein content obtained by a BCA kit (Sigma, USA).

***Matrix Mineralization***

Alizarin red staining was employed to assess the ability of osteoblast cells to produce mineralized matrix. After 14 d of culture, the cells were washed by PBS and transferred to a new 12-well polystyrene culture plate. The cells were then fixed using a mass fraction of 2.5 % gluteraldehyde (Sigma, USA) for 1 h at room temperature. Once fixed, the cells were washed three times with PBS for 10 min each wash. Alizarin red solution was prepared using a mass fraction of 2 % alizarin red S (Sigma, USA) in distilled water, and the pH was adjusted to 4.2 using a volume fraction of 10 % ammonium hydroxide. Alizarin red solution was added and incubated for 1 min at room temperature, and washed three times with

PBS. The samples were then photographed using a digital camera (Canon, USA).

Matrix mineralization was also analyzed by energy dispersive X-ray spectroscopy (EDX) after 14 d of culture. After the experimental culture time was complete, the cells were trypsinized by trypsin EDTA 0.25 % (Invitrogen, USA) and allowed to air dry for SEM and EDX analysis. Identical samples were incubated in cell-free media as a control. The Oxford EDX attachment and Inca Software were used to determine elemental composition of deposited bone matrix.

***Statistical Analysis and Error Bars on Graphs***

Sigma Plot 11.0 software (2008) was utilized to demonstrate the statistical significance of the assays. The graphs show the average ± standard error bars associated, with *p*-values listed in the figure captions.

## 3.1.2 Results and Discussion

Previously, we have demonstrated an accelerated osteoblast proliferation rate and up-regulated alkaline phosphatase (ALP) activity on $TiO_2$ nanotubes compared to flat Ti [1-2]. Since the advantages of a nanotube morphology have been well-concluded on $TiO_2$, the primary focus of this work was to observe the effects of similar $ZrO_2$ nanotopography on osteoblasts. **Figure 3.1-1(a)** shows SEM micrographs of the flat Zr, the top-view of the $ZrO_2$ nanotubes and the cross-sectional

nanotube view after sample cleavage, respectively. The self-assembled nanotube layers were generated using a two-step anodization method of Zr sheets [75]. The images show highly ordered, vertically aligned nanotubes with a pore size of roughly 40 nm, and a length of 10 μm. Flat substrates of Zr with a native $ZrO_2$ oxide layer having a chemical composition analogous to that of the $ZrO_2$ nanotube surface were used as non-textured comparative surfaces. Polystyrene culture dishes were used as a control. The nanotube system possesses unique features that may contribute to possible benefits in the application of enhanced bone cell function in vivo [82]. For instance, a more defined, reproducible and reliable surface texturing is produced by electrochemical anodization in comparison to other micro- and macro-roughening techniques due to the self-assembly mechanism by which the anodization occurs. In addition, the nanotube architecture possesses a closed-end pore volume inside the tubes, as well as an interstitial volume between the nanotube walls which, as previously suggested [2], may allow for continued flow of culture media to the cells even after cell adhesion or confluency, enabling increased exchange spaces for gas, nutrients and cell signaling molecules, to possibly give an enhanced cell environment.

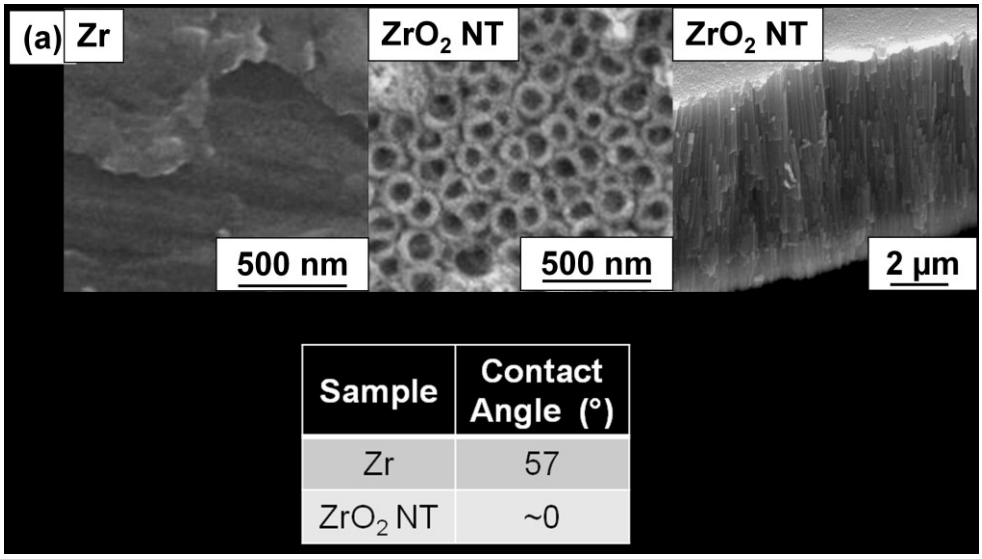


| Sample | Contact Angle (°) |
|---|---|
| Zr | 57 |
| $ZrO_2$ NT | ~0 |

**Figure 3.1-1.** Physical characterization of different experimental surfaces. **(a)** SEM micrographs of the top view of the flat Zr and $ZrO_2$ nanotubes, and the cross-sectional view of the nanotubes after sample cleavage. **(b)** Table with the surface wettability contact angle measurements for flat Zr vs. $ZrO_2$ nanotube surfaces.

The experimental surfaces were characterized by contact angle measurements (**Figure 3.1-1 (b)**). The $ZrO_2$ nanotube surface was found to be extremely hydrophilic, with a measured contact angle of zero degrees. In contrast, the contact angle on the flat Zr was measured to be 57 °. $ZrO_2$ nanotubes are superhydrophilic presumably due to the nature of the $ZrO_2$ oxide surface chemistry and wettability, similar to the well-known hydrophilic nature of the $TiO_2$ nanotubes[2]. Hydrophilic biomaterials are found in general to promote protein adsorption [83] and cell adhesion [84]. In addition, it can be speculated that the hydrophilic properties of the nanotube surface would encourage cell media to penetrate into the tubes via capillary effects [85], enabling the interstitial volume to act as a continuous supply of nutrients for the cells.

As described in Section 2.3.1, the as-formed $ZrO_2$ nanotubes were heat treated at 300° C for 6 h in order to reduce residual fluorides, and to crystallize the as-fabricated amorphous structured $ZrO_2$ nanotubes into a cubic structure [45]. X-ray diffraction (XRD) measurements were performed to confirm the crystal structure after annealing. The XRD pattern (**Figure 3.1-2**) indicates that both cubic $ZrO_2$ (red) and hexagonal Zr (green) are present. The intense peaks indicating a large amount of Zr are reasonable considering that the underlying bulk Zr substrate. When comparing the experimental pattern with the Zr pattern (green), there are missing peaks noted at around 37° and 80° values of 2-θ, corresponding to the (100) and (200) planes, respectively. Since Zr has a hexagonal close packed (HCP) structure, the (100) and (200) planes are identical, which explains why both peaks are missing on the experimental pattern. Since the Zr component corresponds to the bulk of the nanotube sample, it is reasonable to assume that the bulk Zr has insufficient randomness, leading to missing peaks in the diffraction pattern. The fact that the peak intensities of the experimental pattern and the Zr pattern do not match also indicates that the sample is insufficiently random.

When comparing the experimental pattern with the $ZrO_2$ pattern (red), one can note correlating peak intensities, indicating that the patterns are a good match. In addition, the peaks in the experimental

pattern corresponding to $ZrO_2$ reveal peak broadening when compared to the Zr peaks, which indicates that the $ZrO_2$ face centered cubic (FCC) crystal structure is mainly present in the nanotubes, and not in the bulk. This effect can be seen clearly by comparing the (102) green and (220) red peaks at around 60°. In addition, the left shoulder apparent on the (002) Zr peak at ~40° is likely due to broadening of the (200) $ZrO_2$ peak.

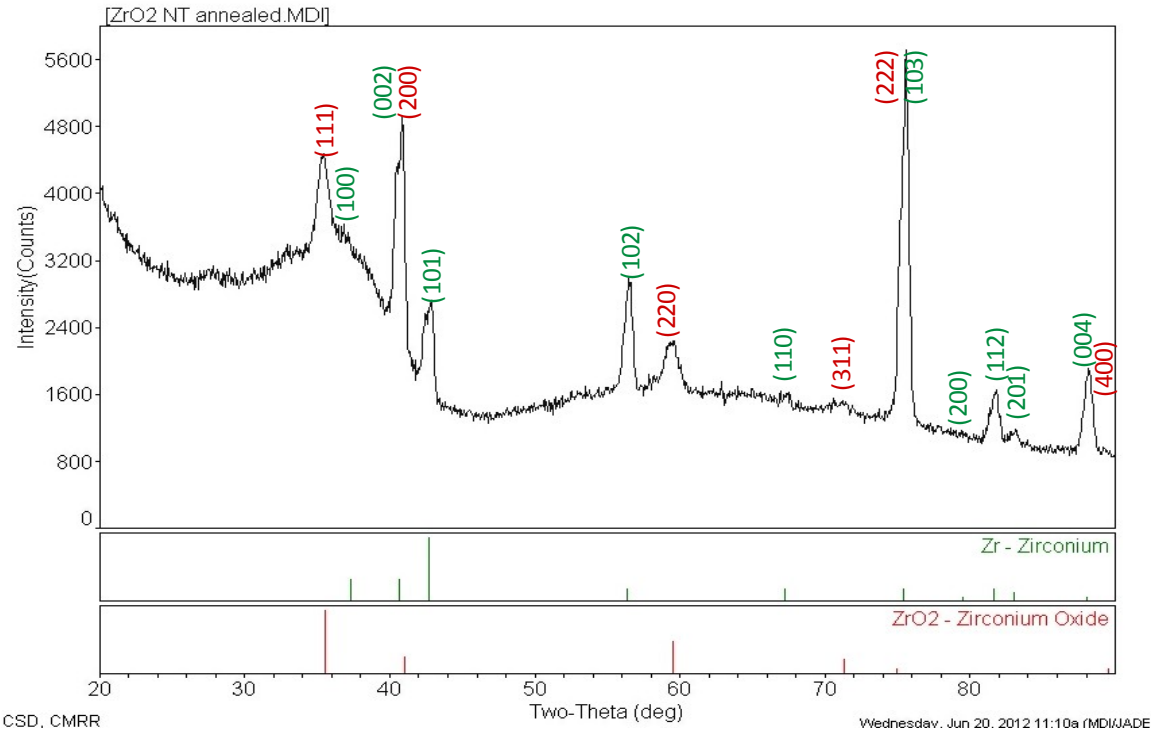


**Figure 3.1-2.** X-ray diffraction pattern of a $ZrO_2$ nanotube sample after annealing at 300 °C for 6 h shows the presence of tetragonal $ZrO_2$ (red pattern) and hexagonal Zr (green pattern). The mixed structure is expected due to the underlying bulk Zr substrate.

**Figure 3.1-3** presents quantitative cell number and spreading analysis of the adhered osteoblasts on the comparative substrates at 24 and 48 h of culture. FDA viability staining results were quantified using Image J image analysis software, and are depicted in **Figure 3.1-3(a)** and

**(b)**. The number of adhered osteoblasts was found to be significantly higher on the $ZrO_2$ nanotube samples when compared to flat Zr at both time points. Furthermore, a significantly greater cell spreading area was revealed on the $ZrO_2$ nanotube surface over flat Zr. Visual comparison of the FDA viability staining of cells on each substrate at 24 h of culture (**Figure 3.1-4**) confirms evidence of greater cell spreading area on the $ZrO_2$ nanotube surface. In contrast, the cells on the flat Zr appear to be balled up and even clumped together, indicating that they may prefer to adhere to each other rather than the flat Zr substrate. 3-D imaging of the cell clusters would provide further insight to what is occurring at the surface. It would be worthwhile for future studies to include such experimentation.

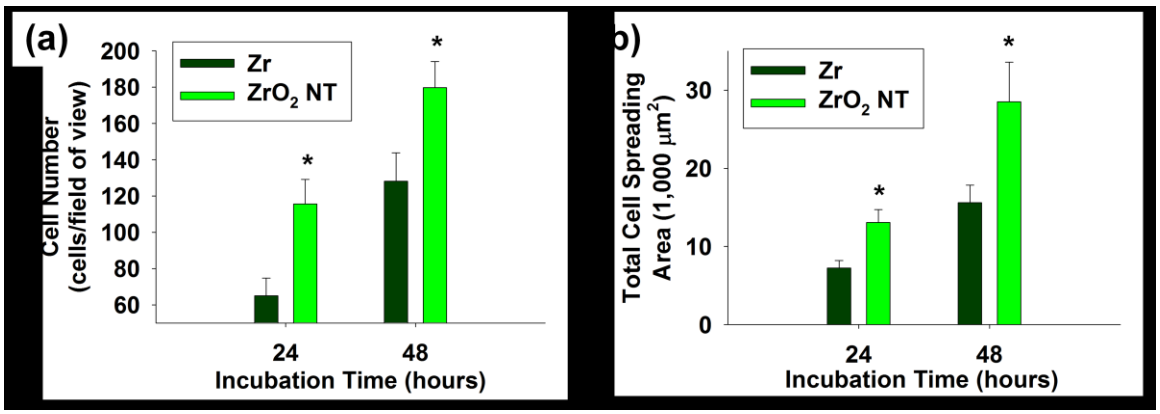


**Figure 3.1-3.** Comparative cell number and spreading analysis. **(a)** Cell number vs. incubation time, **(b)** Cell spreading area vs. incubation time. The bar graph shows the mean ± standard error bars. The *p*-values after performing an ANOVA test reached statistical significance ($p < 0.005$): * indicates a significant difference between $ZrO_2$ nanotube substrates and flat Zr.

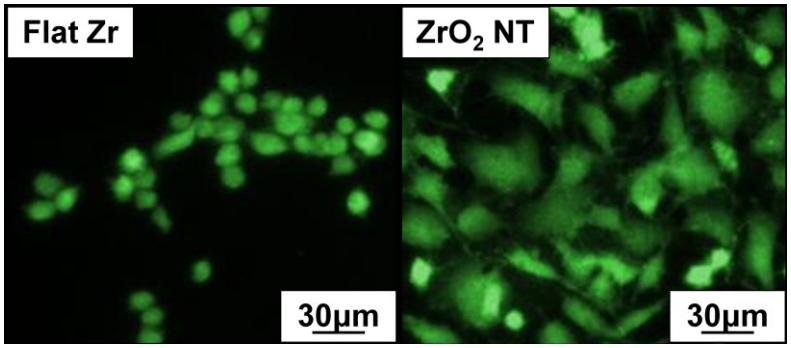


**Figure 3.1-4.** FDA viability staining of osteoblast cells on flat Zr vs. $ZrO_2$ nanotube ($ZrO_2$ NT) substrates, revealing larger cell area observed on the nanotubes.

It is well known that the manner with which a cell adheres and spreads on a biomaterial is highly dependent on the presence and placement of adhesion proteins on a surface [84]. It has been previously suggested that the nanotube topography encourages cell spreading due to the adsorption of proteins only on the nanotube wall rims, thus inducing a fixed distance between proteins and encouraging the cell to spread in order to find adhesion proteins [2]. Prior studies have also shown an enhanced initial protein adsorption on a nanostructured zirconia surface due to strong electrostatic interactions [86]. This trend was confirmed on our $ZrO_2$ nanotube surface in a protein adhesion study after 2 h of incubation in cell culture media. A significantly higher amount of protein was measured on the nanotube surface when compared to the flat Zr and control polystyrene (**Figure 3.1-5**). It is also probable that the hydrophilic nature of the nanotube substrate has an effect on the cell adhesion and spreading. Since cell attachment and adherence are the

first phases of cell response to a biomaterial, it can be hypothesized that the nanotubular surface instigates a preferred initial cell response.

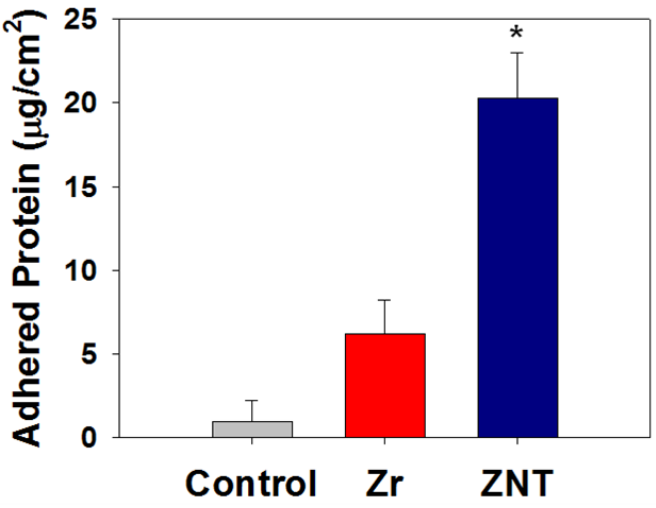


**Figure 3.1-5.** Relative amounts of adhered protein after 2 h of incubation in cell culture media. The bar graph shows the mean ± standard error bars. The *p*-value after performing an ANOVA test reached statistical significance ($p < 0.001$): * indicates a significant difference between $ZrO_2$ nanotube substrates and all other samples.

Immunofluorescent staining of the cytoskeletal actin in osteoblast cells cultured on each experimental substrate is shown in **Figure 3.1-6**at 48 h of culture. While there is evidence of prominent stress fiber formation on both substrates, a distinct difference can be observed in the cytoskeletal organization by visual comparison. The cells appear to form a stretched, multi-layer matrix of cells with crisscross patterned actin on the nanotube surface, versus an organized, single layer of cells on flat Zr. Additionally, the cells on the flat Zr surface exhibit fine stress fibers, whereas on the nanotube surface F-actin bundles formed contractile stress fibers, as

indicated by the yellow arrows (**Figure 3.1-6**). The contractile stress fibers and stretched, crisscross pattern apparent on the nanotube substrate could be evidence of intracellular tension which supports the formation of a well-developed cytoskeleton and cell spreading [87]. Furthermore, the transition from fine filaments of F-actin under no tension to thick contractile stress fibers is said to be a result of initial attachment of integrins to matrix ligands, triggering the activation of cell signaling molecules and eventually allowing for acto/myosin contraction [88]. The presence of contractile stress fibers on the nanotube substrate may indicate that the maturation of the cells is enhanced by the material topography.

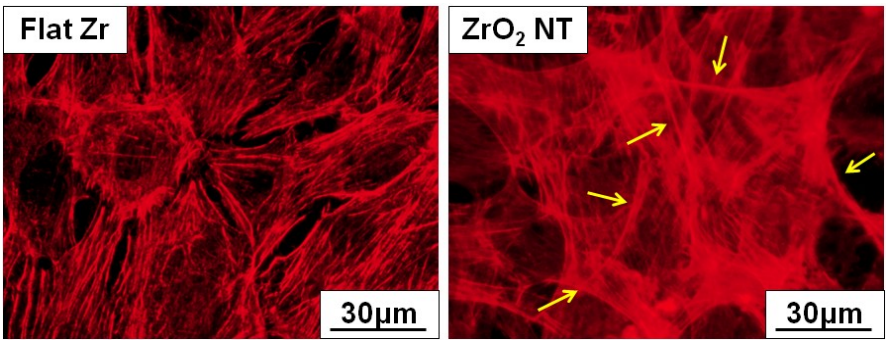


**Figure 3.1-6.** Immunofluorescent images of cytoskeletal actin for osteoblast cells on flat Zr vs. $ZrO_2$ nanotube substrates. The images suggest that the nanotube substrate induces a cytoskeleton with crisscross patterned actin and contractile stress fibers (yellow arrows).

SEM micrographs of the adhered osteoblasts on flat Zr and $ZrO_2$ nanotubes after 24 h of incubation time are presented in **Figure 3.1-7**. On the flat Zr, the cells have very few cellular extensions or filopodia, whereas those cultured on the $ZrO_2$ nanotube surface possess significantly more

cellular extensions and filopodia propagation from the leading edges (red arrows). Evidence of more filopodia on the nanotube surface indicates that the cells may be reacting to the nanotopography by filopodial sensing. These trends in cell morphology are in agreement with the trends observed in our previous studies of osteoblast culture on $TiO_2$ nanotube surfaces [2] as well as other studies which have analyzed cellular sensing of nanotopography via filopodia interaction [40]. It can be speculated that in both the $TiO_2$ and $ZrO_2$ nanotube cases, the cell-substrate interaction allows for an enhanced dynamic propagation and an overall increase in osteoblast activation, as indicated by the filopodia.

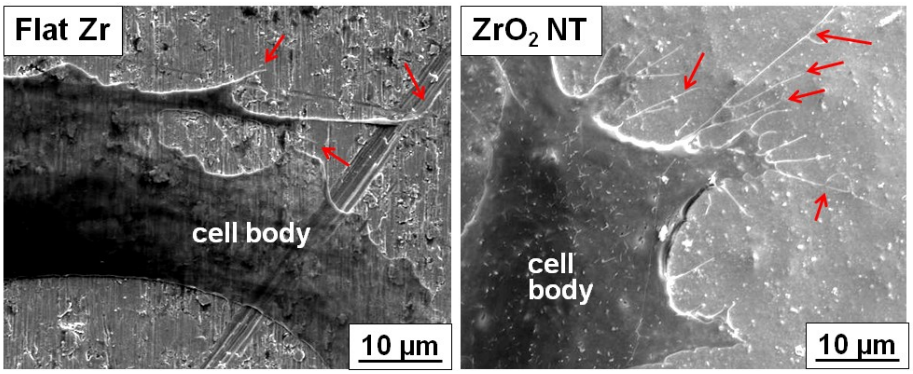


**Figure 3.1-7.** SEM micrographs of osteoblast cells cultured on flat Zr and $ZrO_2$ nanotube surfaces. The red arrows highlight filopodia extending from the cells.

An MTT assay was utilized in order to measure the metabolic activity of the cells and to indirectly estimate the number of viable cells. The MTT results shown in **Figure 3.1-8(a)** reveal a significant difference between the flat Zr and the $ZrO_2$ nanotube surface at 24 and 48 h of incubation time. In addition, the trend observed in **Figure 3.1-8(a)** is comparable to the

trend revealed in the graph of the number of adhered cells as a function of incubation time (**Figure 3.1-3(b)**).

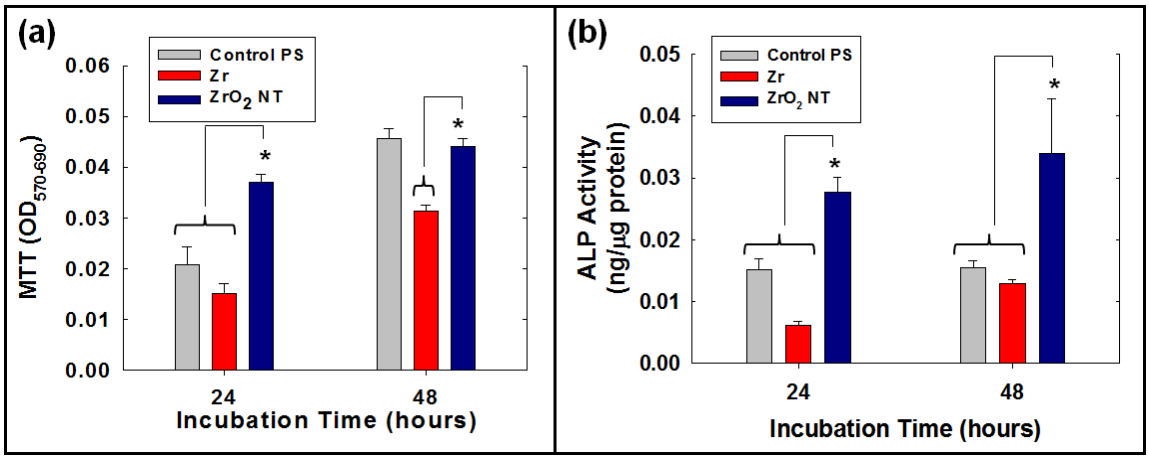


**Figure 3.1-8. (a)** MTT assay data showing the optical density (OD) of the reaction product of the MTT working solution and **(b)** ALP activity of osteoblast cells cultured on the control polystyrene (PS), flat Zr and $ZrO_2$ nanotube (NT) surfaces at 24 and 48 h of incubation. The bar graphs show the mean ± standard error bars. The *p*-values after performing a ANOVA test reached statistical significance ($p < 0.001$): * indicates a significant difference between $ZrO_2$ nanotube substrates and the bracketed groups.

The osteogenic functionality of the osteoblasts was assessed by measuring the alkaline phosphatase activity, an *in vitro* marker of bone formation, on each substrate. **Figure 3.1-8(b)** illustrates the ALP activity as a function of incubation time. There was found to be a significant increase in the ALP activity of the osteoblasts on the $ZrO_2$ nanotubes at both 24 and 48 h of incubation. This evidence of an up-regulation of ALP activity on the nanotube substrate supports the hypothesis that the $ZrO_2$ nanotube surface may induce early bone formation in osteoblast cells when compared to cells cultured on the flat Zr surface. It is also important to note that both the cell number (**Figure 3.1-3(b)**) and MTT data (**Figure**

**3.1-8(a)**) demonstrate a decrease in the $ZrO_2$ nanotube proliferation rate when compared to the proliferation rate on flat Zr. This trend of decreased proliferation on the nanotube surface also coincides with the increase in ALP activity, which is in agreement with the inverse relationship between growth and differentiation that many cell types exhibit *in vitro*. Investigations of osteoblast developmental stages have reported that proliferating osteoblasts demonstrate decreased expression of their phenotypic activities during rapid growth, while they begin to produce more ALP and other markers of osteoblast activity when cell replication rates slow down [89].

It is important to detect the ability of osteoblast cells to perform matrix mineralization, the final event of *in vitro* osteogenesis, in order to determine proper maturation of the cells. Alizarin red S staining, an early stage marker of calcium deposition by osteoblast cells, was used in these studies. Calcified extracellular matrix was detected after 14 d of culture on both experimental substrates, however it appeared to be more uniformly distributed in a dark red color on the $ZrO_2$ nanotube surface (**Figure 3.1-9**). In addition, SEM analysis after 14 d of culture revealed large areas of granular deposits on the nanotube substrate, which was present in lesser amount on the control Zr (**Figure 3.1-10(a)**). Upon close examination of the $ZrO_2$ NT image in **Figure 3.1-10**, the presence of small

pores is apparent. These pores are probably showing the underlying nanotube pore openings. The amount of mineralized matrix covering the nanotubes makes it difficult to see the nanotubes underneath. In contrast, the surface of the flat Zr does not appear to be altered much except for a few granules (indicated by yellow arrows). These results agree with previous findings which demonstrate an increased matrix production stimulated by a $TiO_2$ nanotube substrate [90-91]. Furthermore, the results of EDX analysis of the same 14 d samples compared to identical samples immersed in cell-free media (**Figure 3.1-10(b)**) revealed significantly higher amounts of calcium and phosphorus mineral elements (indicators of bone matrix formation) on the $ZrO_2$ nanotube surface. When interpreting the EDX data, one must consider that the elements Zr and P have overlapping peaks (at 2.040 and 2.013 keV, respectively). This is a probable explanation for the unusually high amount of P present, when compared to the standard Ca:P ratio of hydroxyapatite (1.61). Thus, the EDX data is simply a verification of the presence of Ca and P minerals on the surface in relative amounts. This evidence of mineralized matrix after only 14 d of culture suggests that the $ZrO_2$ nanotube substrates have favorable effects on the ability of the osteoblast cells to mature when compared to the flat Zr substrate. These results are analogous to a study by Guo and coworkers which demonstrated an enhanced

bioactivity on the $ZrO_2$ nanotube surface by the formation of bone-like apatite in simulated body fluid immersion experiments [92]. Another study by Popat and coworkers showed similar increases in calcium and phosphorus content on $TiO_2$ nanotubes when compared to flat Ti [90]. In order to obtain further understanding of the bioactivity of our nanotube surface, the observations of matrix mineralization presented here should be confirmed in further studies by assessing ALP activity at later time points (beyond 48 h).

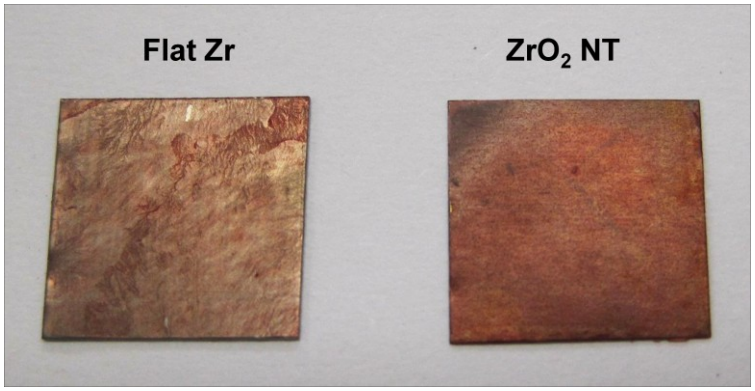


**Figure 3.1-9.** A photograph of matrix mineralization Alizarin red stain of osteoblast cells on the flat Zr and $ZrO_2$ nanotube substrates after 14 d of culture.

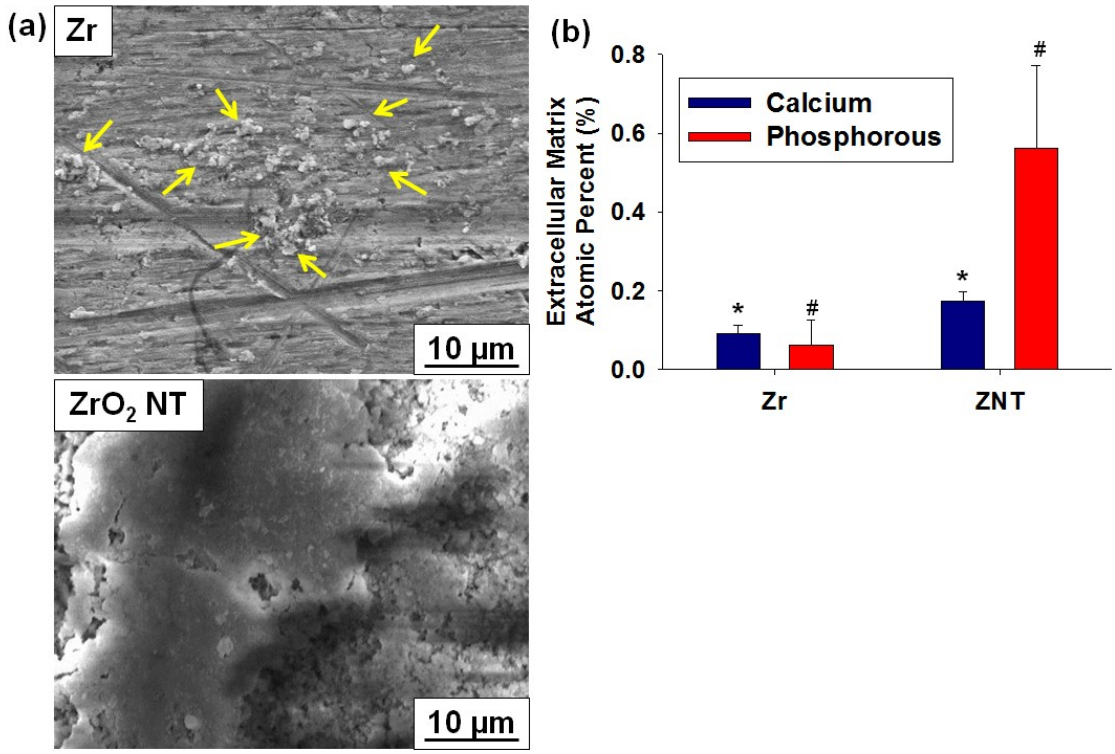


**Figure 3.1-10. (a)** Extracellular matrix mineralization evaluation after 14 d of culture by scanning electron microscopy of matrix deposition on the flat Zr and $ZrO_2$ NT surfaces. There is some evidence of mineralized matrix on the flat Zr (yellow arrows), however the $ZrO_2$ NT surface is totally covered by mineralized matrix. **(b)** EDX analysis of the atomic percent of calcium and phosphorous mineral elements on the surfaces. The bar graphs show the mean ± standard error bars. The *p*-values after performing an ANOVA test reached statistical significance ($p < 0.05$): * and # indicate a significant difference between $ZrO_2$ nanotube substrates and flat Zr for calcium and phosphorous, respectively.

## 3.2 Conclusions & Future Directions

The intention of this study was to contribute toward improved osseointegrative surfaces, in particular for total knee replacement implant applications. Based on our findings, the $ZrO_2$ nanotube surface may provide valuable advantages over a flat Zr surface containing a native oxide layer of $ZrO_2$ in prompting an enhanced osteoblast cell response. The results presented here revealed similar trends to previously published

data on $TiO_2$ nanotube substrates. However, a direct comparison of the $ZrO_2$ and $TiO_2$ nanotube substrates would be an interesting and necessary avenue of future work. In addition, the present results were limited to a single length of nanotube. This was due to a common complication found among anodized nanotubes, in which a thicker oxide nanotube layer tends to cause delamination of the nanotube layer due to the stress accumulations. It will be interesting to study the effect of nanotube layer thickness on cell growth properties and mechanical properties (resistance to delamination, etc.), which will be reported in future publications.

In the present work we investigated the behavior of MC3T3-E1 osteoblast cells on vertically aligned, laterally spaced $ZrO_2$ nanotube structures. An overall improved bone cell response was observed on the nanotube substrate when compared to a flat Zr surface, including both the initial cellular response as well as bone cell maturation at further time points. Cell adhesion and spreading were significantly improved on the nanotube surface, in addition to the formation of a highly organized cytoskeleton with crisscross pattern actin. The cells cultured on the nanotube substrate also gave rise to increased ALP activity and the formation of a concentrated calcified extracellular matrix, both implications of improved osteoblast functionality and mineralization. This $ZrO_2$ nanotubular surface has substantial implications as an improved

osseointegrating biomedical material surface because of its large surface area and unique nanoscaled geometry which prompted an improved osteoblast response. The investigation of innovative nanotopographies of various metal-oxide materials, such as is presented in this chapter, offers significant advancement for the design of bone implant surface technologies.

*Chapter 3 is a reprint in part of the material as it appears in Materials Science & Engineering C Volume 31 (8), 2011, Page 1716 written by Christine J. Frandsen, Karla S. Brammer, Kunbae Noh, Laura S. Connelly, Seunghan Oh, Li-Han Chen, and Sungho Jin. The dissertation is the primary investigator and author of this publication.*

# CHAPTER 4

## 4. Direct Comparison of Nanotube Architecture with Various Surface Chemical Modifications

Current research in the orthopedics industry to a large extent has been concentrated on advanced surface technologies that would instigate biological fixation, enhancing patient healing time and reducing chance for aseptic loosening. An increasing number of studies have shown that cells respond to minute changes in surface characteristics such as wettability [27], surface roughness [25-26], surface energy [93], nanotopography [87, 94-96], and surface chemistry [24]. The ideal orthopedic material surface would be composed of a unique combination of these surface properties, promoting the optimum environment for bone in-growth. A common trend in biomaterials research has been focused especially on the investigation of nanostructured material surfaces, since topographical cues on the nanometer scale have been linked to promoting cellular function and response [97]. However, while nanostructured surface geometries have provided exciting findings in the field of biomaterials research, only a few publications have directly compared nanostructures of various surface chemistries [74]. The history of orthopedic implant materials has made it obvious that the body tissues respond differently to surfaces depending

on the type of foreign material [98]. In fact, it has been proposed that there are two major mechanisms of osseointegration: mechanical interlocking through bone growth in pores (i.e. topography), and biochemical bonding (i.e. surface chemistry) [99]. There remains to be insufficient understanding on how these factors interact in producing biological responses [100]. This is largely due to the difficulty in varying surface chemistry and topography independently. Additionally, i*n vitro* and *in vivo* studies involving surface chemistry are typically multifaceted and complex, due to the multitude of properties that can affect biochemical reactions at the surface (i.e. surface charge, isoelectric point, fluid flow, pH, ionic release from the surface, precipitation of biomolecules from the culture media/biological fluids) [99]. Nevertheless, we believe that a unique combination of surface chemistry and nanostructured geometry may provide a balance of defined characteristics towards an optimal orthopedic implant. Though the majority of related nanotopographical studies compare only nano-textured with non-textured surfaces of the same material, an important addition to this research would be the direct comparison of the same nanostructure with different surface chemistries. The advantages of the $TiO_2$ nanotube surface topography for orthopedic applications have been well outlined in Chapter 1. Since titanium is one of the most

commonly used orthopedic materials in use today, it is of great interest to compare any future materials with a well-recognized industry standard (Ti), in addition to the gold-standard in the Jin Laboratory ($TiO_2$ nanotubes).

## 4.1 Comparative Cell Behavior on Carbon-Coated $TiO_2$ Nanotube Surfaces for Osteoblasts vs. Osteo-Progenitor Cells

Though the majority of related studies compare only nanotextured with non-textured surfaces of the same material, an important addition to this research would be the direct comparison of the same nanostructure with different surface chemistries. Therefore, the studies included in this section and the two following (Section 4.2 and 4.3) were designed to provide a direct comparison of flat Ti and $TiO_2$ nanotubes with the other potential surface chemistries to advance orthopedic implant technology. In order to accomplish this, we have implemented the concept of maintaining constant nanotube geometry (i.e. $TiO_2$ nanotubes with 100 nm diameter as shown in **Figure 2.2-1(a)**) while varying the surface chemistry. The focus of this section is a carbon-coated $TiO_2$ nanotube surface.

Carbon films deposited on metal in both its amorphous and crystalline forms has been investigated as potential biomedical materials, mainly because of its chemical inertness and naturally occurring presence

in the human body [101-103]. The application of carbon films to materials that are sensitive to wear, such as Ti and Si, has been a convenient method that has shown significant potential for implant coating applications [104-110], specifically for orthopedic implants. The effect of a carbon thin film coating on the surface of $TiO_2$ nanotubes is thus of interest, and will be discussed in this section.

### 4.1.1 Experimental Methods

***Nanotube Substrate Fabrication***

$TiO_2$ nanotube surfaces were created using a two-electrode setup, anodization process as described previously [1, 67] . Briefly, a cp-Ti sheet 0.25 mm thick, (Alfa-Aesar, 99.5% metals basis, USA) was used for this process. The nanotubes were prepared in a 1:7 volumetric ratio of acetic acid (≥99.99% purity, Sigma-Aldrich) to 0.5 w/v% hydrofluoric acid in water (EM Science, 48 w/v %, USA) at 20 V for 30 minutes. A platinum electrode (Alfa-Aesar, 99.9%, USA) served as the cathode. The samples were then washed with deionized water, dried at 80˚C, and heat-treated at 500ºC for 2 hours in order to crystallize the as-fabricated amorphous structured $TiO_2$ nanotubes into anatase structure. Carbon **(C)** films were DC-sputter deposited onto $TiO_2$ nanotube substrates from a pyrolytic graphite wafer (99.999 % purity) in a Nor-Cal sputtering system. The base pressure in the chamber before sputtering was 5 X $10^{-7}$ mTorr. During sputtering, the

bleeding pressure was set to 3 mTorr, and the DC power was 100 W. The carbon layer thickness is about 30 nm determined by sputtering rate and time. The nanotubes were visualized under a SEM (scanning electron microscope) (XL30, FEI Co., USA). The Oxford EDX attachment and Inca Software determine elemental make up and composition of the surface, where the carbon coated surface showed a clear carbon peak and there was an increased weight percent of elemental carbon on the surface after deposition. The $TiO_2$ and C coated nanotube samples (1.27×1.27 $cm^2$) used for all experiments were sterilized by autoclaving before usage.

***Contact Angle Measurement***

The measurement of contact angle for the $TiO_2$ and C nanotube surfaces was carried out by a video contact angle measurement system Model No. VSA 2500 XE (by AST Products, Inc.). A small amount of D.I. water droplet (~ 3mg) was placed on the nanotube surfaces to measure static contact angle. The measurement of contact angle is a simple method for analyzing the surface energy and the hydrophilic nature of the surface. In this case, we also wanted to verify that the carbon (more hydrophobic in nature compared to $TiO_2$) was deposited and observe the change in surface energy after deposition.

***Osteoblast Cell Culture***

For these studies, MC3T3-E1 mouse osteoblast (CRL-2593, sub-clone 4, ATCC, USA) were used. Each 1 mL of cells was mixed with 10 mL of alpha minimum essential medium (a-MEM; Invitrogen, USA) in the presence of 10% v/v fetal bovine serum (FBS; Invitrogen, USA) and 1% v/v penicillin-streptomycin (PS; Invitrogen, USA). The cell suspension was plated in a cell culture dish and incubated under 37˚C, 5% v/v $CO_2$ environment. When the concentration of the MC3T3-E1 osteoblastic cells reached ~ $3\times10^5$ cells/mL, they were seeded onto the experimental substrate of interest ($TiO_2$ or C) which were placed on a 12-well polystyrene plate, and stored in a $CO_2$ incubator until the time of the assays. The concentration of the cells seeded onto the specimen substrate was $1\times10^4$ cells/well. For long term culture, media was changed every 3 days.

***Mesenchymal Stem Cell Culture***

Human mesenchymal stem cells (hMSCs) were obtained from Lonza Corporation. The cell growth media were composed of a-MEM (Invitrogen), 10 % FCS (Invitrogen), 100 units/ml penicillin and 100µg/ml streptomycin (Invitrogen). Growth media was used on all experimental surfaces. For preparing positive control for PCR purposes, osteogenic inducing media were also prepared by adding 10 nM dexamethasone

(Sigma), 150 μg/ml L-Ascorbic acid (Sigma), and 10 mM beta-glycerophosphate (Calbiochem) to cell growth media [3, 111-112]. Culture protocol was identical to the osteoblast culture methods as described above.

***MTT (3-(4,5-dimethylthiazole-2-yl)-2,5-diphenyl tetrazolium bromide) Assay***

MTT test was used to determine the amount of adhered viable cells and cell proliferation. After the selected incubation periods, the square samples ($TiO_2$ vs. C) were washed by phosphate buffered solution (PBS, Invitrogen, ph 7.4) and transferred to a new 12-well polystyrene culture plate to isolate and analyze only the cells on the experimental surface. 1 mL of fresh media and 0.1ml of MTT reagent (according to the manufactures directions, MTT kit, Sigma, USA) was added to each well. After 2 hours of incubation in 5% $CO_2$ incubator, 1 mL of solubilizing solution was added to each well and the plate was shaken to dissolve all the formalized crystals. The absorbance of each solution was measured at the wavelength of 570 nm with the subtraction of the 650 nm background by UV-VIS spectrophotometer (BiomateTM 3, Thermo Electron Co., USA).

***Immunofluorescence of Cytoskeletal Actin***

After 24 hours of culture, the cells on the experimental surfaces were fixed in 4% paraformaldehyde in 1X PBS for 15 minutes at room

temperature. Once fixed, the cells were washed twice with 1X wash buffer (1 X PBS containing 0.05% Tween-20). To permeabilize the cells 0.1% Triton X-100 in 1X PBS solution was added for 10 minutes. The cells were washed twice with wash buffer. TRITC-conjugated phalloidin (1:1,000, Sigma, USA) in 1X PBS was added and incubated for 1 hour at room temperature. The cells were washed three times with 1X wash buffer for 5 minutes each wash. The samples were then inverted onto glass slides with a dab of Fluormount-G (Southern Biotech), visualized and photographed using a red (actin) filter by a fluorescence LEICA DM IRB microscope.

***Scanning Electron Microscopy (SEM) for Cell and Substrate Observation***

In order to observed high resolution cell features of cells grown on the nanotube surfaces, SEM was employed. After a culture time of 24 hours, the cells on the substrates were washed with PBS and fixed with 2.5 w/v% glutaraldehyde (Sigma, USA) in PBS for 1 hour. After fixation, they were washed three times with PBS for 10 minutes each wash. Then the cells were dehydrated in a graded series of ethanol (50, 70, 90, and 100 %) for 30 minutes each and left in 100% ethanol until they were dried by critical point dryer (EMS 850, Electron Microscopy Science Co., USA). Next, the dried samples were surface metalized by sputter-coating with cobalt/chrome for SEM examination. The morphology of the samples as

well as that of the adhered cells were observed using SEM (XL30, FEI Co., USA).

***Alkaline Phosphatase (ALP) Activity Test***

To measure the bone forming ability of cells on the experimental surfaces, after the selected incubation periods, the samples ($TiO_2$ vs. C) were washed by PBS and 500 µL of 0.2 w/v % triton X-100 (Sigma, USA) was added to each well to study the lysis of cells. Using a cell scraper the lysate was collected and agitated on ice for 10 minutes, followed by centrifugation for 10 minutes at 4°C. The supernatants were stored at -60°C until further analyzed by AnaSpec SensoLyte pNPP Alkaline Phophatase Assay Kit colorimetric assay (AnaSpec, Inc.) following the manufacturer's instructions. The ALP values were normalized by protein content obtained by a BCA kit (Pierce Protein Products, Thermo Scientific).

***ALP Staining and Semi-Quantification of Osteoblast Cells***

ALP staining kits (Sigma, USA) are intended for the semi-quantitative demonstration of alkaline phosphatase activity. For ALP staining, the cells grown on the experimental substrates and stained following the manufacturer's instructions. Briefly, the cells were incubated in a mixture of naphthol AS-MX phosphate alkaline solution with fast blue RR salt. The resulting blue, insoluble, granular dye deposit indicates sites of alkaline phosphatase activity. The samples were then visualized (through a blue

filter) and photographed using a fluorescence LEICA DM IRB microscope. In order to quantify the sites of ALP activity based on the positively stained area on the experimental surface, the microscopic fields were analyzed using Image J software, a public domain image processing and analysis program developed by the NIH.

***Alizarin Red S Staining of MSC cultures***

The degree of osteogenesis was evaluated by staining cultures with alizarin red after . To detect mineralization (calcium deposits), cells were fixed for 20 min with 4% paraformaldehyde and stained overnight at 4°C with 2% (w/v) alizarin red S (Sigma, USA) solution in distilled water, with the pH adjusted to 4.1–4.3 using 0.5% ammonium hydroxide. Afterward, the samples were washed with distilled water with gentle rocking three times for 10 min each. Then the samples were visualized and photographed using a red (actin) filter by a fluorescence LEICA DM IRB microscope. In order to quantify the alizarin red area on the experimental surface, the microscopic fields were analyzed using Image J software, a public domain image processing and analysis program developed by the NIH.

***Real-time PCR***

After 3 weeks of culture, total RNA of the cells on the $TiO_2$ and C coated nanotube substrates were extracted with Trizol (Sigma), and reverse-transcribed into cDNA by qScript™ cDNA Synthesis Kit (Quanta

BioSciences) Real-time PCR was performed by Taqman® Gene Expression Assays (Applied Biosystems), and the information of Taqman® PCR primer is as follows; GAPDH (Hs99999905_m1, Amplicon length : 122), OCN (Hs00609452_g1, Amplicon length : 74) and OPN (Hs00960942_m1, Amplicon length : 63). Real-time PCR were carried out using Taqman® Fast Universal PCR Master Mix and 7900 HT Fast Real-Time PCR System (Applied Biosystems, Foster City, CA). cDNA samples (1 µl for total volume of 20 µl) were analyzed for gene of interest and for house-keeping gene GAPDH. The comparison test of cycle-threshold point was used to quantify the gene expression level of each sample. In this study, all levels of expression were normalized by the level of expression of positive control (hMSCs cultured with osteogenic inducing media).

***Statistical Analysis and Error Bars on Graphs***

Sigma Plot software 11.0 (2008), which specializes in scientific data analysis and presentation, was utilized to demonstrate the statistical significance of the assays. The graphs show the average ± standard error bars and the significance between groups is marked on the graphs.

### 4.1.2 Results and Discussion

The nanotube substrates used in this study were prepared according to standard anodization protocol for the formation of $TiO_2$ nanotubes with 100 nm diameter, and 1:3 aspect ratio. For the carbon-

coated comparative surface, the $TiO_2$ nanotubes were deposited with a thin, conformal layer of carbon by DC sputter deposition methods in order to obtain a nanotube architecture with a carbon surface chemistry. A schematic illustration is included in **Figure 4.1-1 (a)** in order to clarify that the carbon coating was only deposited in a very thin layer onto the nanotube wall rims. SEM images of the comparative surfaces are depicted in **Figure 4.1-1 (b)**, illustrating that the nanotube geometry was not altered in any way by the addition of the carbon coating.

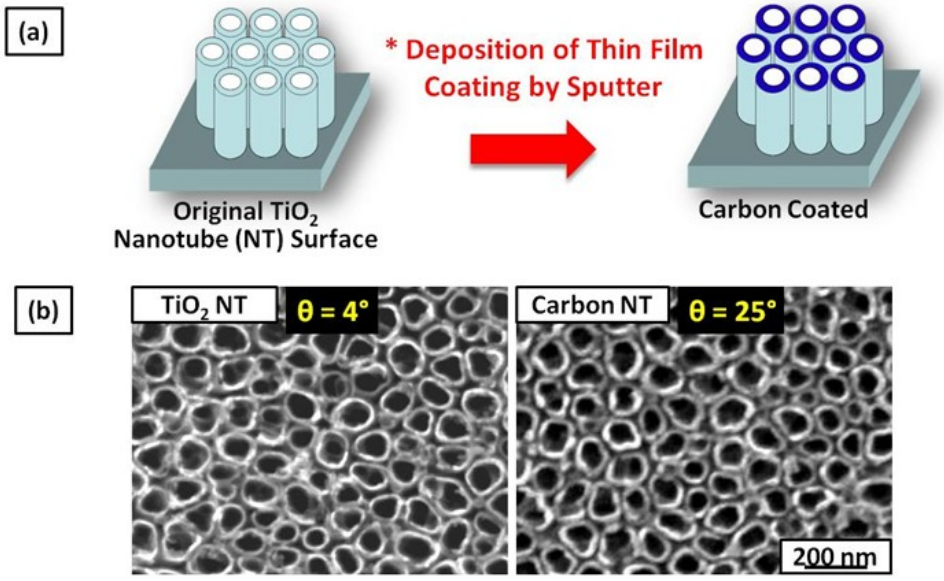


**Figure 4.1-1. (a)** Schematic illustration of nanotube surfaces with different surface chemistry. The original $TiO_2$ nanotube surface was sputter coated with a thin carbon **(C)** film. **(b)** Scanning electron microscopy (SEM) images of the nanotube substrates. The images depict preservation of the nanotube geometry and structure post carbon coating. Shown in yellow is the contact angle for each surface indicating a decrease in hydrophilicity on the C-coated surface from 4 to 25°.

Since cell behavior varies depending on cell type, both osteoblast and osteoprogenitor (mesenchymal stem) cells were plated in this study

onto the experimental surfaces in order to assess their behavior in response to the surface chemistry/nanostructure combination. At early incubation time points, the cellular behavior on the surface *in vitro* includes cell adhesion, growth, and morphological orientation/organization. These three behaviors were assessed via MTT analysis, immunofluorescent cytoskeletal actin staining, and SEM examination (data not shown). The results of each of these assays for both osteoblast and osteoprogenitor cells at early time points (24 and 48 hours) were insignificantly different, which indicates that the carbon versus $TiO_2$ surface chemistry did not affect the initial cell response to the surface. Both cell types adhered and proliferated equally well on both the $TiO_2$ nanotube and carbon-coated nanotube surfaces. In addition, the cell morphology showed no difference.

The ability of osteoblasts and MSCs to mature properly and readily is a vital part of measuring cellular response for bone implant purposes. In this study, the two cell types were cultured for 3 weeks in order to analyze the cells function over time and to determine whether the surfaces were inhibiting or promoting bone function. It should be clarified that the experiments included in this study included the corresponding flat $TiO_2$ and carbon substrates as control surfaces. The nanotube substrates were found to enhance both osteoblast and MSC cellular response when

compared to the flat controls in all aspects of this study, and the data was thus not included.

In order to assess the behavior of the osteoblast cells, the alkaline phosphatase (ALP) activity was measured, which is an enzyme indicative of bone forming ability. Comparative levels of ALP activity on each substrate is presented in **Figure 4.1-2(a)** as a function of incubation time. In order to visually verify the ALP activity quantitative results, the osteoblast cells were also stained using an ALP staining kit, as shown in **Figure 4.1-2(b)**. The qualitative ALP staining was also semi-quantified in **Figure 4.1-2(c)**. Each of the ALP assays depicted here indicates that the bone-forming ability of the osteoblast cells was enhanced on the $TiO_2$ surface chemistry when compared to the carbon surface.

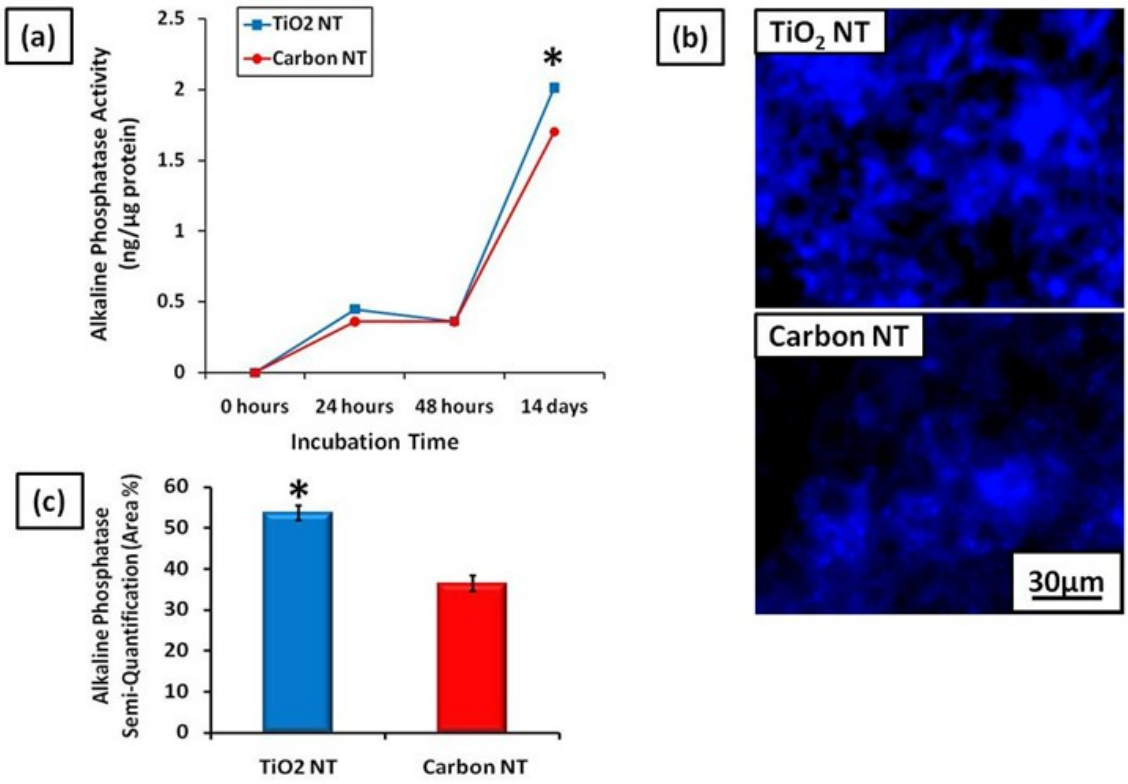


**Figure 4.1-2.** Alkaline phosphatase (ALP) activity of osteoblast cells cultured on the nanotube surfaces. **(a)** ALP activity as a function of time. **(b)** Fluorescent images showing ALP staining after 21 days. **(c)** Semi-quantification of ALP staining representing how much cell surface area was covered by ALP activity based on microscopic fields (N=4). The bar graph shows the average ± the standard error. P values after performing t-tests reaching statistical significance $P<0.05$ are marked on the graphs.

The degree of osteogenic differentiation and maturation of the MSCs was analyzed via various assays after 3 weeks of culture. The ability of the MSCs to deposit mineralized matrix is one important indication of the bone functionality of the cells. Fluorescent images of alizarin red staining for calcium mineral deposition after 3 weeks of incubation are depicted in **Figure 4.1-3(a)**, and the percent area stained is shown in the graph in **Figure 4.1-3(b)**. The staining on the carbon-coated nanotube surface showed slightly larger areas of mineral deposits, as indicated by

the yellow arrows, however it was not a statistically significant difference. A slightly enhanced osteogenic function was confirmed by ALP activity measurements and quantitative PCR analysis for osteocalcin (OCN) and osteopontin (OPN). OCN and OPN are two major noncollagenous protein components of bone extracellular matrix that are considered markers of osteogenic differentiation as they are solely synthesized and secreted by osteoblastic cells. The graphs of relative amounts for each assay are shown in **Figure 4.1-4(a)** and **(b)**; the ALP activity and relative gene expression of OPN were significantly upregulated on the carbon surface chemistry when compared to the $TiO_2$ nanotube surface. The carbon surface chemistry appears to cause an increase in osteogenic differentiation and function of the MSCs. These results indicate that MSCs can distinguish between surface chemistries and crystallinity, as other research groups have also observed [113].

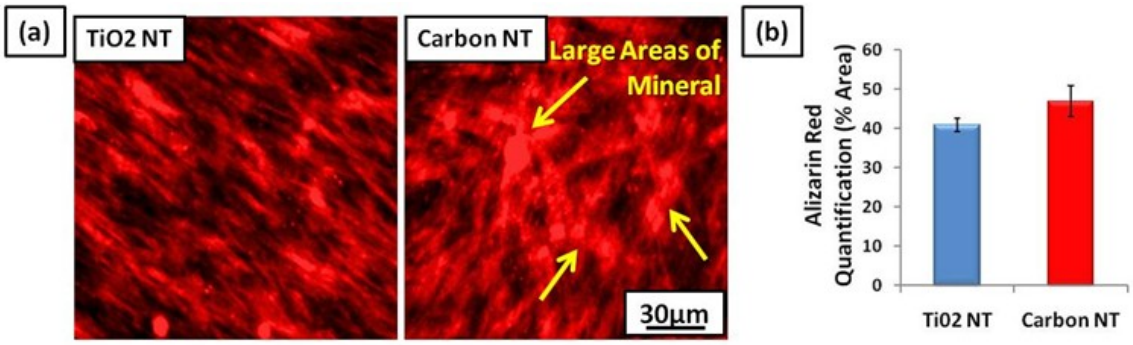


**Figure 4.1-3.** Alizarin red staining for mineral deposition of hMSCs cultured for 3 weeks.**(a)** Fluorescent images showing alizarin red staining (bright red) for the different experimental surfaces. **(b)** Semi-quantification of alizarin red representing how much surface area was covered by bone like mineral matrix based on microscopic fields (N=4). The bar graph shows the average ± the standard error.

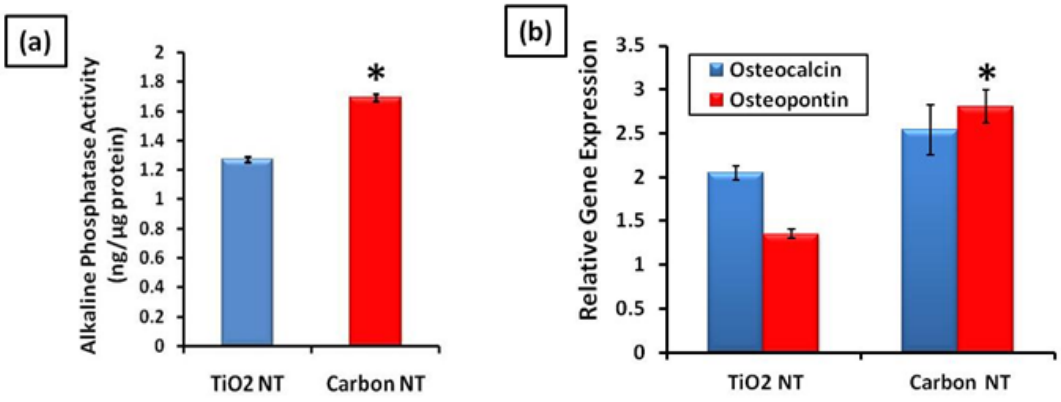


**Figure 4.1-4.** Degree of osteoblastic differentiation and maturation in late stage mesenchymal stem cell (MSC) culture (3 weeks). **(a)** ALP activity for MSCs cultured on the nanotube surfaces, $TiO_2$ vs. Carbon chemistry. **(b)** Quantitative PCR analysis for osteocalcin and osteopontin. The graph shows the average ± standard error bars. P values after performing t-tests reaching statistical significance $P<0.005$ are marked on the graphs.

The results of this study indicate that mesenchymal stem cells and osteoblast cells respond differently to remarkably different surface chemistries, and seem to have different chemical preferences most favorable for cell function. While osteoblast cells are mature bone cells specific to bone tissue, mesenchymal stem cells are highly sensitive, unprogrammed cell, and are readily influenced by extracellular factors such as chemical and topographical cues. Thus it is not surprising that the two cell types have different preferences of surface chemistry. The inclination of the MSCs to the C-coated surface may be explained by the fact that bone marrow contains many organic carbon-rich components. In contrast, bone tissue is composed of more ceramic/mineral rich components, similar to $TiO_2$.

The results of this study indicate that mesenchymal stem cells and osteoblast cells respond differently to remarkably different surface chemistries, and seem to have different chemical preferences for optimal cell function. While osteoblast cells are mature bone cells specific to bone tissue, mesenchymal stem cells are highly sensitive, unprogrammed cells, and are readily influenced by extracellular factors such as chemical and topographical cues. Therefore, it is not surprising that the two cell types have different preferences of surface chemistry. It is possible that the inclination of the MSCs for the C-coated surface may be explained by the fact that bone marrow contains many organic carbon-rich components. In contrast, bone tissue is composed of more ceramic/mineral rich components, similar to $TiO_2$. Perhaps the different cell types are partial to distinct chemistries because of the chemical components of their natural extracellular environments *in vivo*.

### 4.1.3 Conclusion

These findings give substantial evidence towards the importance of surface chemistry for directing cell fate, and indicate that systematic analysis is required of various bone implant material surface chemistries in conjunction with a nanotopography. Emphasis should be placed on the observation that different cell types have different preferences for

chemical/nanotopographical cues, and thus future work should consider this phenomena when organizing experiments.

## 4.2 Tantalum Coating on $TiO_2$ Nanotubes Induces Superior Rate of Matrix Mineralization and Osteofunctionality

Metallic tantalum (Ta) has been a biomaterial of more recent interest for orthopedic applications, as it has been found to be highly corrosion resistant and bioinert [114], as well as bioactive *in vivo*, forming a bone-like apatite layer in simulated body fluid that biologically bonds to bone [115]. Tantalum has regained interest in the biomaterials field mainly due to a new porous (trabecular) tantalum material of micro-porosity approved by the FDA in 1997, which has been shown to possess excellent osseointegrative properties [116]. Since then, studies have compared the biocompatibility, bacterial adherence [117] and osteoconductivity [118] of Ta with that of other common implant materials, such as Ti, CoCr, and hydroxyapatite coatings [119]. In particular, a clinical review was published in 2010 demonstrating that a higher degree of implant fixation was obtained in patients who received porous tantalum acetabular cups when compared to those with hydroxyapatite-coated titanium cups (industry gold standard) [120]. Additionally, a recent *in vitro* study by Sagomonyants, et al. demonstrated that porous Ta even stimulates the

proliferation and osteogenesis of osteoblasts from elderly female patients with compromised bone-forming abilities when compared with titanium fiber mesh [121]. However, despite the promising results to-date, the relatively expensive manufacturing cost, as well as the inability to produce a modular all-Ta implant has prevented its widespread acceptance [116]. A simple solution that has been suggested previously [119, 122] is to coat a Ti implant with a Ta film, thus incorporating the Ta surface chemistry while maintaining the mechanical advantages of a Ti implant (i.e. relatively low elastic modulus).

Few studies have been published to-date investigating nanostructured tantalum as a biomaterial [123-124]. One study in 2009 by Ruckh, *et al.* shows evidence that anodized tantala nanotubes provide a substrate for enhanced osseointegration when compared to flat Ta [123]. However, the study only compares the non-textured surface with the nanotextured surface of the same surface chemistry. Additionally, the nanotubes are of relatively great length (2-11 μm), which has been found in our laboratory to cause a tendency of the nanotube layer to delaminate easily. The relatively unstable nature of this structure is of great concern for an orthopedic implant surface.

Since our recent work in which we examined the effect of a carbon-coated $TiO_2$ nanotube surface on osteoblast and osteo-

progenitor cells [74], we have been interested in other surface chemistries which may enhance the osteofunctionality on the nanotube surface. In light of the promising findings regarding a Ta biomaterial of microtopography (~500-700 μm pore size), as well as the results of Ruckh, *et al.*, we chose to study the effects of the Ta surface chemistry in direct comparison with $TiO_2$ on the same nanotopography (i.e. vertically aligned, laterally spaced 100 nm diameter nanotubes), as well as flat surface controls. The work herein compares the response of human osteoblast cells to the bare $TiO_2$ nanotube surface to a Ta-coated nanotube surface in terms of osteofunctionality and bone-forming ability. The results reveal that the Ta surface chemistry on the nanotube architecture enhances alkaline phosphatase activity, and promotes a ~30% faster rate of matrix mineralization and bone-nodule formation when compared to results on bare $TiO_2$ nanotubes.

### 4.2.1 Experimental Methods

#### *Nanotube Substrate Fabrication*

$TiO_2$ nanotube surfaces were created using a two electrode set-up anodization process as described previously [125]. A 0.25 mm thick commercially pure Ti sheet (99.5 % metal basis, Alfa-Aesar, USA) was used for this process, which was first cleaned successively in acetone and isopropyl alcohol with ultrasonication followed by DI water rinse. The

nanotubes were prepared in a 1:7 volumetric ratio of acetic acid (≥99.99 % purity, Sigma-Aldrich, USA) to a weight percent fraction of 0.5 % hydrofluoric acid in water (48 % w/v, EM Science, USA) at 20 V for 30 min. A platinum electrode (99.9 %, Alfa-Aesar, USA) served as the cathode. The samples were then washed with deionized water, dried at 80° C, and heat treated at 500 °C for 2 h in order to crystallize the as-fabricated amorphous structured $TiO_2$ nanotubes to anatase structure. Tantalum films (20 nm-thick) were vacuum-deposited onto $TiO_2$ nanotube and flat Ti control substrates from a tantalum target in a Denton Discovery 18 sputter system. To ensure preferential coating of the $TiO_2$ nanotube surface, the deposition angle used was ~30° off the vertical axis with substrate rotation during deposition. 200 W plasma was applied when Ar pressure reached 3 mTorr after base pressure reached $10^{-6}$ torr. The as-deposited Ta film is expected to be of amorphous nature.

***Contact Angle Measurement***

The measurement of contact angle for each experimental flat and nanotube surfaces was carried out using a video contact angle measurement system model VSA 2500 XE (AST Products Inc.). A small deionized water droplet (~3 mg) was placed on the nanotube surface to measure the static contact angle. Measurement of the contact angle is a simple method for analyzing the surface energy and hydrophilic nature of

a surface. In this case we also wanted to verify that the tantalum (more hydrophilic in nature compared with $TiO_2$) had been deposited and to observe the changes in surface energy after deposition.

***Osteoblast Cell Culture***

For these studies, human osteoblast (HOb) cells isolated from normal adult human bone (406-05a, Cell Applications, Inc., USA) were used. Each 1 ml of cryo-conserved stock was mixed with 10 ml of alpha minimum essential medium (αMEM; Invitrogen, USA) in the presence of a volume fraction of 10 % fetal bovine serum (FBS; Invitrogen, USA) and a volume fraction of 1 % penicillin-streptomycin (PS; Invitrogen, USA). The cell suspension was plated in a polystyrene cell culture dish and incubated at 37° C in a volume fraction of 5 % $CO_2$ environment. Each 1.27 × 1.27 $cm^2$ experimental substrate ($TiO_2$ nanotubes, Ta-coated nanotubes, and flat control Ti and Ta) was placed into individual wells of a 12-well polystyrene plate. The polystyrene (PS) culture dish was used as a control. When the cells reached confluency, the HOb osteoblast cells were seeded at a concentration of $2.5\times10^4$ cells per well onto the experimental substrates and stored in a $CO_2$ incubator for the experimental time durations. For experimental time points beyond 7 d of culture, cell media was changed at 7 d to osteogenic induced media, αMEM containing a volume fraction of 10 % FBS, a volume fraction of 1 %

PS, 10 nmol/L dexamethasone (Sigma, USA), 150 µg/ml ascorbic acid (Sigma, USA) and 10 mmol/L β-glycerol phosphate (Sigma, USA). All experimental substrates were moved to a new 12-well dish before cell assays were performed in order to isolate the cells on the substrate of interest from cells on the surrounding polystyrene dish.

***MTT Assay***

To estimate the metabolic activity of the cells, an MTT (3-(4,5-dimethylthiazole-2-yl)-2,5-diphenyl tetrazolium bromide) assay was employed. After the selected incubation periods, the samples were washed by PBS and transferred to a new 12-well polystyrene culture plate. Fresh cell culture media was added to each well, and the MTT dye agent was added in an amount equal to 10 % of the culture media volume, according to manufacturer's instructions (MTT kit, Sigma, USA). After 2 h of incubation in a 5 % $CO_2$ incubator, 1 ml of solubilizing solution was added to each well and the polystyrene plate was shaken for 30 sec to dissolve the formazan crystals. The fluorescent absorbance of each solution was measured at a wavelength of 570 nm with the subtraction of the 650 nm background by ultraviolet-visible (UV-vis) spectrophotometer (Biomate™ 3, Thermo Electron Co., USA).

***Scanning Electron Microscopy (SEM) for Cell and Substrate Examination***

After 24 h and 21 d of culture, the cells on the substrates were washed with PBS and fixed with a mass fraction of 2.5 % glutaraldehyde (Sigma, USA) in PBS for 1 h. After fixation, they were washed three times with PBS for 15 min each wash. The cells were then dehydrated in a graded series of ethanol (volume fractions of 50, 75, 90 and 100 %) for 30 min each and left in 100 % ethanol to be dried by a critical point dryer (EMS 850, Electron Microscopy Science Co., USA). Next, the dried samples were sputter-coated with palladium metallization for examination by scanning electron microscopy (SEM). The morphology of the samples as well as that of the adhered cells was observed using a Phillips XL30 field emission environmental scanning electron microscope (FEI Co., USA).

***Energy Dispersive X-Ray Analysis***

The presence of the tantalum thin film coating on the flat Ti and $TiO_2$ nanotube surfaces was confirmed via energy dispersive X-ray analysis (EDX). The Oxford EDX attachment and Inca Software were used to determine elemental composition of the surface. In addition, matrix mineralization was analyzed by EDX analysis after 7, 14, and 21 d of culture. After the experimental culture time was complete, the cells were trypsinized by trypsin EDTA 0.25 % (Invitrogen, USA) and allowed to air dry for SEM and EDX analysis. Identical samples were incubated in cell-free

media as a control. In these studies, EDX was used to determine the elemental composition of deposited bone matrix. The reported atomic percent values were normalized by the relative amounts of Ca and P present on the surfaces incubated under identical conditions in cell-free media.

***Immunofluorescence of Cytoskeletal Actin***

After 24 h of culture, the cells were fixed in 4 % paraformaldehyde in PBS for 15 min at room temperature. Once fixed, the cells were washed twice with wash buffer (PBS containing a volume fraction of 0.05 %Tween-20). To permeabilize the cells, 0.1 % Triton X-100 in PBS was added for 10 min, followed by washing twice with wash buffer. TRITC-conjugated phalloidin (1:1000 Chemicom International) in PBS was added and incubated for 1 h at room temperature, after which the cells were washed three times with wash buffer for 5 min each wash. Samples were then inverted onto coverslips with a dab of Fluoromount-G (Electron Microscopy Sciences, USA), visualized and photographed using a Rhodamine (536 nm excitation) filter by a fluorescence Leica, Co. DM IRB microscope.

***Alkaline Phosphatase Activity Test***

In order to measure the bone forming ability of cells on the experimental surfaces, the alkaline phosphatase (ALP) activity was

detected using a colorimetric assay kit. Briefly, after the selected incubation periods, the samples were washed by PBS and transferred to a new 12-well polystyrene culture plate. Cells were then gently washed twice with phosphate buffer provided by the kit supplier, followed by the addition of a volume fraction of 0.2 % Triton X-100 in phosphate buffer. The adherent cells were further scraped off of the sample substrate and collected in a microcentrifuge tube. Cell suspension was incubated on ice for 10 min under agitation, and then centrifuged at 2500 ×g for 10 min at 4°C. The supernatants were stored at -60°C until further analysis by AnaSpec SensoLyte pNPP Alkaline Phosphatase Assay Kit colorimetric assay (AnaSpec, Inc., USA) following the manufacturer's instructions. The ALP values were normalized by protein content obtained by a BCA kit (Sigma, USA).

***Alizarin Red S Staining***

Alizarin red staining was employed to detect osteoblast mineralization (calcium deposits). After 7, 14, and 21 d of culture, the cells were fixed for 20 min with 4 % paraformaldehyde (Sigma, USA) and stained overnight at 4 °C with a mass fraction of 2 % alizarin red S (Sigma, USA) in distilled water, and the pH was adjusted to 4.1—4.3 using a volume fraction of 10 % ammonium hydroxide. The samples were then washed with distilled water with gentle rocking three times for 10 min each. The

samples were visualized using a Leica DM IRB fluorescence microscope. In order to quantify the alizarin red area on the experimental surface, the microscope fields were analyzed using Image J software.

***Statistical Analysis and Error Bars on Graphs***

Sigma Plot 11.0 software (2008) was utilized to demonstrate the statistical significance of the assays. The graphs show the average ± standard error bars associated, with *p*-values listed in the figure captions.

### 4.2.2 Results and Discussion

Anodized $TiO_2$ nanotube surfaces reportedly offer several advantages over unmodified Ti surfaces for orthopedic implant applications, in terms of significantly enhanced bone mineral formation [2] and adhesion of osteoblasts *in vitro* [125], preferential differentiation of osteo-progenitor cells into osteoblast-like cells *in vitro* [3], and strongly adherent bone growth *in vivo* [126]. Although the phenomenon is not completely understood, the research community continues to investigate whether the enhanced osteoblast and osteo-progenitor cell response is due to the nanotopography/nano-feature size [2-3, 73], surface chemistry [74], or wettability/surface energy [127]. Considering the recent interest in tantalum as an orthopedic biomaterial, and findings which have shown an improved bone cell response to porous Ta when compared to porous Ti [128] and tantala nanotubes when compared to flat Ta [123], we were

attracted to investigate the effect of tantalum-coated $TiO_2$ nanotubes on osteoblast cell behavior.

**Figure 4.2-1** presents SEM images of the flat Ti, flat Ta, and both as-made $TiO_2$ nanotube and Ta-coated nanotube surfaces. The nanotube images reveal near identical structures, with an outer diameter of ~100 nm, ~10 nm wall thickness, ~10 nm spacing, and ~300 nm height, as previously described [2, 125]. The Ta coating performed by vacuum sputter deposition allows for deposition of a conformal layer with high control of the Ta thickness (20 nm). Ta is reported to be a biocompatible material, its corrosion resistance equivalent to Ti, and both Ta and Ta oxide possess low solubility and toxicity [129]. Titanium and tantalum are similar in that they both form a natural oxide layer when exposed to air, which has been attributed to the excellent biocompatibility of these materials [130-131]. It is thus assumed that the amorphous Ta coatings in this study possess a thin natural oxide layer, and are not entirely metallic. The water contact angles are displayed in yellow in the upper right corner of the SEM images in **Figure 4.2-1**, demonstrating that the flat Ta surface is more hydrophilic in nature than the flat Ti surface (31° and 54°, respectively). In addition, the Ta coating induced a slight increase in hydrophilicity from ~4° to ~0° on the $TiO_2$ and Ta coated nanotube surfaces, respectively.

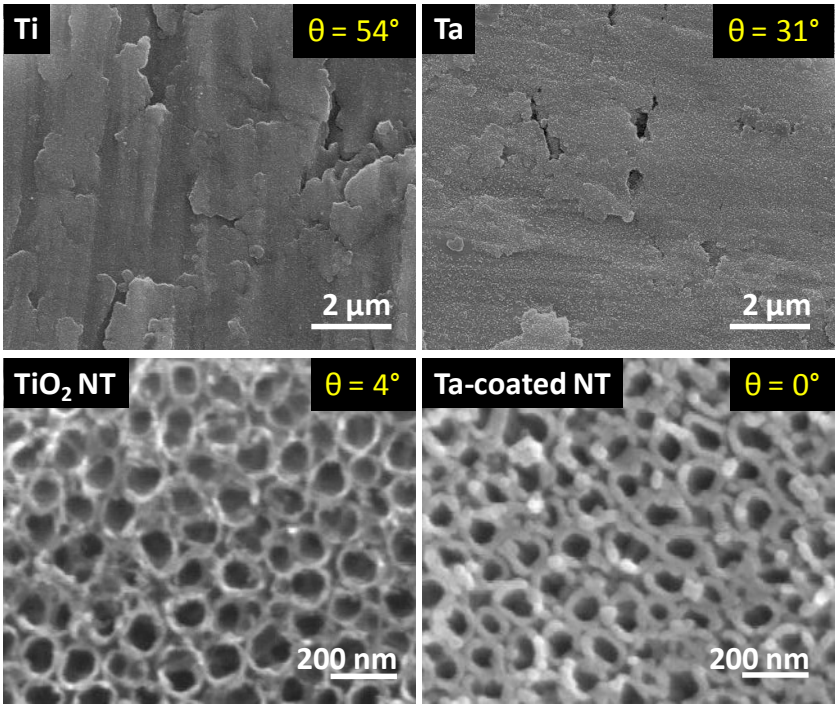


**Figure 4.2-1.** SEM images of the flat Ti, flat Ta, $TiO_2$ nanotube (NT), and Ta-coated nanotube (NT) substrates. The images depict preservation of the nanotube geometry and structure after tantalum coating. The contact angle for each surface is shown in yellow, indicating an increase in hydrophilicity on both tantalum-coated surfaces: from 54° to 31° (flat), and 4° to 0° (nanotube).

The presence of the Ta coating was confirmed via energy dispersive X-ray analysis (EDX), which shows the presence of peaks corresponding to Ta as shown in **Figure 4.2-2**. In addition, the Ta coating resulted in a redish metallic color on the nanotube substrates (in contrast to a greenish/blue color on the as-made nanotube samples). The flat Ta sample showed similar evidence of the Ta coating with EDX analysis and a slight color change to yellow/gold (in contrast to silver metallic color of the as-received Ti foil).

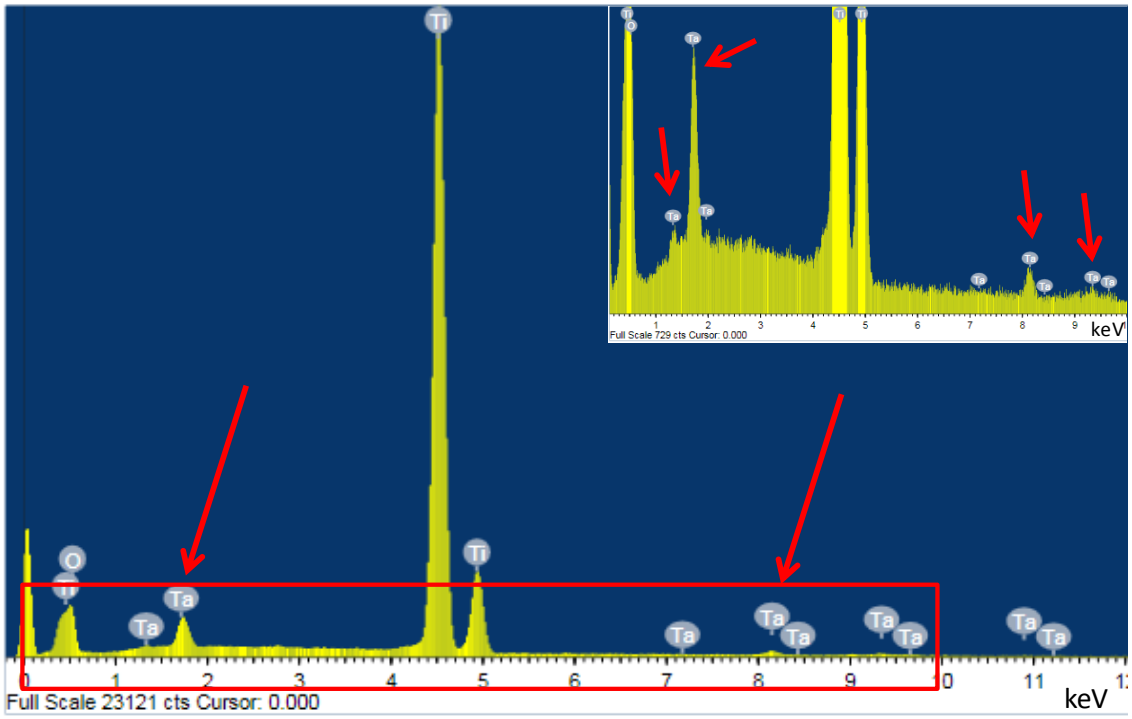


**Figure 4.2-2.** EDX spectrum illustrating the presence of Ta (red arrows) on the surface of the $TiO_2$ nanotube surface. The area highlighted by the red box is enlarged in the inset.

An MTT assay was utilized in order to measure the metabolic activity of the cells and to indirectly estimate the number of adhered, viable cells. Results of the MTT analysis in **Figure 4.2-3(a)** reveal a trend of increasing cell viability until day 14, at which the proliferation begins to decrease. This trend is consistent with published literature, which contributes a peak in osteoblast proliferation (usually at around 12-14 days) as the end of the proliferative period, and the beginning of the matrix maturation phase [132-133]. The MTT data shows no significant difference between the flat control samples and the $TiO_2$ and Ta-coated nanotube surfaces. This trend is rather unexpected, since prior findings in our laboratory have

shown significant acceleration of MC3T3-E1 osteoblast cell growth on $TiO_2$ nanotube surfaces when compared to flat Ti controls [125]. However, the differing results observed in this study could be due to the use of primary osteoblast cells isolated from normal human bone in contrast to the highly proliferative murine cell line used in prior studies. The literature also contains contrasting trends of cell adhesion and proliferation on nanostructured surfaces, which seem to vary based on differing cell type, species, source and maturation [134-135]. Moreover, many of such experiments are performed using very robust and proliferative cell lines, which may bias the findings [134].

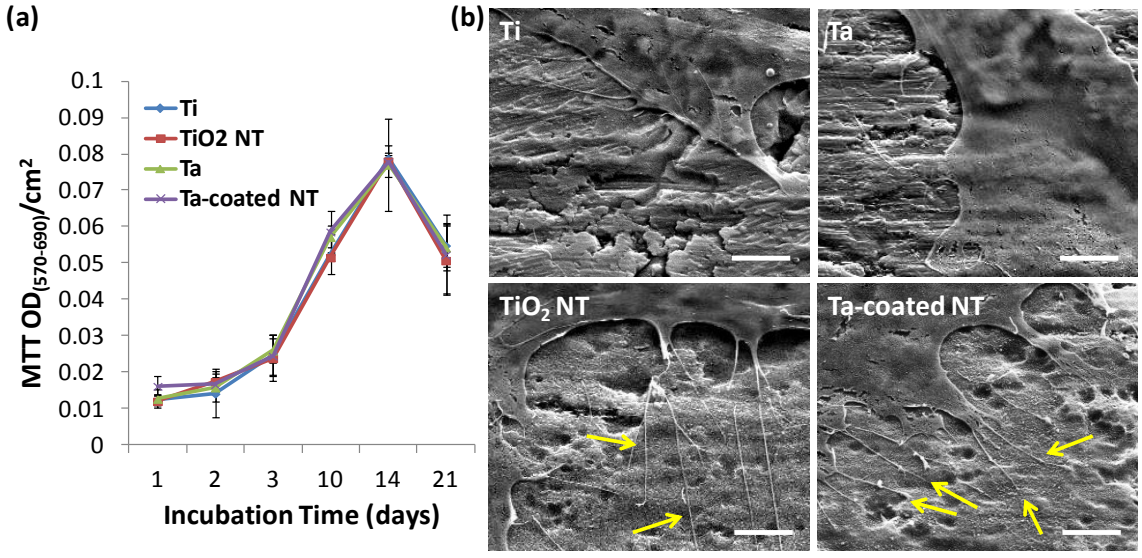


**Figure 4.2-3. (a)** MTT assay data showing the optical density (OD) of the reaction product of the MTT working solution of HOb cells cultured on the nanotube surfaces as a function of incubation time ($n$ = 3). The line graph shows the mean ± standard error bars. **(b)** SEM micrographs of HOb cells after 24 h incubation, showing extensive filopodia activity on both nanosurfaces (yellow arrows). Scale bars = 5 µm.

SEM morphological examination shown in **Figure 4.2-3(b)** after 24 h of culture reveals extensive filopodial activity on both $TiO_2$ and Ta surfaces, but not on the flat control surfaces (as indicated by the yellow arrows). A common speculation is that finger-like filopodia are a cell-sensing mechanism which are used to detect both chemical and nanotopographical cues [41]. An increase in filopodial activity has been demonstrated previously on both $TiO_2$ [2] and $ZrO_2$ [136] nanotube architectures when compared to respective flat controls surfaces. The presence of many filopodia on both nanotube surfaces indicates that the HOb cells are relatively equally activated by the nanotube architecture, independent of surface chemistry.

In addition, cytoskeletal actin organization and cell morphology was also unaffected, as depicted in **Figure 4.2-4**. The figure shows immunofluorescent staining of the cytoskeletal actin of HObs after 24 h of culture on the flat surfaces and both $TiO_2$ and Ta nanotube substrates. It is apparent that the cells on the nanotube surfaces possess a criss-cross pattern within the cell body, as signified by the yellow arrows. The unique cytoskeletal arrangement observed on the nanotube substrates is likely to be a result of an altered placement of proteins adsorbed onto the nanotopographical features from the culture media [2], as well as extracellular protein such as fibronectin and vitronectin [11].

Nanotopography has also been shown to cause distinctive integrin and focal adhesion plaque placement on the surfaces [137], which in turn affects cytoskeletal arrangement [138]. The actin organization by visual comparison appears to be minimally effected by the two surface chemistries compared in this work. These results are perhaps in agreement with prior results which showed no significant difference between proliferation, attachment, or cytoskeletal arrangement between human osteoblast cells cultured on Ta and Ti substrates [118]

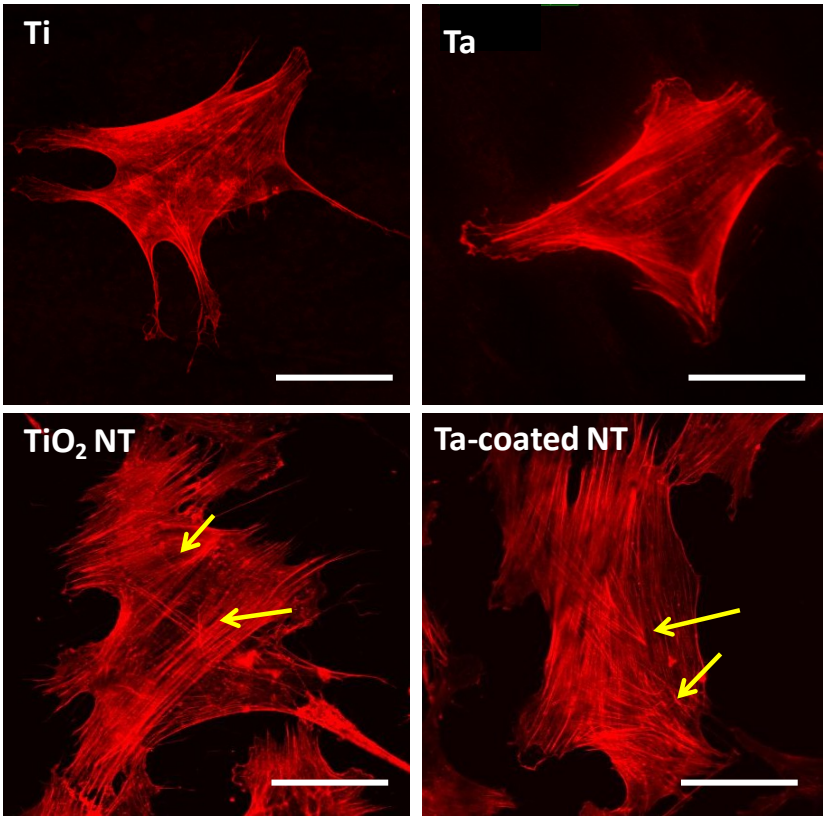


**Figure 4.2-4.** Immunofluorescent images of cytoskeletal actin (red) of HOb cells on flat and nanotube surfaces after 24 h of culture incubation, showing a criss-cross pattern on both $TiO_2$ and Ta surfaces (yellow arrows). Scale bars = 50 µm.

Alkaline phosphatase (ALP) activity was measured as a function of incubation time to estimate the bone-forming ability of osteoblast cells on the experimental substrates (**Figure 4.2-5**). As mentioned earlier, the peak in cell growth at day 14 (**Figure 4.2-3**) is consistent with the progressive development of osteoblasts demonstrated in the literature, which indicates the end of the proliferation stage, and the onset of extracellular matrix maturation. In concurrence with a decrease in cell proliferation, an up-regulation in ALP activity in osteoblasts occurs during the matrix maturation phase [132-133]. This reciprocal relationship is evident in comparing **Figure 4.2-3** and **Figure 4.2-5**: the onset of increasing ALP activity (at ~day 10-14) with decreasing cell proliferation (at day 14) indicates proper osteoblast matrix maturation [133]. It is also apparent that the ALP activity is increased on both nanotube surfaces when compared to their respective flat surfaces ($Ti/TiO_2$ NT, and Ta/Ta-NT). This observation is expected, since prior studies have demonstrated enhanced bone function on nanotube architectures when compared to flat controls for $TiO_2$ [2], $ZrO_2$ [136], and $Ta_2O_5$ [123].

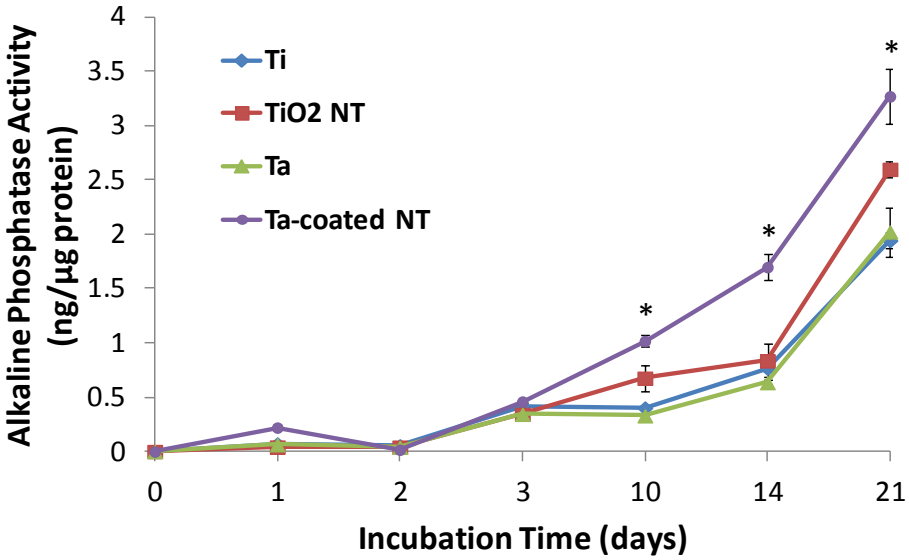


**Figure 4.2-5.** ALP activity of HOb cells cultured on the nanotube surfaces vs. incubation time ($n$ = 3). The graph points show the mean ± standard error bars. The $p$-values after performing an ANOVA test reaching statistical significance ($p < 0.001$) are marked on the graph (*).

However, when comparing the two nanotube surfaces in this study, it is interesting to note that no difference was observed at shorter time points; conversely at 10 days and beyond, a significantly higher ALP activity was detected on the Ta-coated nanotube surfaces when compared to all of the other samples. Since the nanotube surfaces are of identical topography, but with differing surface chemistry, one could speculate that the Ta chemistry may enhance the osteogenic functionality of the HOb cells on the nanotube surface. However, the ALP levels of the flat Ta compared to the flat Ti do not clearly support this claim (flat Ta is lower than Ti at day 3, 10, and 14, although the difference is not statistically significant). Additionally, the literature comparing *in vitro*

osteogenic behavior on Ti and Ta surfaces is not entirely consistent. While an increased ALP activity on flat Ta thin film when compared to flat Ta thin film was observed by Stiehler, et al. [129], multiple other studies have demonstrated that the osteogenic behavior on Ta and Ti are relatively the same [118, 139]. The fact that we only saw a significant upregulation on the nanostructured tantalum surface could indicate that there is a unique combination of physico-chemical properties on this surface that is not present on the others. For example, while the $TiO_2$ nanotube surface is hydrophilic (contact angle of 4°), the Ta-coated nanotube surface is superhydrophilic, with a contact angle of 0°. This is in great contrast to the flat Ti and Ta rather hydrophobic contact angles (54° and 31°). Furthermore, it is known that surface hydrophilicity is directly related to the energy at the surface of a biomaterial, which is defined by the general charge density and net polarity of the charge [113].

In understanding the relative charge of a surface, a discussion of isoelectric points is necessary. It is well known that the surface of a metal oxide film terminates in an outermost layer of hydroxyl groups [140]. In an aqueous solution with a pH equal to the isoelectric point, the surface hydroxyl groups will remain undissociated [140]. Although the isoelectric points of metal oxides vary based on factors such as temperature and crystal structure as well as method of measurement [141], the estimated

isoelectric point of anatase phase titanium oxide (6.1 [142]) is much higher than that of tantalum oxide (2.7-3.0 [140]). However, the optimal pH for human osteoblast cell culture in vitro is ~7.2 [143] (most culture media have pH=7.4). Since the pH of the culture media (7.4) is greater than the isoelectric point of both $TiO_2$ (6.1) and $Ta_2O_5$ (2.7-3.0), the surface will acquire a negative charge by either of the following reactions [140]:

$$–MOH_{surf} + OH^- \leftrightarrows –MO_{surf}^- + H_2O \quad (1)$$

or

$$–MOH_{surf} \leftrightarrows –MO_{surf}^- + H_{(aq)}^+. \quad (2)$$

However, for a lower isoelectric point, more negative charges will accumulate on the surface [144]. This means that it is probable that the Ta-coated surfaces are more negatively charged than the $TiO_2$ surfaces, leading towards greater affinity of positively charged ions and molecules to accumulate on the surface (i.e. $Ca^{2+}$, $Mg^{2+}$, $Na^+$, which are present in cell culture media). The presence of such ions on a surface has been shown to increase osteoblast function *in vitro* [145-147], as well as enables the surface to bind electrostatically to a variety of proteins [148]. Furthermore, a study by Moller, et al. revealed that a higher degree of osteoblast differentiation was achieved on a biocomposite with the lowest isoelectric point [149].

Another factor that may affect the relative charge of the surfaces is that the $TiO_2$ nanotubes were heat treated in order to transform the as-made amorphous structure to anatase (for osteoblast preference [125]). Heat treatment has been shown to diminish the amount of OH groups on a surface [150], and is likely to affect the overall surface charge. In contrast, the Ta-coated nanotube surface was heat treated, then deposited with a thin layer of Ta, which spontaneously forms hydroxyl groups on the surface. Lastly, the nanostructured surface presents a much larger surface area than a flat surface. The larger surface area would introduce more active sites and active OH groups on the nanotube surfaces than on the corresponding flat substrates [150]. As a result, the combination of the nanostructure and more negatively charged Ta surface coating of the Ta-coated nanotube surface may be more highly active for ion and biomolecule accumulation on the surface, thus enhancing the osteoblast cells ability to form mature extracellular matrix (which has been linked to upregulation in ALP activity [133]). The interplay between these physico-chemical differences and osteoblast behavior is not well-understood, and their possible effects in this study are only speculation. However, the Ta-coated nanotube surface demonstrates a significantly higher ALP activity than the $TiO_2$ nanotube surface as well as

flat controls, which may signify a greater extent of matrix maturation at this stage [133].

The third phase of osteoblast development is the onset of matrix mineralization, which is essential for expression of osteoblast phenotypical genes [132]. In order to evaluate the degree of matrix mineralization of the bone cells on each experimental surface, the osteoblasts were analyzed for bone nodule formation via various analytical techniques. After 21 d of culture, the osteoblast morphology on the nanotube surfaces was assessed by SEM, which revealed the presence of large bone nodules [151] on both nanotube surfaces, with very little nodule-like formation on the flat controls (**Figure 4.2-6(a)**). The presence of bone nodules was also visible on the positive control tissue culture plastic (data not shown). In addition, energy dispersive x-ray (EDX) analysis revealed significantly higher amounts of both phosphorus and calcium on the Ta-coated nanotube samples than was found on all other samples, as shown in the graph in **Figure 4.2-6(b)**. This indicates that although bone nodule formation readily occurred on both nanotube surfaces, the Ta-coating appears to have had the effect of inducing increased deposition of bone matrix minerals. The formation of bone-like apatite on tantalum metal in simulated body fluid has been previously reported [147], as well as on Ta treated with sodium hydroxide (NaOH) [152]. Furthermore, a prior study by

Oh, et al. demonstrated the formation of nano-scale hydroxyapaptite on the surface of $TiO_2$ nanotubes after treatment with NaOH [153]. It would be interesting to compare the apatite-formation behavior of the $TiO_2$ and Ta-coated nanotube array in simulated body fluid. Osteoblast cells have been shown to preferentially differentiate to form mineralized extracellular matrix on apatite layers [152]. The speculation that a Ta nanostructure has apatite-inducing properties supports the hypothesis that it also encourages the production of mineralized matrix by HOb cells.

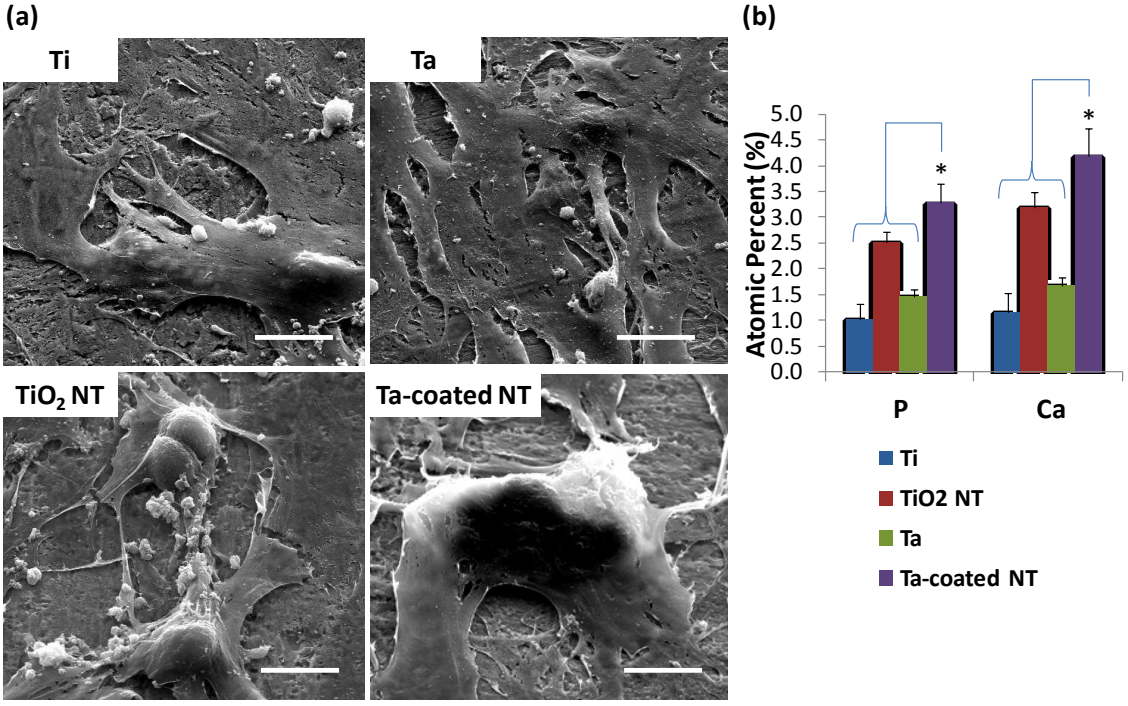


**Figure 4.2-6.** Bone nodule formation by HOb cells cultured for 3 weeks. **(a)** SEM micrographs at 1000x showing larger bone nodule formation on the Ta-coated NT surface. Scale bar = 20 μm. **(b)** EDX analysis of the atomic percent of calcium and phosphorous mineral elements on the surfaces ($n$ = 5). The bar graph shows the mean ± standard error bars. The $p$-values after performing an ANOVA test reached statistical significance ($p \leq 0.001$), as indicated by (*).

The kinetics of matrix mineralization were also examined in order to determine whether the rate of mineralization was effected by the nanostructure or surface chemistry. EDX analysis estimating the atomic percent of phosphorus (**Figure 4.2-7 (a)**) and calcium (**Figure 4.2-7 (b)**) on each substrate after 7, 14, and 21 d of culture revealed that the highest rate of mineralization occurred on the Ta-coated nanotube surface. A linear trendline was estimated for the mineral atomic percent as a function of incubation time for each sample type using Microsoft Excel, and the slope of each line was determined and recorded as the rate of phosphorus or calcium deposition (**Figure 4.2-7 (c)**). The correlation coefficients ($R^2$) of each trendline are portrayed on the graphs, demonstrating that this method only gives a rough estimate of the rates of mineralization. However, the rates of both phosphorus and calcium deposition are estimated to be roughly 30% faster on the Ta-coated nanotube substrate than on the $TiO_2$ nanotube substrate.

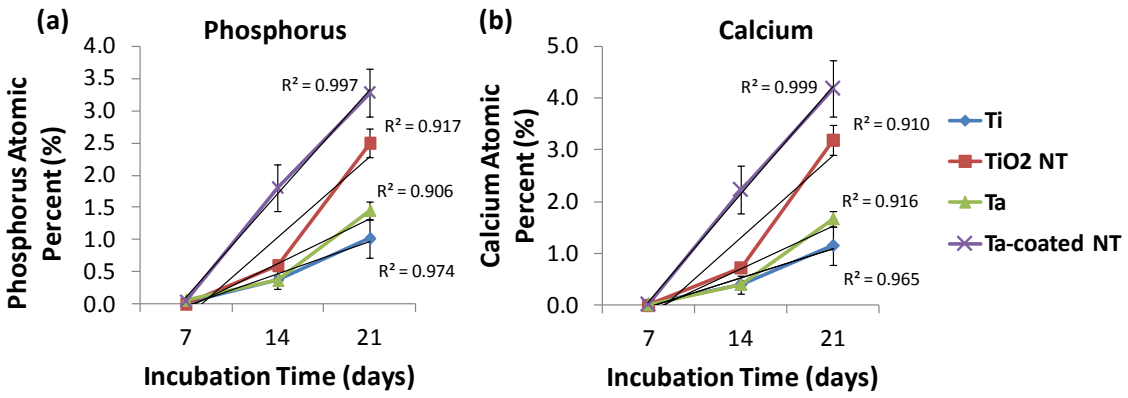


(c)

| Sample | Rate of P | Rate of Ca |
|---|---|---|
| Ti | 0.498 | 0.565 |
| Ta | 0.695 | 0.830 |
| $TiO_2$ NT | 1.247 | 1.594 |
| Ta-coated NT | 1.616 | 2.081 |

30% increase

**Figure 4.2-7.** Mineralization kinetics study. EDX analysis of the atomic percent of phosphorus **(a)**, and calcium **(b)** mineral elements on the surfaces as a function of time ($n$ = 5), with linear trendlines overlaid and correlation coefficients labeled. **(c)** A table of the corresponding rates (slopes of the linear trendlines) of phosphorus and calcium deposition for each substrate. The line graphs show the mean ± standard error bars. The $p$-values after performing an ANOVA test reached statistical significance ($p \leq 0.001$) for all comparisons between samples except for Ti vs. Ta.

The results of matrix mineralization kinetics were verified by alizarin red S staining, a simple and convenient method for detecting calcium mineral deposition. The immunofluorescent images show the stained area (bright red) on each experimental surface after 1, 2, and 3 weeks of culture in **Figure 4.2-8** (from left to right). After 1 week, only small amounts of mineral were detected on the $TiO_2$ and Ta-coated nanotube surfaces, while nothing was visible on the flat substrates. After 2 weeks, more highly concentrated areas of calcium mineral deposits (indicated by arrows) were visible on the nanotube surfaces, with a few on the flat surfaces.

After 3 weeks, large areas of several bone nodules were present on the nanotube surfaces; the nodules on the flat surfaces were fewer and less pronounced. The fluorescent staining was semi-quantified using ImageJ analysis in order to validate the relative surface areas covered in bone-like mineral shown in **Figure 4.2-8**. This data is presented in **Figure 4.2-9**, and reveals a higher stained surface area on the Ta-coated nanotubes than all other surfaces. These results verify the observations by EDX analysis. In addition, increased alizarin red staining was reported by Stiehler, et al. of MSCs on Ta when compared to Ti, which supports our findings [129].

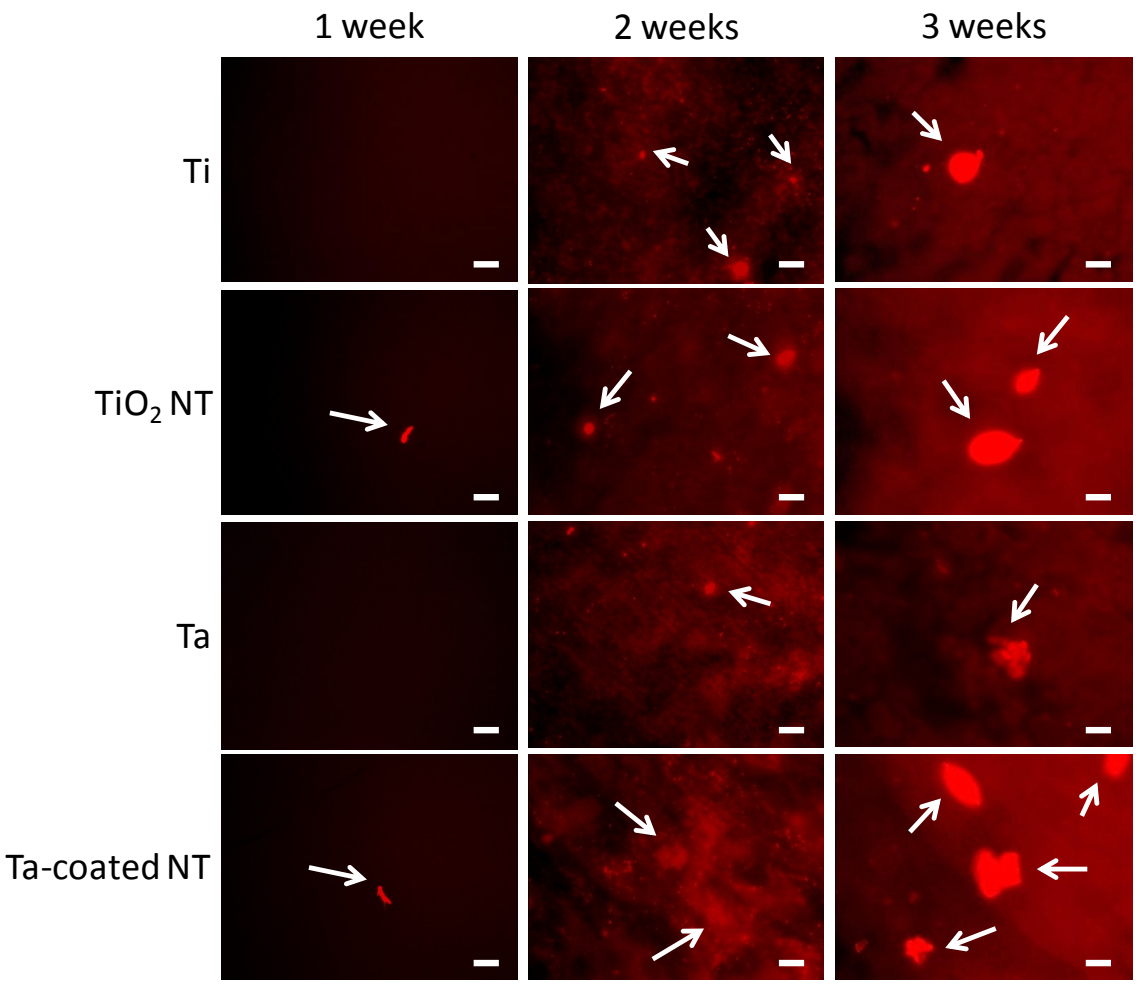


**Figure 4.2-8.** Alizarin red staining for mineral deposition by HObs cultured for 1, 2, and 3 weeks. Fluorescent images show alizarin red staining (bright red) for mineral deposition. Arrows indicate bone nodule formation. Scale bar = 50 μm.

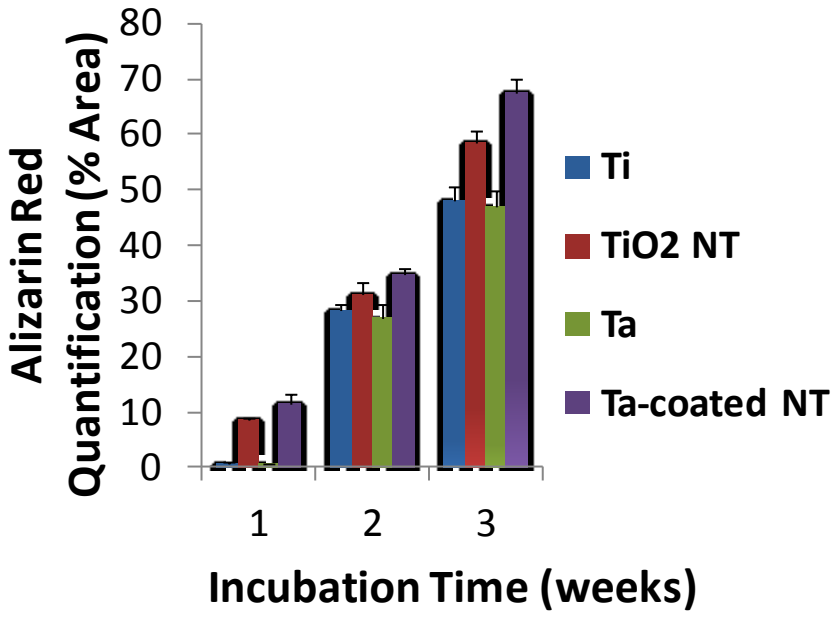


**Figure 4.2-9.** Semi-quantification of alizarin red in **Figure 4.2-8** representing how much surface area was covered by bone-like mineral matrix based on microscopic fields (n=5). The bar graph shows the average ± standard error.

Both the $TiO_2$ and Ta-coated nanotube surfaces enhanced osteogenic function over that of flat controls of smooth Ti and Ta-coated smooth Ti. However, the Ta-coated nanotube surfaces had superior osteofunctionality in terms of ALP activity, bone nodule formation, and the rate of matrix mineralization. These results indicate that HOb filopodial activity and cytoskeletal arrangement may be influenced primarily by nanotopographical cues (they were similar on both nanotube surfaces, but different on the flat surfaces). However, the osteogenesis may be more highly influenced by surface chemistry/material properties than nanotopography. This hypothesis coincides with our prior findings on carbon-coated nanotube surfaces [74]. Furthermore, some studies have

shown that osteoblast differentiation *in vitro* is more highly influenced by differences in surface chemistry irrespective of surface microtopography [154-155]. Another experiment by Cyster, et al. demonstrated that fibroblasts preferentially attached to titanium nitride surfaces of a defined surface chemistry at early time points; however at later time points, preference was shown towards a nanostructured surface, with no preference for surface chemistry [156]. While the interplay of the surface chemistry and nanotopography are not completely understood, it is apparent that unique combinations can have substantial results, and that cell preference for certain properties may change over time.

The purpose of this study was to evaluate the osteoblast response to Ta versus $TiO_2$ nanotube surface chemistries in terms of bone-forming ability. Our results indicate that nanotopographical Ta triggers enhanced osteofunctionality and matrix mineralization in adult human osteoblast cells, and even increased the rate of mineralization by ~30 % when compared to the bare $TiO_2$ nanotubes. We believe that a unique combination of surface chemistry and nanostructured geometry may provide a balance of defined characteristics towards an optimal orthopedic implant, and this study indicates that osteoblasts may prefer nanostructured Ta to nanostructured $TiO_2$ *in vitro*. An explanation for the observed behavior is not straightforward due to lack of studies comparing

nanostructured Ti and Ta surface behavior in vitro. Further studies are required to gain insight to this phenomenon, such as comparative analysis of protein adsorption, hydroxyapatite formation, and biomolecule interaction with the $TiO_2$ and Ta-coated nanotube surfaces. Future studies should also compare an amorphous Ta coating with that of crystalline Ta on the nanotube surface, since differences have been observed in osteoblast response to amorphous and crystalline $TiO_2$ nanotubes [125]. Additionally, it has been found that oxide layer thickness can affect protein adsorption on tantalum [157]. Hence it would be of interest to assess the effects of Ta surface oxide content (i.e. natural oxide layer versus a fully oxidized Ta layer) on osteogenic function. Lastly, it has been demonstrated that different cell types (i.e. osteoblasts versus osteoprogenitor cells) have different preferences for surface chemistry (Section 4.1), thus forthcoming research should compare the response of different cell types on varied surface chemical/nanotopography combinations.

The work presented herein demonstrates the highly sensitive nature of osteoblast cells to seemingly minute and simple modifications to a surface. With increased focus in the field of orthopedic materials research on nanostructured surfaces, this study emphasizes the need for careful

and systematic review of variations in surface chemistry in concurrence with nanotopographical changes.

### 4.2.3 Conclusion

Herein we have compared the behavior of human osteoblast cells on $TiO_2$ and Ta-coated nanotube surfaces of nearly identical nanotopography (and the respective flat controls surfaces), in order to assess the effect of changes in surface characteristics due to a Ta coating alone. It was determined that both nanotube surfaces instigate similar levels of cell adhesion, proliferation, and morphology. However, at advanced culture times, the osteofunctionality was enhanced on the Ta surface in terms of alkaline phosphatase activity, bone nodule formation, and matrix mineral deposition. In fact, the Ta surface promoted a ~30% faster rate of matrix mineralization and bone-nodule formation when compared to results on bare $TiO_2$ nanotubes. These findings are of paramount importance to the orthopedics field for understanding cell behavior in response to subtle alterations in nanostructure and surface chemistry, and will enable further insight into the complex manipulation of biomaterial surfaces. The enhanced HOb response observed on the Ta-coated nanotube surface is speculated to be a result of a unique combination of preferred nanotopography and surface chemistry.

## 4.3 Direct Comparison of Ta and Ta-Oxide Coated Anodic Nanotubes in Terms of *In Vitro* Human Osteoblast Function

Section 4.2 revealed that the Ta surface chemistry on the nanotube architecture enhanced alkaline phosphatase activity, and promoted a ~30% faster rate of matrix mineralization and bone-nodule formation when compared to results on bare $TiO_2$ nanotubes. However, as mentioned previously, further investigations are necessary in order to validate these findings, as well as provide greater insight into the effects of the tantalum chemistry. In particular, it has been found that oxide layer thickness can affect protein adsorption on tantalum [157]. As described previously (Section 1.3.2), protein interaction at the biomaterial surface is of great import and highly influential to cell behavior. Hence it would be of interest to assess the effects of Ta surface oxide content (i.e. natural oxide layer versus a fully oxidized Ta layer) on osteogenic function. The work herein compares the response of human osteoblast cells to the regular $TiO_2$ nanotube surface, as-deposited amorphous metallic Ta-coated nanotubes, and as-deposited amorphous tantalum oxide ($Ta_2O_5$) coated nanotubes. The results demonstrate that the osteofunctionality is even further enhanced by the Ta oxide nanotube surfaces when compared to the $TiO_2$ nanotube surface and metallic Ta-coated nanotube surface.

### 4.3.1 Experimental Methods

***Nanotube Substrate Fabrication***

$TiO_2$ nanotube surfaces were created using a two electrode set-up anodization process as described previously [125]. A 0.25 mm thick commercially pure Ti sheet (99.5 % metal basis, Alfa-Aesar, USA) was used for this process, which was first cleaned successively in acetone and isopropyl alcohol with ultrasonication followed by DI water rinse. The nanotubes were prepared in a 1:7 volumetric ratio of acetic acid (≥99.99 % purity, Sigma-Aldrich, USA) to a weight percent fraction of 0.5 % hydrofluoric acid in water (48 % w/v, EM Science, USA) at 20 V for 30 min. A platinum electrode (99.9 %, Alfa-Aesar, USA) served as the cathode. The samples were then washed with deionized water, dried at 80° C. The as-made nanotubes were then treated in five different combinations of annealing and coating procedures.

**$TiO_2$ NTs:** The as-made $TiO_2$ nanotubes were heat treated at 500 °C for 2 h in order to crystallize the as-fabricated amorphous structured $TiO_2$ nanotubes to anatase structure.

**Ta-coated NTs:** After heat treatment as described in (1), tantalum films (20 nm-thick) were vacuum-deposited onto $TiO_2$ nanotube substrates from a tantalum target in a Denton Discovery 18 sputter system. To ensure preferential coating of the $TiO_2$ nanotube surface,

the deposition angle used was ~30° off the vertical axis with substrate rotation during deposition. 200 W plasma was applied when Ar pressure reached 3 mTorr after base pressure reached $10^{-6}$ torr. The as-deposited Ta film is expected to be of amorphous nature.

**$Ta_2O_5$-coated NTs:** After heat treatment as described in (1), $Ta_2O_5$ thin films (20 nm-thick) were vacuum-deposited onto the $TiO_2$ nanotube substrates using a sputtering system (Denton Discovery 18 Sputter System) at room temperature. The deposition of $Ta_2O_5$ was carried out at pressures up to 5 X $10^{-7}$ mTorr (base pressure). The RF sputtering power was 400 W when Ar pressure reached 3 mTorr gas pressure. The as-deposited $Ta_2O_5$ film is expected to be of amorphous nature.

***Contact Angle Measurement***

The measurement of contact angle for each of the nanotube surfaces was carried out using a video contact angle measurement system model VSA 2500 XE (AST Products Inc.). A small deionized water droplet (~3 mg) was placed on the nanotube surface to measure the static contact angle. Measurement of the contact angle is a simple method for analyzing the surface energy and hydrophilic nature of a surface. In this case we also wanted to verify that the tantalum (more

hydrophilic in nature compared with $TiO_2$) had been deposited and to observe the changes in surface energy after deposition and heat treatment procedures.

***Osteoblast Cell Culture***

For these studies, human osteoblast (HOb) cells (406-05a, Cell Applications, Inc., USA) were used. Each 1 ml of cryo-conserved stock was mixed with 10 ml of alpha minimum essential medium (αMEM; Invitrogen, USA) in the presence of a volume fraction of 10 % fetal bovine serum (FBS; Invitrogen, USA) and a volume fraction of 1 % penicillin-streptomycin (PS; Invitrogen, USA). The cell suspension was plated in a polystyrene cell culture dish and incubated at 37° C in a volume fraction of 5 % $CO_2$ environment. Each 1.27 × 1.27 $cm^2$ experimental substrate ($TiO_2$ nanotubes and each category of Ta-coated nanotubes) was placed into individual wells of a 12-well polystyrene plate. The polystyrene (PS) culture dish was used as a control. When the cells reached confluency, the HOb osteoblast cells were seeded at a concentration of $2.5\times10^4$ cells per well onto the experimental substrates and stored in a $CO_2$ incubator for the experimental time durations. All osteoblast cells for this study were used at passage 5. For experimental time points beyond 7 d of culture, cell media was changed at 7 d to osteogenic induced media, αMEM containing a volume fraction of 10 % FBS, a volume fraction

of 1 % PS, 10 nmol/L dexamethasone (Sigma, USA), 150 µg/ml ascorbic acid (Sigma, USA) and 10 mmol/L β-glycerol phosphate (Sigma, USA). All experimental substrates were moved to a new 12-well dish before cell assays were performed in order to isolate the cells on the substrate of interest from cells on the surrounding polystyrene dish.

**MTT Assay**

To estimate the metabolic activity of the cells, an MTT (3-(4,5-dimethylthiazole-2-yl)-2,5-diphenyl tetrazolium bromide) assay was employed. After the selected incubation periods, the samples were washed by PBS and transferred to a new 12-well polystyrene culture plate. Fresh cell culture media was added to each well, and the MTT dye agent was added in an amount equal to 10 % of the culture media volume, according to manufacturer's instructions (MTT kit, Sigma, USA). After 2 h of incubation in a 5 % $CO_2$ incubator, 1 ml of solubilizing solution was added to each well and the polystyrene plate was shaken for 30 sec to dissolve the formazan crystals. The fluorescent absorbance of each solution was measured at a wavelength of 570 nm with the subtraction of the 650 nm background by ultraviolet-visible (UV-vis) spectrophotometer (Biomate™ 3, Thermo Electron Co., USA).

***Scanning Electron Microscopy (SEM) for Cell and Substrate Examination***

After 24 h of culture, the cells on the substrates were washed with PBS and fixed with a mass fraction of 2.5 % glutaraldehyde (Sigma, USA) in PBS for 1 h. After fixation, they were washed three times with PBS for 15 min each wash. The cells were then dehydrated in a graded series of ethanol (volume fractions of 50, 75, 90 and 100 %) for 30 min each and left in 100 % ethanol to be dried by a critical point dryer (EMS 850, Electron Microscopy Science Co., USA). Next, the dried samples were sputter-coated with palladium metallization for examination by scanning electron microscopy (SEM). The morphology of the samples as well as that of the adhered cells was observed using a Phillips XL30 field emission environmental scanning electron microscope (FEI Co., USA).

***Immunofluorescence of Cytoskeletal Actin***

After 24 h of culture, the cells were fixed in 4 % paraformaldehyde in PBS for 15 min at room temperature. Once fixed, the cells were washed twice with wash buffer (PBS containing a volume fraction of 0.05 %Tween-20). To permeabilize the cells, 0.1 % Triton X-100 in PBS was added for 10 min, followed by washing twice with wash buffer. TRITC-conjugated phalloidin (1:1000 Chemicom International) in PBS was added and incubated for 1 h at room temperature, after which the cells were washed three times with wash buffer for 5 min each wash. Samples were then

inverted onto coverslips with a dab of Fluoromount-G (Electron Microscopy Sciences, USA), visualized and photographed using a Rhodamine (536 nm excitation) filter by a fluorescence Leica, Co. DM IRB microscope.

***Alkaline Phosphatase Activity Test***

In order to measure the bone forming ability of cells on the experimental surfaces, the alkaline phosphatase (ALP) activity was detected using a colorimetric assay kit. Briefly, after the selected incubation periods, the samples were washed by PBS and transferred to a new 12-well polystyrene culture plate. Cells were then gently washed twice with phosphate buffer provided by the kit supplier, followed by the addition of a volume fraction of 0.2 % Triton X-100 in phosphate buffer. The adherent cells were further scraped off of the sample substrate and collected in a microcentrifuge tube. Cell suspension was incubated on ice for 10 min under agitation, and then centrifuged at 2500 ×g for 10 min at 4°C. The supernatants were stored at -80°C until further analysis by AnaSpec SensoLyte pNPP Alkaline Phosphatase Assay Kit colorimetric assay (AnaSpec, Inc., USA) following the manufacturer's instructions. The ALP values were normalized by protein content obtained by a BCA kit (Sigma, USA).

***Energy Dispersive X-Ray Analysis***

Matrix mineralization was analyzed by energy dispersive X-ray analysis (EDX) after 21 d of culture. After the experimental culture time was complete, the cells were trypsinized by trypsin EDTA 0.25 % (Invitrogen, USA) and allowed to air dry for SEM and EDX analysis. Identical samples were incubated in cell-free media as a control. The Oxford EDX attachment and Inca Software were used to determine elemental composition of deposited bone matrix.

***Statistical Analysis and Error Bars on Graphs***

Sigma Plot 11.0 software (2008) was utilized to demonstrate the statistical significance of the assays. The graphs show the average ± standard error bars associated, with *p*-values listed in the figure captions.

## 4.3.2 Results and Discussion

Section 4.2 demonstrated a ~30% increase in the rate of bone mineralization on $TiO_2$ nanotubes modified with a thin conformal layer of tantalum (Ta) when compared to bare $TiO_2$ nanotubes. The tantalum film in the prior study was assumed to be in the amorphous metallic form, as no post-deposition treatment was performed. Considering the significant difference observed in the prior study between $TiO_2$ and Ta-coated nanotubes, further investigation was necessary to understand the effect of the tantalum film on the behavior of human osteoblast cells. One

aspect of the tantalum film that we wanted to consider is the effect of the oxide content of the tantalum coated nanotubes on the osteogenic behavior. A number of studies have shown that titanium and tantalum both form a natural oxide layer when exposed to air, which has been attributed to the excellent biocompatibility of these materials [130-131]. Additional studies, however, have shown that protein absorption was markedly increased with increasing thickness of an oxide layer on the surface of tantalum [131]. Since the first interaction in the sequence of events at the biomaterial implant surface is the absorption of proteins, this trend is of importance when considering a biomaterial composed of tantalum. Thus, in order to compare the osteoblast response to metallic and oxidized tantalum surface chemistries on the nanotube geometry, three sample types were prepared: (1) $TiO_2$ nanotubes (NTs), (2) amorphous metallic Ta-coated NTs, and (3) amorphous $Ta_2O_5$-coated NTs, as described in detail in the Materials and Methods.

**Figure 4.3-1**presents SEM images of each of the experimental nanotube surfaces. The images reveal near identical surface structures, with an outer diameter of ~100 nm, ~10 nm wall thickness, ~10 nm spacing, and ~300 nm height, as previously described [2, 125]. The Ta and $Ta_2O_5$ coating performed by vacuum sputter deposition allows for deposition of a conformal layer with high control of the Ta thickness (20

nm). Both tantalum and tantalum oxide are reported to be biocompatible materials, with excellent corrosion resistance and low solubility and toxicity [129, 158]. The contact angle measurements of each surface are reported in yellow in the upper right corner of each figure. The $TiO_2$ nanotube surface contact angle of a water droplet was ~4°; the contact angle on the Ta and $Ta_2O_5$ coated nanotube surfaces was ~0°. The presence of the Ta and $Ta_2O_5$ coatings was confirmed via energy dispersive x-ray (EDX) analysis. In addition, the relative oxygen content of each substrate was measured, and is shown in the graph in **Figure 4.3-1**. These measurements include oxygen content of not only the surface, but also the nanotube length and bulk Ti substrates (as far as the x-ray beam can penetrate). However, the relative amounts show increased oxygen content on the $Ta_2O_5$-coated nanotube substrate, as expected.

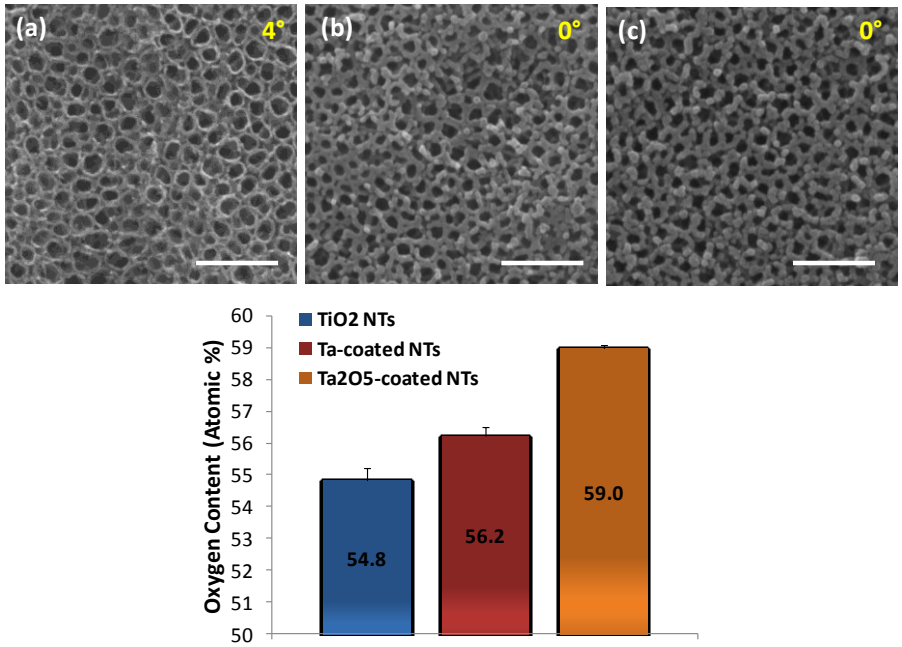


**Figure 4.3-1. Top:** SEM micrographs of each of the experimental nanotube surfaces, with water contact angles for each surface displayed in the upper right corner in yellow. Scale bars = 500 nm. **(a)** $TiO_2$ NTs, **(b)** Ta-coated NTs, and **(c)** $Ta_2O_5$-coated NTs. **Bottom:** EDX analysis of the atomic percent of oxygen on the experimental surfaces.

The cytoskeletal actin organization and cell morphology on each of the nanotube substrates is shown in **Figure 4.3-2**. The top row depicts immunofluorescent staining of the cytoskeletal actin of HObs after 24 h of culture on the various surfaces, and the bottom row shows SEM images of the HObs after 24 h of culture. In both the actin and SEM images, the cells appear to be relatively unaffected by the changes in surface oxidation. The cells maintain elongated shapes, with significant lamellipodial and filopodial protrusions characteristic of osteoblast and osteoprogenitor cellular response to the nanotube surface geometry [2-3]. The elongated leading edges of lamellipodia are indicated on the SEM images by yellow

arrows. These lamellipodia suggest that the cells are relatively motile and activated by the nanotube architecture, but are not necessarily influenced by the surface oxide composition.

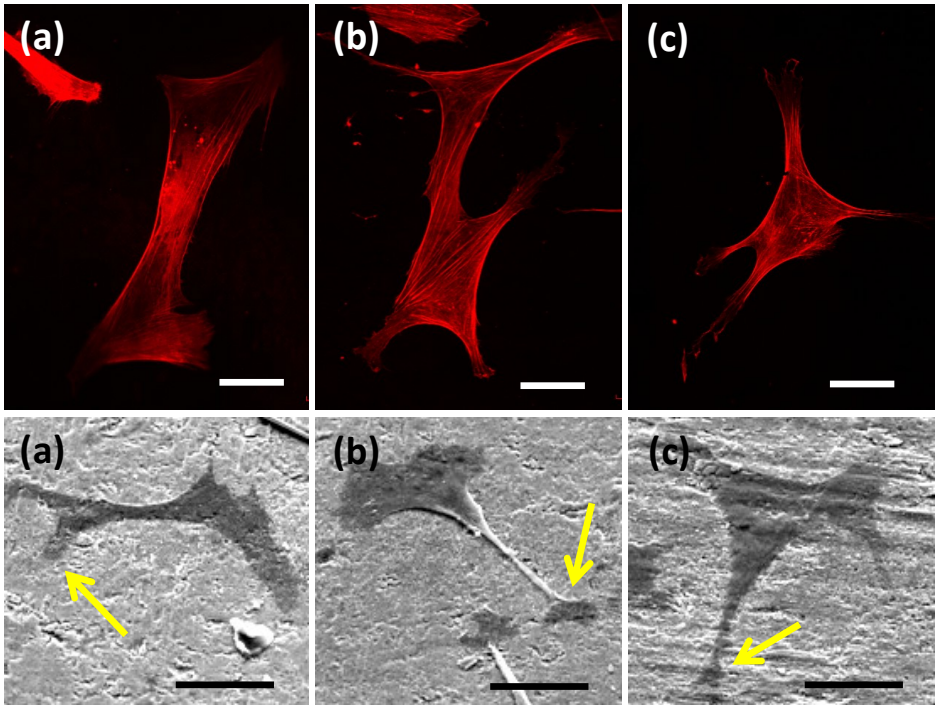


**Figure 4.3-2. Top Row:** Immunofluorescent images of cytoskeletal actin (red) of HOb cells after 24 h of culture incubation, showing a criss-cross pattern on both $TiO_2$ and Ta surfaces (yellow arrows). Scale bars = 50 μm. **Bottom Row:** SEM micrographs of HOb cells after 24 h incubation. Scale bars = 50 μm. **(a)** $TiO_2$ NTs, **(b)** Ta-coated NTs, and **(c)** $Ta_2O_5$-coated NTs. The elongated leading edges of lamellipodia are indicated by yellow arrows.

The cell adhesion and proliferation was also not significantly affected by the various surface chemistries in this study. The metabolic activity of the cells was measured using an MTT assay in order to indirectly estimate the number of viable cells. Results of the MTT analysis in **Figure 4.3-3** show that the cells proliferated on each of the nanotube surfaces well, with a slight trend of increasing cell viability from $TiO_2$ to Ta to $Ta_2O_5$,

however no statistical difference between substrates was observed. We hypothesize that the initial cell response to a surface is more highly influenced by substrate topography and surface energy than by surface oxide content.

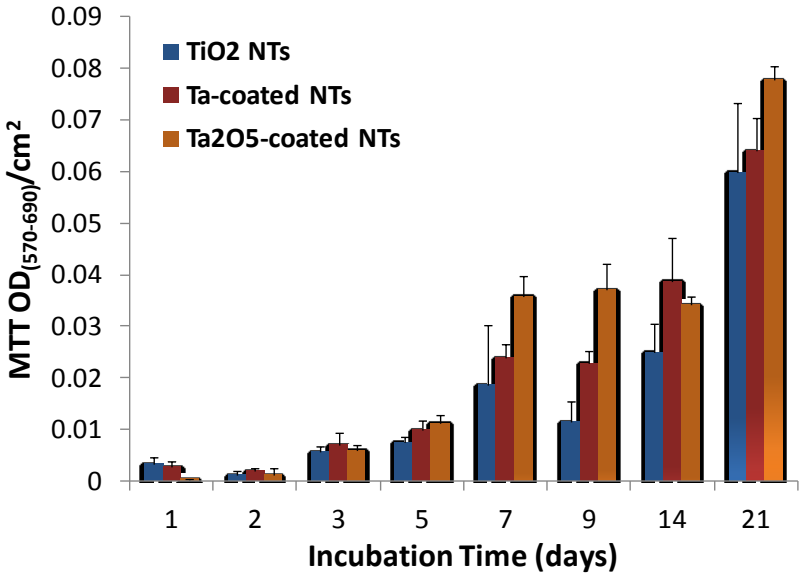


**Figure 4.3-3.** MTT assay data showing the optical density (OD) of the reaction product of the MTT working solution of HOb cells cultured on the nanotube surfaces as a function of incubation time (*n* = 3). The bar graph shows the mean ± standard error bars.

In order to assess the functionality of the osteoblast cells, the alkaline phosphatase (ALP) activity was measured as a function of incubation time (**Figure 4.3-4**). Alkaline phosphatase is an enzyme that indicates the bone-forming ability of osteoblast cells. Although no significant difference was observed at shorter time points, at 9 days both the Ta and $Ta_2O_5$ coated nanotube surfaces were significantly higher than the $TiO_2$ nanotubes (but no difference was observed between the

metallic and oxide Ta-coated NTs). However, at 14 and 21 days, a consistent trend was apparent in which the ALP activity was highest on the amorphous $Ta_2O_5$-coated NTs, followed by the amorphous Ta-coated NTs. These results indicate that at more advanced times points, the osteoblast cells respond more positively to tantalum oxide than to metallic tantalum.

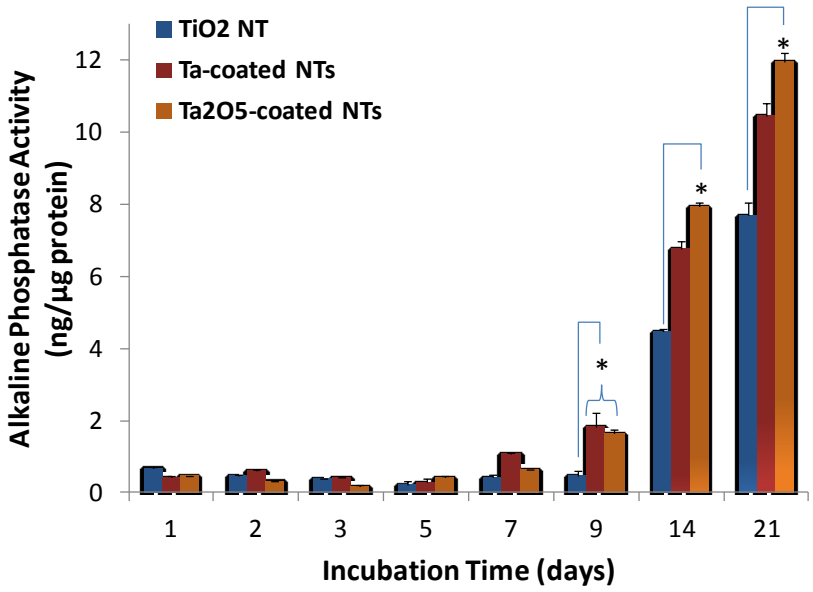


**Figure 4.3-4.** ALP activity of HOb cells cultured on the nanotube surfaces vs. incubation time ($n$ = 3). The graph points show the mean ± standard error bars. The $p$-values after performing an ANOVA test reached statistical significance ($p \leq 0.001$), for the comparison between sample types indicated by the arrows and (*).

The bone-forming functionality of the osteoblast cells was also analyzed by measuring the relative amounts of calcium and phosphorus deposited on each surface via energy dispersive x-ray analysis (EDX). The atomic percents of each atom reported in **Figure 4.3-5(a)** indicate that there were significantly greater amounts of calcium and phosphorus

present on the $Ta_2O_5$-coated nanotube substrate when compared to the $TiO_2$ nanotube and Ta-coated NT. **Figure 4.3-5(b)** shows SEM images of the matrix deposits on each surface for visual comparison with the quantified EDX data in the graph. The largest mineral deposits are apparent on Ta-oxide surface when compared to the $TiO_2$ nanotubes and metallic Ta-coated surface. The trends observed in the ALP activity in **Figure 4.3-4**are also supported by the trends in the mineralized matrix amounts.

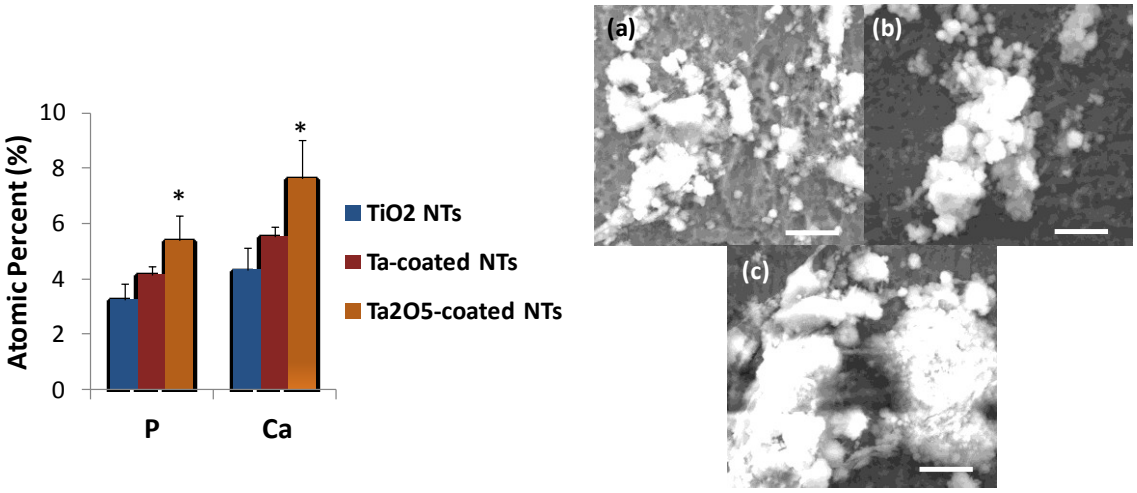


**Figure 4.3-5.** Bone nodule formation by HOb cells cultured for 3 weeks. **(Left)** EDX analysis of the atomic percent of calcium and phosphorus mineral elements on the surfaces (*n* = 5). The bar graph shows the mean ± standard error bars. The *p*-values after performing an ANOVA test reached statistical significance ($p \leq 0.05$), as indicated by (*). **(Right)** SEM micrographs at 2000x showing larger bone matrix deposits on the $Ta_2O_5$-coated nanotube surface. Scale bars = 10 µm. **(a)** $TiO_2$ NTs, **(b)** Ta-coated NTs, and **(c)** $Ta_2O_5$-coated NTs.

Although no significant difference was detected in the data from the earlier incubation time points (less than 7 days), at day 9 to 21 the $Ta_2O_5$ coating appears to have triggered an upregulated osteogenic

functionality. This can be concluded by the enhanced ALP activity and evidence of more matrix deposits at advanced incubation stages. One possible explanation for this trend could be that there is a greater percentage of oxygen in the $Ta_2O_5$-coated nanotube substrate when compared to the other samples, as shown in the graph of comparative amounts of oxygen in **Figure 4.3-1**. Studies in the past have contributed surface oxide thickness to increased protein absorption on the surface of tantalum [131]. Additionally, greater osteoblast adhesion and activity has been correlated to more surface hydroxyl groups on titanium [130]. It is possible that the higher percentage of surface oxygen on the $Ta_2O_5$-coated nanotube surface induces an accumulation of more proteins on the surface, which leads to faster osteoblast maturity and matrix mineralization.

The purpose of this study was to provide a comparative analysis of the effects of the anodic nanotube architecture with varied surface chemistry ($TiO_2$, Ta, and $Ta_2O_5$) on osteoblast growth and maturation. The results of this study have shown that although an amorphous metallic Ta coating can induce a more highly active osteoblast behavior than the bare $TiO_2$ nanotube surface, these effects can be considerably improved using an amorphous $Ta_2O_5$ coating, which may be attributed to higher surface oxygen content. Future studies should provide a direct

comparison between the amorphous and crystalline tantalum and tantalum oxide coatings on the nanotube architecture since differences have been observed in osteoblast response to amorphous and crystalline $TiO_2$ nanotubes [125]. It would also be of interest to perform similar experiments with osteoprogenitor cells, since it is known that there are differences in cell preferences of physical and chemical cues [74]. It is possible that the $Ta_2O_5$ surface chemistry would also further enhance the osteoprogenitor cell response.

### 4.3.3 Conclusion

In this work, we have compared the response of human osteoblast cells to three nanotube surfaces of identical geometry, but various chemistries: the bare $TiO_2$ nanotubes, Ta-coated nanotubes, and $Ta_2O_5$-coated nanotubes. The purpose of this experiment was to analyze the effect of surface oxide content in a tantalum thin film on the osteogenic behavior of human osteoblast cells. Although no difference was observed at brief incubation time points (less than 7 days), at advanced stages we observed an upregulation in ALP activity, as well as a significant increase in bone matrix mineralization on the tantalum oxide coated nanotube surface when compared to the bare $TiO_2$ nanotubes and metallic tantalum coated nanotubes. These results indicate that the oxide content of a biomaterial surface may provide a significant

opportunity for enhancing the bone-forming ability of osteoblasts grown thereon.

## 4.4 Conclusions & Future Directions

The findings presented in this chapter demonstrate the highly complex interaction between the cell and a biomaterial surface, and that cellular behavior is easily influenced by both surface chemical and nanotopographical cues. It has been illustrated that:

i. Osteoblast cells have opposite preferences as osteoprogenitor cells when in contact with $TiO_2$ and carbon,
ii. Osteoblast cells show preference for Ta over $TiO_2$ nanostructured surfaces,
iii. Osteoblast cells show preference for $Ta_2O_5$ over Ta and $TiO_2$,

The overall conclusion that can be obtained from these findings implies that unique combinations of surface chemistry and nanostructure may influence cell behavior due to distinctive physico-chemical properties. Further studies are required to gain insight to the phenomenon observed in this work, such as comparative analysis of protein adsorption, hydroxyapatite formation, and biomolecular interaction with the nanotube surfaces of various surface chemistries. These findings are of paramount importance to the orthopedics field for understanding cell

behavior in response to subtle alterations in nanostructure and surface chemistry, and will enable further insight into the complex manipulation of biomaterial surfaces. With increased focus in the field of orthopedic materials research on nanostructured surfaces, this study emphasizes the need for careful and systematic review of variations in surface chemistry in concurrence with nanotopographical changes.

*Chapter 4, section 1 contains a reprint in part of the material as it appears in Acta Biomaterialia Volume 7 (6), 2011, Page 2697 written by Karla S. Brammer, Chulmin Choi, Christine J. Frandsen, Seunghan Oh, Gary Johnston, and Sungho Jin. The dissertation author is a collaborating investigator and author of this publication. Chapter 4, section 2 contains a reprint in part of the material as it has been prepared for submission for publication, written by Christine J. Frandsen, Karla S. Brammer, Kunbae Noh, Gary W. Johnston, and Sungho Jin. The dissertation author is the primary investigator and author of this publication. Chapter 4, section 3 contains a reprint in part of the material as it has been prepared for submission for publication, written by Christine J. Frandsen, Karla S. Brammer, Gary W. Johnston, Chulmin Choi, and Sungho Jin. The dissertation author is the primary investigator and author of this publication.*

# CHAPTER 5

## 5. $TiO_2$ Nanotube Coatings on Femoral Knee Implant Materials

The advantages of the nanotube architecture as an advanced orthopedic implant surface structure have been well-demonstrated in previous chapters of this dissertation. The studies discussed thus far have been focused on nanotubes fabricated from a bulk Ti or Zr substrate, with the intended eventual application being a bulk orthopedic implant consisting of a medical grade metal alloy consisting of mainly Ti or Zr. For example, the anodization procedure could easily be scaled-up to produce a nanotube surface coating covering the outer surfaces of a bulk titanium alloy orthopedic implant. However, there exist several other widely used orthopedic implant materials for which the electrochemical anodization technique could not be directly applied, meaning nanotube formation has not been shown to occur via the same mechanism as with Ti or Zr. Such alternative materials include, for example, cobalt chromium (CoCr) alloys, stainless steel, zirconia ($ZrO_2$) ceramics, and polymers such as polyethylene. These orthopedic materials maintain similar relatively short implant lifetimes as do Ti and Zr, and thus novel bone-integrating surfaces are of interest for these materials as well. Thus, it would be of interest to develop a method in which a nanotube coating could be

applied to any of these implant materials as an advanced bone-integrating surface, enabling a more versatile application. The work presented in this chapter discusses the application of a thin film of titanium to various substrate materials, followed by electrochemical anodization, in order to introduce a $TiO_2$ nanotube surface coating.

## 5.1 Increased Osteoblast Adhesion and Spreading on a $TiO_2$ Nanotube-Coated Commercial Zirconia Femoral Knee Implant *In Vitro*

Zirconia ($ZrO_2$) was introduced as an orthopedic implant material in 1985, and is well known as one of the highest-strength ceramics suitable for medical use [159]. In particular, zirconia has been found to be a choice material for the femoral component of the total knee implant when compared to the more commonly used CoCr, due to a reduction in polyethylene wear [160]. Although zirconia orthopedic implants received a poor reputation in the late 90s due to failures found to be a result of a change in the heat treatment procedure, a much better understanding of the ceramic aging and degradation behavior and prevention techniques has been obtained [161-162], and the material is becoming popular again.

While the current success of total knee replacement (TKR) is much improved from pioneering knee implant designs, further improvements are necessary for increased implant lifetime. Some studies have shown that the failure rate of TKR is greater in younger patients due to a higher level of activity [163]. The most common reasons for TKR revision surgery are aseptic loosening and instability [164]. The reasons for aseptic loosening are multifactorial [165]. However, in general, the source of the problem lies in osteolysis at the bone-implant interface. As such, one area for implant lifetime improvement is in strengthening the osseointegration of the implant.

There is much controversy on the benefits of cemented versus uncemented fixation techniques of TKRs. Uncemented fixation for TKR was introduced as a method of potentially increasing implant longevity [166]. The presence of a more physiological bond between the bone and the implant is considered by some to provide a stronger device [167]. While studies in the literature often favor cemented fixation, some more recent studies suggest that there is not a significant difference between the fixation methods [167-168], and both are equally recommended in terms of implant performance.

It has been well-established that the presence of nanotopography affects basic cell behavior in almost all types of mammalian cells [169].

Of particular interest are titanium oxide ($TiO_2$) nanotubes, since titanium is a well-known biocompatible orthopedic material. $TiO_2$ nanotubes have been found not only to significantly accelerate osteoblast cell growth, but also improve bone-forming functionality and direct stem cell fate. These results are especially promising for well-established titanium bone implants currently on the market, since aseptic loosening is still a relevant problem in orthopedic implants. The nanotube surface structure can essentially be added to any shape of titanium implant by a simple anodization procedure. Additionally, $TiO_2$ nanotubes can be grown from a thin film of titanium deposited onto another surface. This expands the possible applications to not only current titanium implants, but other types of implants as well.

In this work, a commercial zirconia ceramic femoral knee component was sputter coated with a thin film of titanium on the bone bonding (backside) surface, and further anodized to form a coating of $TiO_2$ nanotubes. Osteoblast viability, adhesion, and spreading was analyzed and compared on the $TiO_2$ nanotube coating and bare zirconia implant surface. Here we report an improvement of osteoblast cell adhesion and spreading on the $TiO_2$ nanotube coated implant.

### 5.1.1 Experimental Methods

#### *$TiO_2$ Nanotube-Coated Implant Preparation*

A zirconia ceramic femoral knee component was obtained from Kinamed, Inc. (GEM™ Total Knee System, Cat # 20-120-1001) and was cleaved into six pieces in a manner which maximized the sample surface area of relatively flat backside implant surface. Two of the pieces were set aside to be used as controls in this study, while the remaining four pieces were taken for further processing. Before film deposition, $ZrO_2$ implant materials were cleaned successively in acetone and isopropyl alcohol with ultrasonication. Ti thin film was vacuum-deposited using Denton Discovery 18 sputter system. Base pressure was $1\sim10^{-6}$ torr and substrate being rotated was heated to 400 °C during sputtering. Plasma power was 200 W and Ar pressure was 3.0 mTorr. Deposition rate was 0.25 nm/s and 1 μm thick Ti film was deposited. Electrical contact for the anodization step was provided by copper tape and a laquer protective paint. The $TiO_2$ nanotube surfaces were created using a two-electrode-setup anodization process. An organic-based electrochemical solution was used which was composed of 0.25 wt% $NH_4F$ in 2 vol% deionized water in ethylene glycol. A platinum electrode (99.9% pure, Alfa-Aesar, USA) served as the cathode. The samples were anodized at 20 V for 15 min, followed by a washing step with ethanol, and an acetone soak to

remove the lacquer paint. The samples were then dried at 80 °C overnight and heat-treated at 500 °C for 2 h in order to crystallize the as-fabricated amorphous structured $TiO_2$ nanotubes into an anatase structure. The samples used for all experiments were sterilized by autoclaving prior to use. The bare zirconia implant samples were used as a control after being chemically cleaned by acetone and isopropanol, dried and autoclaved.

***Adhesion Strength Test***

For adhesion strength of $TiO_2$ nanotube coating on the zirconia implant materials, a simple adhesion set-up was utilized. Commercial thermosetting epoxy was attached on the surface of the $TiO_2$ nanotubes and a hook-shaped metal wire end was tightly embedded inside the epoxy. The adhered area of epoxy was 0.2 $cm^2$. After the epoxy was fully cured, uniaxial force was applied normal to the surface. Adhesion strength was indirectly determined whether fracture occurred along the epoxy/$TiO_2$ nanotube interface or $TiO_2$ nanotube/implant interface. In result, adhesion strength was at least greater than 460 $lb/in^2$ in which epoxy was detached from $TiO_2$ nanotube surface with a sharp facture interface.

***Contact Angle Measurement***

The measurement of contact angle for the bare implant and $TiO_2$ nanotube surfaces was carried out by a video contact angle measurement system (Model No. VSA 2500 XE, AST Products, Inc.).

***Osteoblast Cell Culture***

For this study, MC3T3-E1 mouse osteoblast (CRL-2593, subclone 4, ATCC, USA) were used. Each 1 ml of cells was mixed with 10 ml of alpha minimum essential medium (a-DMEM; Invitrogen, USA) in the presence of 10 vol.% bovine serum (FBS; Invitrogen, USA) and 1 vol.% penicillin-streptomycin (PS; Invitrogen, USA). The cell suspension was plated in a cell culture dish and incubated at 37°C in a 5 vol.% $CO_2$ environment. When the concentration of the MC3T3-E1 osteoblastic cells reached confluency, they were seeded onto the experimental substrate of interest ($TiO_2$ nanotubes or bare implant), which was placed on a 6-well polystyrene plate and stored in a $CO_2$ incubator for 24 and 48 h to observe the cell morphology and adhesion. The concentration of the cells seeded onto the substrate was $1.5 \times 10^5$ cells per well.

***Cell Viability, Adhesion, and Spreading Test***

Fluorescein diacetate (FDA; Sigma, USA) staining was conducted to visualize cell viability and to quantify cell spreading. At 24 h after plating, the cells on the substrates were washed with phosphate-buffered saline (1

x PBS) solution (Invitrogen, USA) and incubated for approximately 30 s with FDA stock (5 mg dissolved in 1 ml of acetone) dissolved in PBS (10µl/10ml), and washed once more. The samples were then inverted into new wells, visualized and photographed using a fluorescence microscope with a green filter (DM IRB, Leica Co., USA). Six fields were randomly chosen from each sample. The digital images were stored in a 672 x 512 pixels file and imported to a TIF format. Stored images were imported to ImageJ image processing program for digital analysis. The number of adherent cells were counted in each image. Additionally, the total cell spreading area was quantified.

***SEM for Substrate and Cell Morphological Examination***

After 24 h of culture, the cells on the substrates were washed with PBS and fixed with 2.5% w/v glutaraldehyde (Sigma, USA) in PBS for 1 hour. After fixation, they were washed three times with PBS for 10 min each wash. The cells were then dehydrated in a graded series of ethanol (50, 75, 90, 100 vol.%) for 30 min each and left in 100% ethanol overnight. The substrates were then dried by a critical point dryer (EMS 850, Electron Microscopy Science Co., USA). Next, the dried samples were sputter-coated with palladium for examination by scanning electron microscopy (SEM). The morphology of the $TiO_2$ nanotubes and bare implant as well as

that of the adhered cells were observed using an XL30 scanning electron microscope (FEI Co., USA).

***Statistical Analysis and Error Bars on Graphs***

SigmaPlot 11.0 software (2008), which specializes in scientific data analysis and presentation, was utilized to demonstrate the statistical significance of the spreading assay. The graph shows the average ± standard error bars associated, with the sample size (or *N* values) shown in a box in the upper portion of the graph.

## 5.1.2 Results and Discussion

The zirconia ($ZrO_2$) ceramic femoral knee component obtained from Kinamed, Inc. (GEM™ Total Knee System, Cat # 20-120-1001) for modification and experimentation in this study is pictured in **Figure 5.1-1**, as received. The bone-integrating (backside) surface of the femoral knee implant is shown facing upward (the dull surface) in this photograph, while the articulating (shiny) surface is facing downward. This implant was cut into six sample pieces for use in the study herein.

**Figure 5.1-1.** Photograph of the as-received commercial zirconia femoral knee implant.

**Figure 5.1-2**shows SEM micrographs of the as-received zirconia implant surface **(a)**, and the $TiO_2$ nanotube coated implant surface **(b)**. The two surfaces look relatively similar when viewed at a lower magnification, with micron-rough surface features. However, the insets of each image reveal the nanotopography present on the $TiO_2$ nanotube surface. The self-assembled nanotube surface was obtained by anodizing the titanium sputter-coated zirconia femoral implant at 20 V an organic-based electrolytic solution. The nanotube pore size is ~50 nm, with a length of ~200 nm.

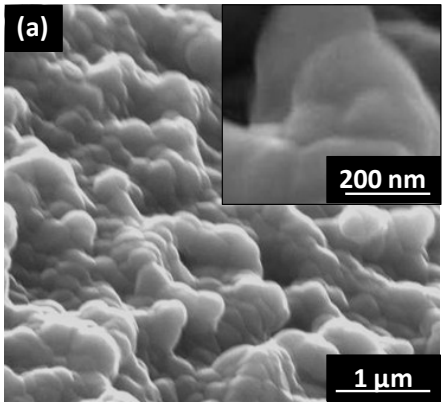


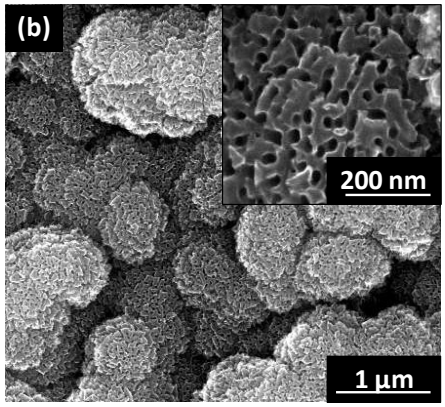


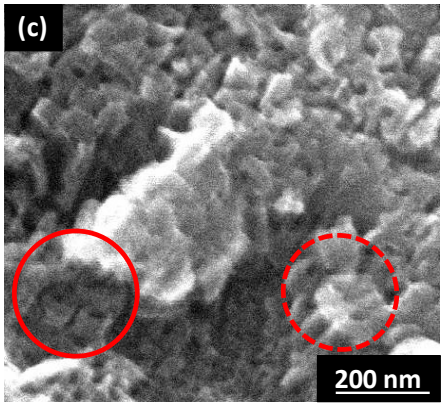


(d)

| Sample | Contact Angle (°) |
|---|---|
| Bare implant | 65 |
| Ti coated implant | 0 |
| $TiO_2$ NT coated implant | 0 |

**Figure 5.1-2.** Physical characterization of the as-received zirconia implant and $TiO_2$ nanotube coated implant surfaces. **(a)** SEM micrographs of bare implant surface, with higher magnification in the inset (tilted 45° angle). **(b)** SEM micrographs of the $TiO_2$ nanotube coated implant surface. **(c)** Tilted view SEM micrograph showing the nanotube opening (solid circle) underneath a porous top layer (dashed circle). **(d)** Table with surface contact angle measurements of water droplets on the bare implant, titanium coated implant, and $TiO_2$ nanotube coated implant surfaces.

While the top-view of the $TiO_2$ nanotube surface appears slightly more porous in nature, tube morphology was verified to be present underneath a porous top layer, as seen in **Figure 5.1-2(c)**. The solid circle shows the tube-surface, while the dashed circle shows the porous top layer. This configuration of $TiO_2$ nanotubes with a porous surface morphology was clearly explained by Wang, et al. to be the result of an imbalance in two competitive reactions which occur during $TiO_2$

nanotube formation [170]. Further optimization of our anodization conditions could result in a tube-like surface morphology. However, for the purposes of this study we analyzed the porous $TiO_2$ nanotube surface morphology in comparison with the bare implant material.

The SEM images show that a micron-scale surface roughness is present on the as-received implant; the nanotube coated implant possesses the same microtopography, in addition to the nanotopography created by the porous nanotube surface. The surface contact angle measurements of water droplets on each surface revealed that the titanium surface coating altered the as-received implant surface to become extremely hydrophilic in nature, while the as-received implant was only slightly hydrophilic. The $TiO_2$ nanotube coated implant was also superhydrophilic, with a contact angle of 0°.

To investigate the cell behavior in response to the as-received and modified implant surfaces, osteoblast cells were seeded on the comparative surfaces at a cell density of $1.5 \times 10^5$ per well. As indicated in **Figure 5.1-3**, cell adhesion and spreading after 24 h of culture was found to be increased on the $TiO_2$ nanotube surface in comparison to the bare implant surface. The plots of the quantification of the fluorescent images (**Figure 5.1-4**) clearly confirm these trends. Both the number of adhered cells (**Figure 5.1-4(a)**) and cell spreading area (**Figure 5.1-4(b)**)

were significantly increased on the nanotube surface. These results are in agreement with our previously reported investigations of osteoblast behavior on $TiO_2$ nanotube surfaces when compared to flat Ti foil [1-2]. It is likely that the increase in cell adhesion and spreading is a direct result of the superhydrophilic nature of the nanotube-coated surface. Many researchers have demonstrated the positive effects of superhydrophilic biomaterials on protein and cell adhesion properties [171-172].

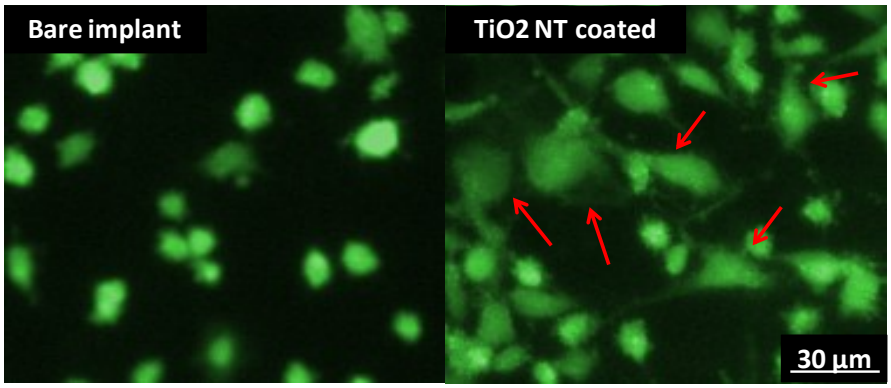


**Figure 5.1-3.** FDA viability of osteoblast cells after 24 hours of incubation on the bare zirconia implant and $TiO_2$ nanotube coating on the zirconia implant. More spreading is evident on the nanotube surface which indicates greater cell adhesion. Red arrows indicate significant cell spreading.

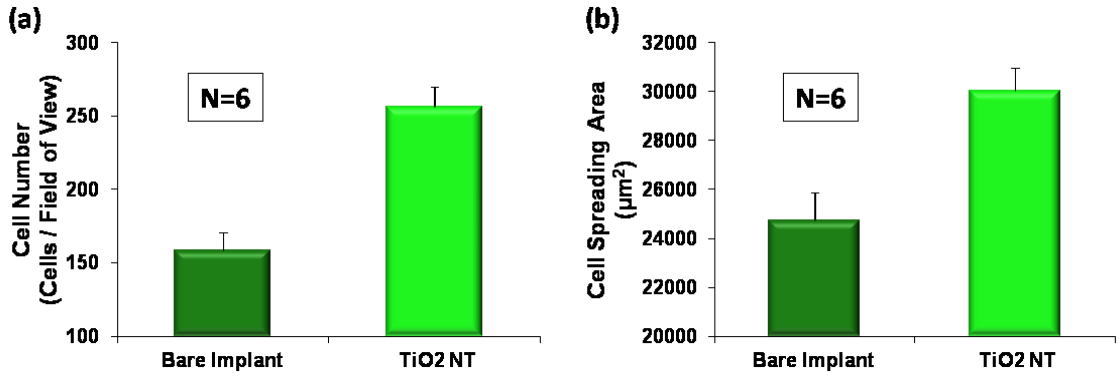


**Figure 5.1-4.** Cell number **(a)** and spreading area **(b)** after 24 hours of incubation. The bar graphs show the average ± standard error bars. The *p*-value after performing a *t*-test confirmed a statistical significance ($p < 0.005$).

The higher degree of cell adhesion and spreading was further confirmed by SEM, as shown in **Figure 5.1-5**. On the bare zirconia implant surface (**Figure 5.1-5(a)** and **(c)**), the cells appear to be unable to attach to the surface. Although there are many filopodial extensions present, rarely are they in contact with the surface, as indicated by the red arrows. In contrast, the cells on the $TiO_2$ nanotube coated implant surface (**Figure 5.1-5(b)** and **(d)**) are clearly integrating into the surface, and no floating filipodia are evident. The higher magnification images of the cell edge (**Figure 5.1-5(c)** and **(d)**) emphasize the unmistakable cell-surface interaction evident on the $TiO_2$ nanotube coated implant. It can be speculated that the increase in cell-surface interaction can be contributed to two key reasons. Firstly, as mentioned previously, the alteration from a slightly hydrophobic surface to an extremely hydrophilic surface is likely to enhance cell adhesion and spreading capabilities.

Secondly, the presence of nanotopography in addition to the bare implant microtopography may have an impact on how the cells behave. A hierarchical hybrid micro/nano-textured titanium surface has been recently considered to create an improved surface structure for osseointegration [173]. While the nanotopography can be assumed to induce an increase in bone functionality, the microtopography contributes to the mechanical interlocking ability of the surface.

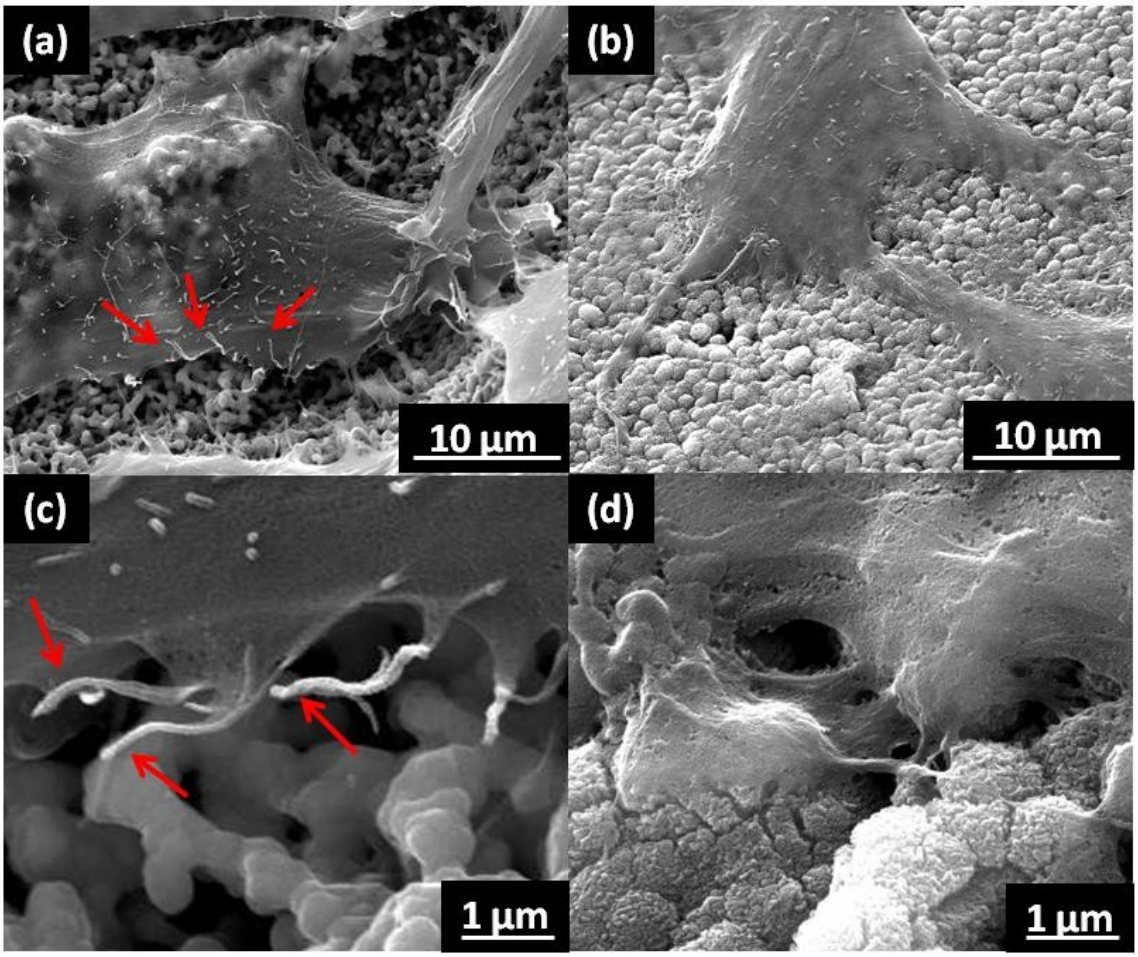


**Figure 5.1-5.** SEM micrographs of osteoblast cells after 24 hours of incubation on the bare zirconia implant (a, c), and $TiO_2$ nanotube coating on the zirconia implant (b, d). **(c)** and **(d)** are higher magnification of the cell edges on the respective surfaces. Red arrows indicate floating filopodia.

The spectrum of this study was limited by the number of commercial femoral implant samples available at the present time. Further studies should be performed in order to verify osteoblast functionality and maturation, as well as mesenchymal stem cell behavior on the surfaces in order to demonstrate the *in vitro* behavior of the two important cell types present at a bone implant interface. Furthermore, *in vivo* results should be assessed for more complete materials analysis.

### 5.1.3 Conclusion

This study was intended to facilitate the osseointegration of zirconia femoral knee implants by providing a novel hierarchical micro- and nano-structured titanium surface coating which encourages bone cell adhesion and integration. The results of this brief study provide sufficient evidence to encourage future studies. The development of such hierarchical micro and nano topographical features, as demonstrated in this work, can provide for insightful designs for advanced bone-inducing material coatings on ceramic orthopedic implant surfaces.

## 5.2 Fabrication of thin film $TiO_2$ nanotube arrays on Co-28Cr-6Mo alloy by anodization

Since Gong, et al. [42] first fabricated uniform $TiO_2$ nanotube arrays by anodizing titanium foil in hydrofluoric (HF) acid aqueous solution, many

researchers have investigated the mechanism, structural design, and application of anodic $TiO_2$ nanotubes, largely focusing on anodization of thick titanium foils [174-176]. However, the use of Ti foil for fabrication of $TiO_2$ nanotube arrays limits the promising application of this material architecture on other substrates [177]. Therefore, it is necessary to develop approaches to fabricate the highly ordered $TiO_2$ nanotube arrays directly on the desired substrates in order to expand the application field of $TiO_2$ nanotubes. Recently, one of the most studied methods is the deposition of titanium metal directly on the desired substrate and then anodizing the titanium thin film to obtain a $TiO_2$ nanotube array on this desired substrate. In the published studies, Ti thin films were deposited on various substrates such as silicon wafers, conductive glass and regular glass by employing sputtering techniques for applications such as solar cells, photovoltaic nanodevices, hydrogen sensors, and so on [178-182]. For example, Mor, et al. achieved nanotube arrays by anodizing radio frequency (RF) sputtered deposited titanium films at 500°C on a variety of substrates including glass and silicon in an electrolyte solution containing acetic acid and hydrofluoric acid [177, 183]. Yang, et al. obtained $TiO_2$ nanotube arrays by anodization of direct current (DC) sputtered Ti films on a silicon substrate at 500°C in a sodium fluoride (NaF) aqueous electrolyte [184].

To date, the focus of $TiO_2$ nanotube fabrication from thin films has been to utilize the attractive and unique ionic and electronic properties of $TiO_2$ nanotubes [185]. However, there is also a large interest in the applicability of $TiO_2$ nanotubes for next-generation orthopedic implants, since many benefits of such a surface topography for bone regeneration have been realized, including significantly accelerated osteoblast growth [1], enhanced bone-forming functionality [2], and even directing stem cell fate [3]. Two of the most common orthopedic implant materials in use today are composed of titanium (Ti) alloy or cobalt chromium (CoCr) alloy. For the case of the titanium alloy (Ti-6Al-4V), the potential fabrication of an anodized nanotube coating on the surface of a relatively large 3-D implant with intricate designs is altogether feasible with proper scale-up techniques [44]. However, to our knowledge such methods are not easily applied to a CoCr alloy surface.

As mentioned, Co-28Cr-6Mo is a medical grade alloy commonly used for surgical implants because of its high strength, superior corrosion resistance, non-magnetic behavior, and biocompatibility. The applications of Co-28Cr-6Mo alloy include prosthetic replacements of hips, knees, elbows, shoulders, ankles, and fingers; bone plates, screws, staples, and rods; and heart valves [186-187]. We believe that it could be highly advantageous to combine the well-recognized Co-28Cr-6Mo alloy

implant material with the advanced $TiO_2$ nanotube surface structure by preparing a $TiO_2$ nanotube array on a CoCr substrate. To our knowledge, few research studies have been carried out to investigate the anodization of deposited Ti thin film on Co-28Cr-6Mo alloy. In this paper, we achieved $TiO_2$ nanotube arrays by anodizing the DC-sputtered Ti/Au/Ti trilayer film on a Co-28Cr-6Mo alloy substrate. The effects of experimental parameters on the growth of $TiO_2$ nanotube were investigated to optimize the process. In addition, to demonstrate the biocompatibility of the nanostructured coating, adhered osteoblast cell morphology data is presented.

### 5.2.1 Experimental Methods

***Deposition of titanium film on Co-28Cr-6Mo substrate***

Two different types of medical grade Co-28Cr-6Mo alloy substrates (ASTM F-75 and ASTM F-799) were obtained in order to determine whether the substrate forming technique used (cast or forged) was significant. Titanium and gold film deposition was carried out on Co-28Cr-6Mo alloy substrates (17mm×22mm, cast Co-28Cr-6Mo, ASTM F-75; Φ13mm, thickness 1mm, forged Co-28Cr-6Mo, ASTM F-799) using direct-current sputtering. Before deposition, the Co-28Cr-6Mo alloy was cleaned by DI water, acetone, methanol, and isopropyl alcohol (IPA) sequentially. The deposition was carried out under an Ar flow rate of 37 sccm. The argon

pressure was 3 mTorr and the applied sputtering power was 200 W during the deposition process. The deposition temperature was held constantly at 400 °C. The base pressure was lower than $1\times10^{-6}$ torr, but pressure increased when heating chamber up to ~ $3\times10^{-6}$ torr. The substrate rotation was maintained at ~75 rpm and the deposition rate was approximately 15 nm/min. Two different deposited-film structures were made for comparison. The first deposited-film structure: a 20 nm Ti coating was firstly deposited on the Co-28-6Mo substrate, followed by a 50 nm Au layer and a 2 μm Ti layer were deposited in turn. The second deposited-film structure: a 2 μm Ti layer was deposited directly on the Co-28-6Mo substrate. **Figure 5.2-1** shows the schematic diagram of the Ti/Au/Ti trilayer and Ti monolayer deposited-film structure on Co-28Cr-6Mo alloy.

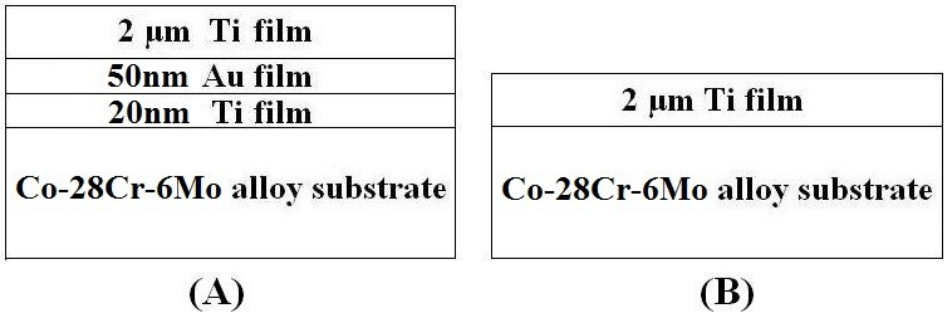


**Figure 5.2-1.** Schematic diagrams of two different deposition structures on Co-28Cr-6Mo alloy substrate: **(A)** Ti/Au/Ti trilayer; **(B)** Ti monolayer.

***Fabrication of the $TiO_2$ nanotubes by anodization***

Co-28Cr-6Mo alloy substrate was fixed to copper conductive tape to form the working electrode. The edge and back area of Co-28Cr-6Mo

alloy without Ti-deposited film were covered by a protective lacquer, leaving Ti film exposed to the electrolyte. This constant-voltage anodization was performed in a two-electrode configuration using a DC power supply (E3612A, Agilent) at room temperature. In this work, the applied voltage was 20 V. The electrolyte consisted of ammonium fluoride ($NH_4F$, 96%, Alfa Aesar) and distilled water in glycerol (99.9%, JT Baker). A platinum sheet was used as the counter-electrode. After anodization, samples were immediately washed in distilled water, and then dipped in a glycerol solution containing 6 vol% HF and 12 vol% $H_2O$ for 50 s to etch away the tangled debris existing on the surface of $TiO_2$ nanotube array. Subsequently, samples were cleaned by ultrasonication for 15 s and then dried with air stream. For the morphological characterization, a ultra high resolution field emission microscope (UHR SEM; FEI XL30) was employed. The cross-sectional images were taken from mechanically scratched samples.

***Osteoblast cell culture assay for morphological examination***

For these studies, human osteoblast (HOb) cells (406-05a, Cell Applications, Inc., USA) were used. Cell growth media consisted of alpha minimum essential medium (αMEM; Invitrogen, USA) in the presence of a volume fraction of 10% fetal bovine serum (FBS; Invitrogen, USA) and a volume fraction of 1% penicillin-streptomycin (PS; Invitrogen, USA). The

cells were incubated under the standard 37° C, 5% $CO_2$ environment. When the cells reached confluency, the HOb cells were seeded at a concentration of $2.5x10^4$ cells per well onto the experimental substrates (flat forged CoCr and $TiO_2$ nanotube coated forged CoCr) which were placed into individual wells of a 12-well polystyrene plate and stored in a $CO_2$ incubator for the experimental time durations. The polystyrene (PS) culture dish was used as a control.

Next, to observe the cellular morphology and filopodial activity of the attached cells, the cells were prepared for SEM examination. After 24 h, the cells on the substrates were washed with PBS and fixed with 2.5 wt% glutaraldehyde (Sigma, USA) in PBS for 1 h. After fixation, they were washed three times with PBS for 15 min each wash. The cells were then dehydrated in a graded series of ethanol (volume fractions of 50, 75, 90 and 100%) for 30 min each and left in 100% ethanol to be dried by a critical point dryer (EMS 850, Electron Microscopy Science Co., USA). Next, the dried samples were sputter-coated with palladium metallization for examination by scanning electron microscopy (SEM). The morphology of the adhered cells was observed using a Phillips XL30 field emission environmental scanning electron microscope (FEI Co., USA).

## 5.2.2 Results and Discussion

### *5.2.2.1 Effect of deposited-film structure*

The Co-28Cr-6Mo substrate itself seemed to be reactive with anodizing solution, especially when current was applied. When the Ti monolayer type sample (**Figure 5.2-1(b)**) was anodized, the Co-28Cr-6Mo substrate was easily damaged because the anodization end-point could not be properly detected. Thus, immediately after the entire Ti layer was consumed, the CoCr substrate was then exposed to electrolyte solution, which etched the underlying substrate surface. In order to provide a means for end-point detection, the trilayer structure was employed (**Figure 5.2-1(a)**).

In this work, the 50 nm gold (Au) thin film deposited between two Ti thin films was found to be important for proper control of the growth of the $TiO_2$ nanotube arrays. In the case of the Ti/Au/Ti trilayer structure, the Ti thin film between the CoCr substrate and Au layer serves as an adhesion layer. Accordingly, the Au layer was inserted to determine the anodization end-point as the anodization proceeded. A surge in the anodization current would indicate that the Au layer was exposed to the electrolyte solution, but since Au does not oxidize (noble metal), current would continue to flow as long as the circuit is closed. In contrast, if the current decreased down to 0, this would signal that the Ti layer on top of the Au

was entirely consumed so that $TiO_2$ served as an insulating layer. However, these opposite cases depend on $TiO_2$ barrier thickness and applied current whether anodizing current overcomes a threshold value for tunneling effect.

The corresponding current density vs. time curve of the anodization process of Ti/Au/Ti trilayer (deposited at 400 C°) is shown in **Figure 5.2-2**. The three regions labeled in this curve indicate three different phases of the anodization process. In region I, the current density dropped sharply at the beginning of the anodization and then slowly decreased as time progressed due to the formation of a compact oxide on the top of the Ti layer and the initial growth of $TiO_2$ nanotubes. During region II, the relatively constant low current indicates the steady growth of the $TiO_2$ nanotube arrays. An abnormal increase of current density occurred in region III, which signals that the anodization reached the interface of top Ti/Au and breakdown events began. A series of experiments showed that optimized $TiO_2$ nanotube array was obtained if the sample was removed from the electrolyte at the end of region II, otherwise extended anodization led to the deposited film peeling off from Co-28Cr-6Mo substrate. In this work, higher concentration of $NH_4F$ in the electrolyte reduced the anodization time required to arrive at the end of region II.

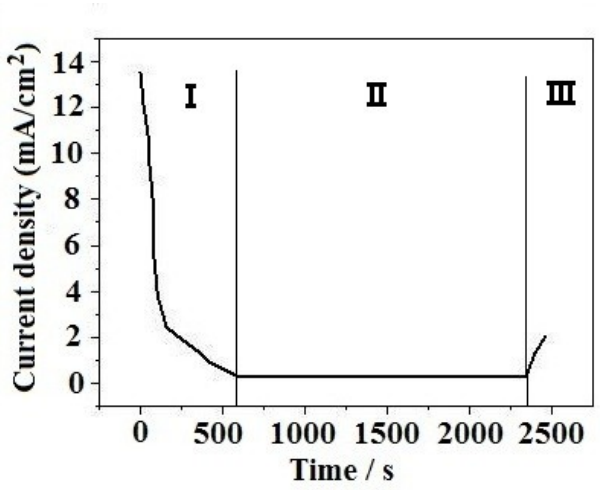


**Figure 5.2-2.** Corresponding current density vs. anodization time curve of anodization process of Ti/Au/Ti trilayer at 400 °C (divided into three regions).

### *5.2.2.2 Effect of deposition temperature*

**Figure 5.2-3** shows the SEM images of the as-deposited surface morphology of the Ti/Au/Ti thin film on forged Co-28Cr-6Mo alloy sputtered at 400 °C **(a)** and room temperature **(b)**. From **Figure 5.2-3(a)** and **Figure 5.2-3(a)**, it is obvious that the morphology of the Ti films sputtered at 400 °C and at room temperature is different. The surface of the Ti/Au/Ti thin film sputtered at 400 °C is compact, with polygonal plate-like structures on the scale of 150-200 nm (**Figure 5.2-3(a)**). The surface of the Ti/Au/Ti thin film sputtered at room temperature (**Figure 5.2-3(b)**) consists of angular grain structures on the scale of 200-300 nm, which is larger than those observed at 400 °C. In addition, the room temperature film is loose, with larger spaces between grains.

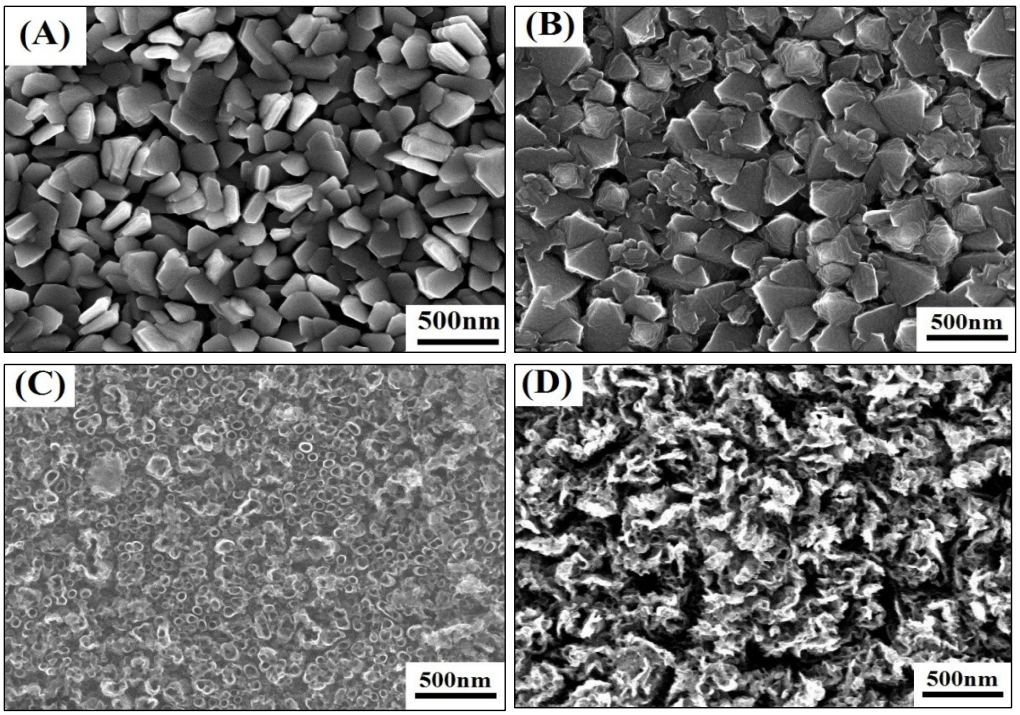


**Figure 5.2-3.** The SEM images of the surface morphology of Ti/Au/Ti thin film on forged Co-28Cr-6Mo alloy disc samples sputtered at different deposition temperature: **(A)** at 400 °C, **(B)** at room temperature; and the surface SEM images of $TiO_2$ nanotube arrays anodized Ti/Au/Ti thin film on Co-28Cr-6Mo alloy disc samples sputtered at different deposition temperature: **(C)** at 400 °C, **(D)** at room temperature.

The surface morphologies of the corresponding $TiO_2$ nanotube arrays obtained by anodizing these films under the same anodizing conditions are shown in **Figure 5.2-3(c)** and **(d)**. **Figure 5.2-3(c)** shows the $TiO_2$ nanotube arrays obtained by anodizing the Ti/Au/Ti thin film deposited on Co-28Cr-6Mo alloy at 400 °C in glycerol solution containing 3.0 wt% $NH_4F$ and 5 vol% $H_2O$ at 20 V. The diameter of $TiO_2$ nanotubes is ~45-55 nm. The surface morphology of Ti/Au/Ti thin film deposited at room temperature after anodization is shown in **Figure 5.2-3(d)**. Some nanoholes and cracks are distributed on the surface, and $TiO_2$ nanotube morphology

does not appear to be present. Obviously, the structure of sputtered film effects the growth of the $TiO_2$ nanotube. Compact, smooth and uniform sputtered films favor the formation of $TiO_2$ nanotubes. For the cast Co-28Cr-6Mo substrate, the influence of deposition temperature on the structure of Ti thin film is the same as the forged Co-28Cr-6Mo substrate.

#### *5.2.2.3 Effect of electrolyte content*

The influence of $NH_4F$ concentration and $H_2O$ concentration in electrolyte on the formation of $TiO_2$ nanotube by anodizing the Ti/Au/Ti trilayer deposited on forged Co-28Cr-6Mo substrate at 400 de was investigated**. Figure 5.2-4** shows top-view SEM images of the layers grown in glycerol electrolyte containing 5 vol% $H_2O$ with different $NH_4F$ contents from 2.0 wt% to 5.0 wt%. A few $TiO_2$ nanotubes can be observed in the 2.0 wt% $NH_4F$ containing electrolyte, but almost the whole surface was covered by non-etched topmost layer (**Figure 5.2-4(a)**). A nanotubular oxide layer with an average tube diameter of 40-60 nm and a layer thickness of approximately 300-400 nm is formed in the 2.5 wt% $NH_4F$ containing electrolyte (in **Figure 5.2-4(b)**). However, some residual debris still existed on the surface. Anodization in electrolyte with 3.0 wt% $NH_4F$ (**Figure 5.2-4(c)**) leads to a complete removal of the covering layer, revealing uniformly opened nanotubes with an average tube diameter of 40-60 nm and a layer thickness of 300-400 nm. These observations can be

explained by the higher etch rate of the system with increasing $NH_4F$ content in the electrolyte, which can result in a complete and homogeneous dissolution of the topmost oxide layer cover. After anodization in 4.0 wt% $NH_4F$, although the $TiO_2$ nanotubes were also obtained, the space between nanotubes becomes large and the nanotubes were ruined slightly, appearing over-etched (**Figure 5.2-4(d)**). When the content of $NH_4F$ was 5.0 wt% (**Figure 5.2-4(e)**), the surface was etched badly and a small quantity of disordered $TiO_2$ nanotubes existed.

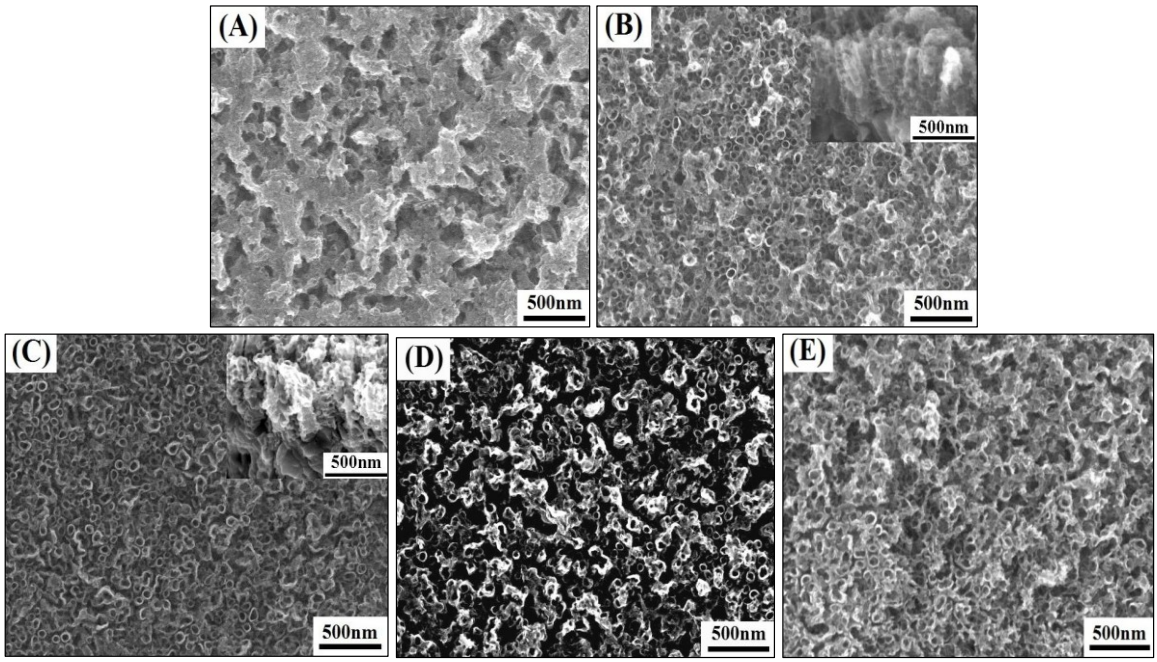


**Figure 5.2-4.** The surface SEM images of Ti/Au/Ti thin film on forged Co-28Cr-6Mo alloy disc samples sputtered at 400 °C after anodization in 5 vol% $H_2O$ and 95 vol% glycerol including different content of $NH_4F$: **(A)** 2.0 wt%, **(B)** 2.5 wt%, **(C)** 3.0 wt%, **(D)** 4.0 wt%, **(E)** 5.0 wt%. The insets depict cross-sectional views.

**Figure 5.2-5** shows the SEM micrographs of the layers grown in glycerol electrolytes containing 2.5 wt% $NH_4F$ with different water contents ranging from 2.5 vol% to 7 vol%. In electrolytes with 2.5 vol% $H_2O$, the

surface is rough and disordered nanoholes exist on the surface (**Figure 5.2-5(a)**). When the content of $H_2O$ is approximately 5 vol%, ordered $TiO_2$ nanotube arrays can be obtained, however partial residual debris is still present on the surface (**Figure 5.2-5(b)**). In electrolytes containing 6 vol% $H_2O$ (**Figure 5.2-5(c)**), uniformly opened nanotubes with an average tube diameter of 50-70 nm are visible. When the film was anodized in 7 vol% $H_2O$, the surface appears to have nanoholes distributed on the surface (**Figure 5.2-5(d)**); however the cross-sectional view (inset) indicates that a nanotube architecture with ~100 nm length was formed under the nanohole surface.

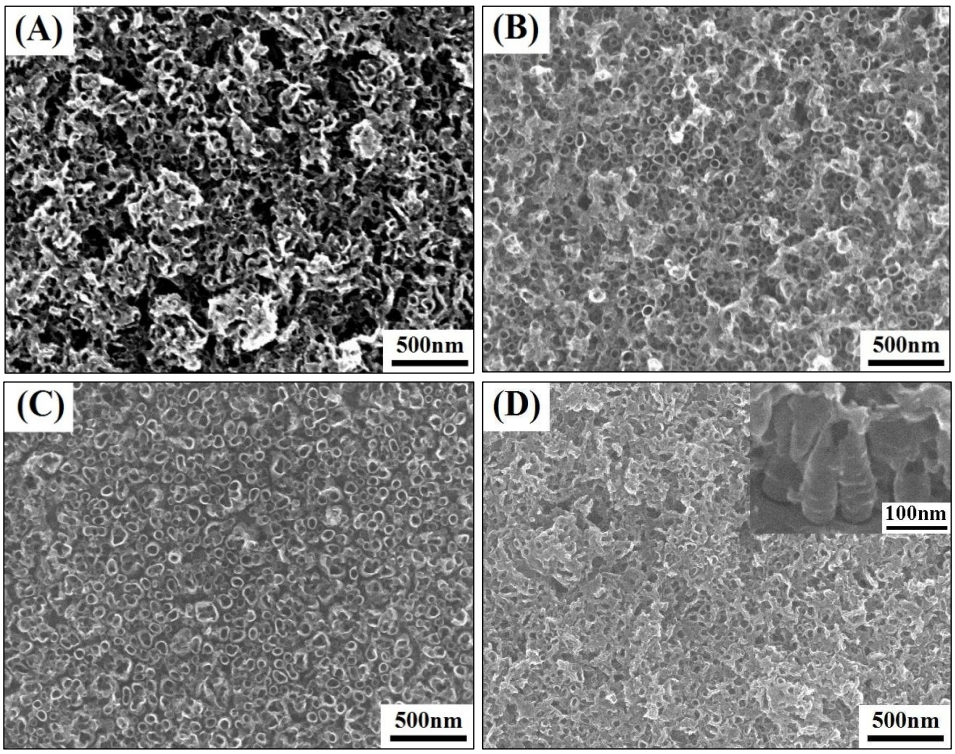


**Figure 5.2-5.** The surface SEM images of Ti/Au/Ti thin film on forged Co-28Cr-6Mo alloy sputtered at 400 °C after anodization in 2.5 wt% $NH_4F$ and 95 vol% glycerol including different content of $H_2O$: **(A)** 2.5 vol%, **(B)** 5 vol%, **(C)** 6 vol%, **(D)** 7 vol%. The insets depict cross-sectional views.

Thus, an increase in $NH_4F$ and $H_2O$ concentration successively leads to an etching of the topmost layer until the nanotubes are completely open. For anodization of the Ti/Au/Ti trilayer deposited on the forged Co-28Cr-6Mo substrate at 400 °C, the optimized electrolyte content was determined to be: 2.5-4.0 wt% $NH_4F$ and 5-6 vol% $H_2O$ in glycerol. Similarly, for anodization of the Ti/Au/Ti trilayer deposited onto the cast Co-28Cr-6Mo substrate at 400 °C, the optimized electrolyte content was determined to be: 2.0 wt% $NH_4F$ and 2.5 vol% $H_2O$ in glycerol.

#### *5.2.2.4 Osteoblast cell response*

Once the optimal conditions were determined for nanotube formation on the surface of the CoCr alloy, the initial response of osteoblast cells to the surface was investigated. In order to assess the biocompatibility of the surfaces and to compare the cellular response to the flat CoCr alloy and $TiO_2$ nanotube coated CoCr alloy, human osteoblast (HOb) cells were cultured on the substrates for 24 hours. The ability of the cells to attach and grow on a medical implant surface is important for initial *in vitro* testing. The cell morphology of attached cells was examined by SEM imaging, which is presented in **Figure 5.2-6**. At lower magnification, the cells appear very flat and well-spread on the CoCr alloy surface (**Figure 5.2-6(a)**). In contrast, the cells on the $TiO_2$ nanotube surface show extensive elongation and cellular extensions (**Figure 5.2-6(b)**), which is characteristic of the typical cell behavior on $TiO_2$ nanotube architectures [188]. The presence of many filopodia is evident on both surfaces (**Figure 5.2-6 (c and d)**). However, at high magnification, the cells on the nanotube surface show prominent filopodia with large areas adhered to the surface in contrast to the fine filopodia fibers on the CoCr surface. Cell flipodia have been shown to "sense" biomaterial surface topographies, and play an important role in cell movement and attachment [41]. Importantly, filopodia have been suggested to first sense

the surface, and then form focal adhesions which allow the cells to firmly adhere to the surface [189]. Since osteoblasts are anchor-dependent cells, the formation of focal adhesions is vital for proper cell function [190], and altered focal adhesion-cytoskeleton assembly has been linked to differing cell phenotype in osteoblastic cells [191]. The large areas at the ends of the filopodia observed on the nanotube surface in **Figure 5.2-6(D)** are speculated to be focal adhesions. Further studies require fluorescent staining of actin and vinculin in order to confirm this speculation.

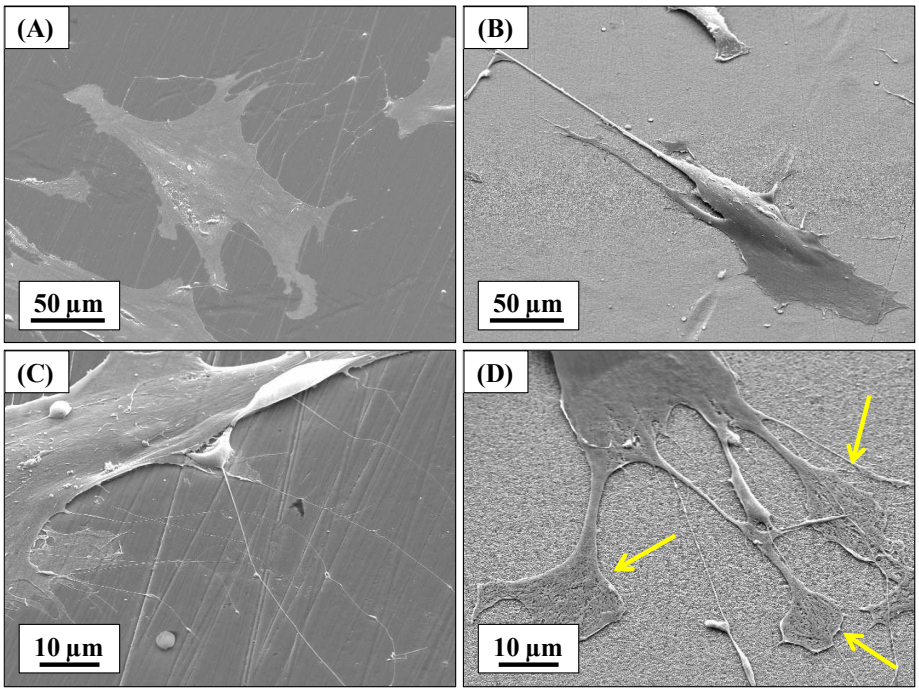


**Figure 5.2-6.** SEM micrographs of HOb cells after 24 h incubation on the flat CoCr substrate (A and C) and $TiO_2$ nanotube substrate (B and D). Image **(B)** indicates cell elongation in response to the nano topography; image **(D)** shows extensive filopodia activity on the nanotube surface (yellow arrows).

The initial osteoblast cell response to the $TiO_2$ nanotube coated CoCr alloy in this study appears to be similar to the response to $TiO_2$

nanotube surfaces in prior studies, and extensive filopodia activity indicates a high response to the nanotube topography. These primary studies indicate the potential applicability of this coating for bone implant use. However, extensive in vitro analysis is required to assess the cell viability and functionality after longer incubation times. These studies are ongoing, and will be published in future work.

### 5.2.3 Conclusion

The intention of this study was to investigate the feasibility of applying anodized $TiO_2$ nanotube films onto CoCr alloy medical implants for next-generation osseointegrative surfaces. Further investigations are necessary to more completely assess the biocompatibility and biological response of osteoblast cells to the nanotube surface, as well as in-depth analysis of the quality of the $TiO_2$ nanotube film in terms of adhesion strength and mechanical stability. *In vitro* osteoblast studies will be published in future work.

In the present work, DC sputtered titanium thin films deposited onto forged and cast Co-28Cr-6Mo substrates at 400 °C and room temperature have been anodized and studied. The study shows that depositing a Ti/Au/Ti trilayer thin film enables for better anodization control and thus optimal nanotube morphology. In addition, it was found that films sputtered at an elevated temperature are favorable for the formation of

well-ordered nanotubes, most likely due to the smaller grain size and more compact nature of the film. The effects of electrolyte concentration were also investigated and the optimized experimental parameters were obtained. This work contains meaningful results for the application of a $TiO_2$ nanotube coating to a CoCr alloy implant for the purpose of enhancing bone formation and bone in-growth for more stable orthopedic implants. In addition, the findings of this study are beneficial to furthering the understanding of electrochemical anodization of Ti thin films, especially on unique substrates such as medical grade alloys. The investigation of the formation of thin film $TiO_2$ nanotube coatings on metallic alloy substrates offers significant advancement in the potential applicability of such nanotube architectures.

## 5.3 Conclusions and Future Directions

The work presented in this chapter demonstrates the feasibility of applying thin film $TiO_2$ nanotubes to the surface of an alternative biomedical implant material for enhanced biological fixation. The anodization process for such thin film coatings requires unique electrolyte concentrations, as well as process parameters that have been optimized for demonstration of principle. Differences in the underlying substrate material (i.e. ceramic versus metal) require extensive optimization in order

for nanotube formation to be achieved. In addition, brief *in vitro* osteoblast experiments were conducted to portray biocompatibility and cell adhesion ability. These results have exciting implications for the application of the nanotube structure to an orthopedic implant for a bioactive coating.

Although the preliminary results are promising, further research is necessary in order to prove the *in vitro* and *in vivo* compatibility and osteogenic behavior on these surfaces. In addition to biological experiments, extensive analysis of the quality and properties of the nanotube thin film are required to determine whether they are suitable for load-bearing orthopedic implant applications.

*Chapter 5, section 1 contains a reprint in part of the material as it has been prepared for submission for publication, written by Christine J. Frandsen, Kunbae Noh, Karla S. Brammer, and Sungho Jin. The dissertation author is the primary investigator and author of this publication. Chapter 5, section 2 contains a reprint in part of the material as it has been prepared for submission for publication, written by Jiahua Ni, Christine J. Frandsen, Kunbae Noh, Gary W. Johnston, Guo He, Tingting Tang, and Sungho Jin. The dissertation author is the primary collaborating investigator and author of this publication.*

# CHAPTER 6

## 6. Closing Remarks

In this work, various nanotube architectures were prepared, characterized, and altered using standard materials science techniques. The surfaces were then analyzed using standard *in vitro* biological assay techniques in order to assess osteoblast cell compatibility and function in response to the unique surfaces. The findings presented in this dissertation provide exciting evidence towards engineering nanostructured biomaterial surfaces for the eventual goal of encouraging rapid osseointegration of orthopedic implants.

A good share of current research in the orthopedics industry has been concentrated on advanced surface technologies that would instigate biological fixation, enhancing patient healing time and reducing chance for aseptic loosening. An increasing number of studies have shown that cells respond to minute changes in surface characteristics as discussed in this dissertation. The ideal orthopedic material surface would be composed of a unique combination of surface properties that would promote the optimum environment for bone in-growth and implant fixation.

It is apparent that the nanotube architecture is capable of strongly affecting cell behavior, and that even minute changes in the nanotube

surface can have substantial results. The fact that such a small range of dimensions as 30-100 nm diameter pore openings can alter cell functionality has great promise for researchers in the field of bone regeneration. Furthermore, the differing cellular preferences for various surface chemistry/nanotopography combinations demonstrated in this work indicate the potential for utilizing unique combinations of topography and chemistry to tailor a medical implant surface to a particular tissue type. Such an implant coating would provide "smart" biomaterials surfaces that interact with a tissue in predefined ways, thus encouraging the appropriate tissue response. In addition, it is possible that a single implant could have particular sections of the surface engineered for different tissue/cell types, similarly to the way current implants are created. For example, femoral knee implants today have smooth and rough surfaces, each designed for the particular purpose of that section of implant (i.e. bone in-growth versus articulating surface). A possible future implant would have areas of combined surface chemistry/nanotopography designed for mesenchymal stem cell recruitment, while another area geared towards osteoblast cell growth, and possibly another for chondrocyte growth. Thus, a single implant would be designed to recruit different cell types to different areas, enabling each particular area to have the best tissue interaction for that

section of the human joint. This kind of multi-faceted surface engineered for particular cell recruitment would revolutionize the field of regenerative medicine for orthopedic implant devices.

In conclusion, the research of this dissertation conveys substantial contributions towards the field of orthopedic surface technology, and for furthered understanding of cellular interactions with complex nano-interfaces. With greater insight into engineering nanoscale surfaces that guide cell response, next-generation orthopedic implants are in closer and more prominent view.

# CHAPTER 7

# 7. References


1. Oh, S., et al., *Significantly accelerated osteoblast cell growth on aligned TiO2 nanotubes.* Journal of Biomedical Materials Research Part A, 2006. **78A**(1): p. 97-103.

2. Brammer, K.S., et al., *Improved bone-forming functionality on diameter-controlled TiO(2) nanotube surface.* Acta Biomater, 2009. **5**(8): p. 3215-23.

3. Oh, S., et al., *Stem cell fate dictated solely by altered nanotube dimension.* Proc Natl Acad Sci U S A, 2009. **106**(7): p. 2130-5.

4. Matassi, F., et al., *New biomaterials for bone regeneration.* Clin Cases Miner Bone Metab, 2011. **8**(1): p. 21-4.

5. Clarke, B., *Normal bone anatomy and physiology.* Clin J Am Soc Nephrol, 2008. **3 Suppl 3**: p. S131-9.

6. Albrektsson, T. and C. Johansson, *Osteoinduction, osteoconduction and osseointegration.* Eur Spine J, 2001. **10 Suppl 2**: p. S96-101.

7. Hench, L.L., D.L. Wheeler, and D.C. Greenspan, *Molecular control of bioactivity in sol-gel glasses.* Journal of Sol-Gel Science and Technology, 1998. **13**(1-3): p. 245-250.

8. Sun, H.L., et al., *Failure rates of short (</= 10 mm) dental implants and factors influencing their failure: a systematic review.* Int J Oral Maxillofac Implants, 2011. **26**(4): p. 816-25.

9. Sato, M. and T.J. Webster, *Nanobiotechnology: implications for the future of nanotechnology in orthopedic applications.* Expert Rev Med Devices, 2004. **1**(1): p. 105-14.

10. Hench, L.L. and J.M. Polak, *Third-generation biomedical materials.* Science, 2002. **295**(5557): p. 1014-+.

11. Stevens, M.M. and J.H. George, *Exploring and engineering the cell surface interface.* Science, 2005. **310**(5751): p. 1135-8.

12. Perez-Sanchez, M.J., et al., *Biomaterials for bone regeneration.* Med Oral Patol Oral Cir Bucal, 2010. **15**(3): p. e517-22.

13. McMahon, S., et al., *In vivo response of bone defects filled with PMMA in an ovine model.* Hip Int, 2011. **21**(5): p. 616-22.

14. Tabassum, A., et al., *Influence of surgical technique and surface roughness on the primary stability of an implant in artificial bone with different cortical thickness: a laboratory study.* Clin Oral Implants Res, 2010. **21**(2): p. 213-20.

15. Schuh, A., et al., *Second generation (low modulus) titanium alloys in total hip arthroplasty.* Materialwissenschaft Und Werkstofftechnik, 2007. **38**(12): p. 1003-1007.

16. Hay, E.D., *Cell biology of extracellular matrix*. 2nd ed. 1991, New York: Plenum Press. 468.

17. Christenson, E.M., et al., *Nanobiomaterial applications in orthopedics.* Journal of Orthopaedic Research, 2007. **25**(1): p. 11-22.

18. Campbell, N.A., J.B. Reece, and R.T. Taylor, *Biology: Concepts and Connections*. 5th ed. 2008, San Francisco: Pearson/Benjamin Cummings. 783.

19. Cooper, L.F., *Biologic determinants of bone formation for osseointegration: clues for future clinical improvements.* J Prosthet Dent, 1998. **80**(4): p. 439-49.

20. Nanci, A., et al., *Chemical modification of titanium surfaces for covalent attachment of biological molecules.* J Biomed Mater Res, 1998. **40**(2): p. 324-35.

21. Boyan, B.D., Z. Schwartz, and J.C. Hambleton, *Response of bone and cartilage cells to biomaterials in vivo and in vitro.* J Oral Implantol, 1993. **19**(2): p. 116-22; discussion 136-7.

22. Schwartz, Z., et al., *Modulation of matrix vesicle enzyme activity and phosphatidylserine content by ceramic implant materials during endosteal bone healing.* Calcif Tissue Int, 1992. **51**(6): p. 429-37.

23. Isa, Z.M., et al., *Effects of fluoride-modified titanium surfaces on osteoblast proliferation and gene expression.* Int J Oral Maxillofac Implants, 2006. **21**(2): p. 203-11.

24. Meirelles, L., et al., *The effect of chemical and nanotopographical modifications on the early stages of osseointegration.* Int J Oral Maxillofac Implants, 2008. **23**(4): p. 641-7.

25. Deligianni, D.D., et al., *Effect of surface roughness of the titanium alloy Ti-6Al-4V on human bone marrow cell response and on protein adsorption.* Biomaterials, 2001. **22**(11): p. 1241-51.

26. Deligianni, D.D., et al., *Effect of surface roughness of hydroxyapatite on human bone marrow cell adhesion, proliferation, differentiation and detachment strength.* Biomaterials, 2001. **22**(1): p. 87-96.

27. Lampin, M., et al., *Correlation between substratum roughness and wettability, cell adhesion, and cell migration.* J Biomed Mater Res, 1997. **36**(1): p. 99-108.

28. Maroudas, N.G., *Sulphonated polystyrene as an optimal substratum for the adhesion and spreading of mesenchymal cells in monovalent and divalent saline solutions.* J Cell Physiol, 1977. **90**(3): p. 511-9.

29. Schakenraad, J.M., et al., *The influence of substratum surface free energy on growth and spreading of human fibroblasts in the presence and absence of serum proteins.* J Biomed Mater Res, 1986. **20**(6): p. 773-84.

30. Maroudas, N.G., *Adhesion and spreading of cells on charged surfaces.* J Theor Biol, 1975. **49**(2): p. 417-24.

31. Ramsey, W.S., et al., *Surface treatments and cell attachment.* In Vitro, 1984. **20**(10): p. 802-8.

32. Brunette, D.M., *Mechanism of Directed Cell-Migration on Grooved Titanium Substrata.* Journal of Dental Research, 1987. **66**: p. 114-114.

33. Das, K., S. Bose, and A. Bandyopadhyay, *TiO2 nanotubes on Ti: Influence of nanoscale morphology on bone cell-materials interaction.* Journal of Biomedical Materials Research Part A, 2009. **90**(1): p. 225-37.

34. S.Anil, et al., eds. *Dental Implant Surface Enhancement and Osseointegration*. Implant Dentistry - A Rapidly Evolving Practice, ed. I. Turkyilmaz. 2011, InTech. 544.

35. Oshida, Y., et al., *Dental implant systems.* Int J Mol Sci, 2010. **11**(4): p. 1580-678.

36. Wennerberg, A. and T. Albrektsson, *Effects of titanium surface topography on bone integration: a systematic review.* Clin Oral Implants Res, 2009. **20 Suppl 4**: p. 172-84.

37. Fujibayashi, S., et al., *Osteoinduction of porous bioactive titanium metal.* Biomaterials, 2004. **25**(3): p. 443-50.

38. Norman, J.J. and T.A. Desai, *Methods for fabrication of nanoscale topography for tissue engineering scaffolds.* Ann Biomed Eng, 2006. **34**(1): p. 89-101.

39. Junker, R., et al., *Effects of implant surface coatings and composition on bone integration: a systematic review.* Clin Oral Implants Res, 2009. **20 Suppl 4**: p. 185-206.

40. Dalby, M.J., et al., *Investigating filopodia sensing using arrays of defined nano-pits down to 35 nm diameter in size.* Int J Biochem Cell Biol, 2004. **36**(10): p. 2005-15.

41. Dalby, M.J., et al., *Investigating the limits of filopodial sensing: a brief report using SEM to image the interaction between 10 nm high nano-topography and fibroblast filopodia.* Cell Biol Int, 2004. **28**(3): p. 229-36.

42. Gong, D., et al., *Titanium oxide nanotube arrays prepared by anodic oxidation.* Journal of Materials Research, 2001. **16**(12): p. 3331-3334.

43. Mor, G.K., et al., *A review on highly ordered, vertically oriented TiO2 nanotube arrays: Fabrication, material properties, and solar energy applications.* Solar Energy Materials and Solar Cells, 2006. **90**(14): p. 2011-2075.

44. Macak, J.M., et al., *TiO2 nanotubes: Self-organized electrochemical formation, properties and applications.* Current Opinion in Solid State & Materials Science, 2007. **11**(1-2): p. 3-18.

45. Lee, W.J. and W.H. Smyrl, *Zirconium oxide nanotubes synthesized via direct electrochemical anodization.* Electrochemical and Solid State Letters, 2005. **8**(3): p. B7-B9.

46. Sieber, I., et al., *Formation of self-organized niobium porous oxide on niobium.* Electrochemistry Communications, 2005. **7**(1): p. 97-100.

47. Choi, J.S., et al., *Porous niobium oxide films prepared by anodization in HF/H3PO4.* Electrochimica Acta, 2006. **51**(25): p. 5502-5507.

48. Choi, J., et al., *Porous niobium oxide films prepared by anodization-annealing-anodization.* Nanotechnology, 2007. **18**(5).

49. Karlinsey, R.L., *Preparation of self-organized niobium oxide microstructures via potentiostatic anodization.* Electrochemistry Communications, 2005. **7**(12): p. 1190-1194.

50. Tsuchiya, H., et al., *Self-organized porous WO3 formed in NaF electrolytes.* Electrochemistry Communications, 2005. **7**(3): p. 295-298.

51. Berger, S., et al., *High photocurrent conversion efficiency in self-organized porous WO3.* Applied Physics Letters, 2006. **88**(20).

52. Tsuchiya, H. and P. Schmuki, *Self-organized high aspect ratio porous hafnium oxide prepared by electrochemical anodization.* Electrochemistry Communications, 2005. **7**(1): p. 49-52.

53. Allam, N.K., X.J. Feng, and C.A. Grimes, *Self-Assembled Fabrication of Vertically Oriented Ta2O5 Nanotube Arrays, and Membranes Thereof, by One-Step Tantalum Anodization.* Chemistry of Materials, 2008. **20**(20): p. 6477-6481.

54. Sieber, I., B. Kannan, and P. Schmuki, *Self-assembled porous tantalum oxide prepared in H2SO4/HF electrolytes.* Electrochemical and Solid State Letters, 2005. **8**(3): p. J10-J12.

55. Sieber, I.V. and P. Schmuki, *Porous tantalum oxide prepared by electrochemical anodic oxidation.* Journal of the Electrochemical Society, 2005. **152**(9): p. C639-C644.

56. El-Sayed, H., et al., *Formation of highly ordered arrays of dimples on tantalum at the nanoscale.* Nano Letters, 2006. **6**(12): p. 2995-2999.

57. Zwilling, V., et al., *Structure and physicochemistry of anodic oxide films on titanium and TA6V alloy.* Surface and Interface Analysis, 1999. **27**(7): p. 629-637.

58. Beranek, R., H. Hildebrand, and P. Schmuki, *Self-organized porous titanium oxide prepared in H2SO4/HF electrolytes.* Electrochemical and Solid State Letters, 2003. **6**(3): p. B12-B14.

59. Macak, J.M., K. Sirotna, and P. Schmuki, *Self-organized porous titanium oxide prepared in Na2SO4/NaF electrolytes.* Electrochimica Acta, 2005. **50**(18): p. 3679-3684.

60. Macak, J.M., H. Tsuchiya, and P. Schmuki, *High-aspect-ratio TiO2 nanotubes by anodization of titanium.* Angewandte Chemie-International Edition, 2005. **44**(14): p. 2100-2102.

61. Ghicov, A., et al., *Titanium oxide nanotubes prepared in phosphate electrolytes.* Electrochemistry Communications, 2005. **7**(5): p. 505-509.

62. Ruan, C.M., et al., *Fabrication of highly ordered TiO2 nanotube arrays using an organic electrolyte.* Journal of Physical Chemistry B, 2005. **109**(33): p. 15754-15759.

63. Macak, J.M., et al., *Smooth anodic TiO2 nanotubes.* Angewandte Chemie-International Edition, 2005. **44**(45): p. 7463-7465.

64. Taveira, L.V., et al., *Initiation and growth of self-organized TiO2 nanotubes anodically formed in NH4F/(NH4)(2)SO4 electrolytes.* Journal of the Electrochemical Society, 2005. **152**(10): p. B405-B410.

65. Wang, D.A., et al., *TiO2 Nanotubes with Tunable Morphology, Diameter, and Length: Synthesis and Photo-Electrical/Catalytic Performance.* Chemistry of Materials, 2009. **21**(7): p. 1198-1206.

66. Shin, Y. and S. Lee, *Self-Organized Regular Arrays of Anodic TiO2 Nanotubes.* Nano Letters, 2008. **8**(10): p. 3171-3173.

67. Oh, S.H., et al., *Growth of nano-scale hydroxyapatite using chemically treated titanium oxide nanotubes.* Biomaterials, 2005. **26**(24): p. 4938-43.

68. Baowan, D., W. Triampo, and D. Triampo, *Encapsulation of TiO2 nanoparticles into single-walled carbon nanotubes.* New Journal of Physics, 2009. **11**.

69. He, J., et al., *The anatase phase of nanotopography titania plays an important role on osteoblast cell morphology and proliferation.* Journal of Materials Science-Materials in Medicine, 2008. **19**(11): p. 3465-3472.

70. Maniotis, A.J., C.S. Chen, and D.E. Ingber, *Demonstration of mechanical connections between integrins, cytoskeletal filaments, and nucleoplasm that stabilize nuclear structure.* Proc Natl Acad Sci U S A, 1997. **94**(3): p. 849-54.

71. Getzenberg, R.H., et al., *Nuclear structure and the three-dimensional organization of DNA.* J Cell Biochem, 1991. **47**(4): p. 289-99.

72. Yoriya, S. and C.A. Grimes, *Self-Assembled TiO2 Nanotube Arrays by Anodization of Titanium in Diethylene Glycol: Approach to Extended Pore Widening.* Langmuir, 2010. **26**(1): p. 417-420.

73. Bauer, S., et al., *Size selective behavior of mesenchymal stem cells on ZrO(2) and TiO(2) nanotube arrays.* Integr Biol (Camb), 2009. **1**(8-9): p. 525-32.

74. Brammer, K.S., et al., *Comparative cell behavior on carbon-coated TiO2 nanotube surfaces for osteoblasts vs. osteo-progenitor cells.* Acta Biomater, 2011. **7**(6): p. 2697-703.

75. Berger, S., et al., *Enhanced self-ordering of anodic ZrO2 nanotubes in inorganic and organic electrolytes using two-step anodization.* Physica Status Solidi-Rapid Research Letters, 2008. **2**(3): p. 102-104.

76. Oliveira, N.T., et al., *Electrochemical studies on zirconium and its biocompatible alloys Ti-50Zr at.% and Zr-2.5Nb wt.% in simulated physiologic media.* Journal of Biomedical Materials Research Part A, 2005. **74**(3): p. 397-407.

77. Kobayashi, E., et al., *Mechanical properties of the binary titanium-zirconium alloys and their potential for biomedical materials.* J Biomed Mater Res, 1995. **29**(8): p. 943-50.

78. Bourne, R.B., et al., *Arthroplasty options for the young patient: Oxinium on cross-linked polyethylene.* Clin Orthop Relat Res, 2005. **441**: p. 159-67.

79. Hunter, G., et al., *Creation of oxidized zirconium orthopaedic implants.* Journal of ASTM International, 2005. **2**(7): p. 16-29.

80. *2004 Annual Report*. 2005: London, England. p. 1-161.

81. Oh, S. and S. Jin, *Titanium oxide nanotubes with controlled morphology for enhanced bone growth.* Materials Science & Engineering C-Biomimetic and Supramolecular Systems, 2006. **26**(8): p. 1301-1306.

82. Bjursten, L.M., et al., *Titanium dioxide nanotubes enhance bone bonding in vivo.* Journal of Biomedical Materials Research Part A, 2010. **92**(3): p. 1218-24.

83. Webster, T.J., et al., *Specific proteins mediate enhanced osteoblast adhesion on nanophase ceramics.* J Biomed Mater Res, 2000. **51**(3): p. 475-83.

84. Anselme, K., *Osteoblast adhesion on biomaterials.* Biomaterials, 2000. **21**(7): p. 667-81.

85. Kim, D., et al., *Capillary effects, wetting behavior and photo-induced tube filling of TiO2 nanotube layers.* Nanotechnology, 2008. **19**(30): p. -.

86. Sabirianov, R.F., A. Rubinstein, and F. Namavar (2010) *Enhanced initial protein adsorption on engineered nanostructured cubic zirconia*. arXiv.org, 13.

87. Biggs, M.J., et al., *The effects of nanoscale pits on primary human osteoblast adhesion formation and cellular spreading.* J Mater Sci Mater Med, 2007. **18**(2): p. 399-404.

88. Dalby, M.J., et al., *Initial attachment of osteoblasts to an optimised HAPEX topography.* Biomaterials, 2002. **23**(3): p. 681-90.

89. Ishaug, S.L., et al., *Osteoblast function on synthetic biodegradable polymers.* J Biomed Mater Res, 1994. **28**(12): p. 1445-53.

90. Popat, K.C., et al., *Influence of engineered titania nanotubular surfaces on bone cells.* Biomaterials, 2007. **28**(21): p. 3188-97.

91. Brammer, K.S., et al., *Enhanced cellular mobility guided by TiO2 nanotube surfaces.* Nano Lett, 2008. **8**(3): p. 786-93.

92. Guo, L., et al., *Bioactivity of zirconia nanotube arrays fabricated by electrochemical anodization.* Materials Science & Engineering C, 2008. **29**(4): p. 1174-77.

93. Sista, S., et al., *The influence of surface energy of titanium-zirconium alloy on osteoblast cell functions in vitro.* J Biomed Mater Res A, 2011.

94. Dalby, M.J., *Topographically induced direct cell mechanotransduction.* Med Eng Phys, 2005. **27**(9): p. 730-42.

95. Dalby, M.J., *Cellular response to low adhesion nanotopographies.* Int J Nanomedicine, 2007. **2**(3): p. 373-81.

96. Dalby, M.J., *Nanostructured surfaces: cell engineering and cell biology.* Nanomedicine (Lond), 2009. **4**(3): p. 247-8.

97. Curtis, A. and C. Wilkinson, *New depths in cell behaviour: reactions of cells to nanotopography.* Biochem Soc Symp, 1999. **65**: p. 15-26.

98. Srivastav, A., *An Overview of Metallic Biomaterials for Bone Support and Replacement*, in *Biomedical Engineering, Trends in Materials Science*, A.N. Laskovski, Editor. 2011, InTech.

99. Sul, Y.T., et al., *The bone response of oxidized bioactive and non-bioactive titanium implants.* Biomaterials, 2005. **26**(33): p. 6720-30.

100. Meyer, U., et al., *Basic reactions of osteoblasts on structured material surfaces.* Eur Cell Mater, 2005. **9**: p. 39-49.

101. Rodil, S.E., et al., *Properties of carbon films and their biocompatibility using in-vitro tests.* Diamond and Related Materials, 2003. **12**(3-7): p. 931-937.

102. Cui, F.Z. and D.J. Li, *A review of investigations on biocompatibility of diamond-like carbon and carbon nitride films.* Surface & Coatings Technology, 2000. **131**(1-3): p. 481-487.

103. Cui, F.Z., et al., *Biomedical investigations on CNx coating.* Surface & Coatings Technology, 2005. **200**(1-4): p. 1009-1013.

104. Amaral, M., et al., *Nanocrystalline diamond: In vitro biocompatibility assessment by MG63 and human bone marrow cells cultures.* Journal of Biomedical Materials Research Part A, 2008. **87A**(1): p. 91-99.

105. Amaral, M., et al., *Cytotoxicity evaluation of nanocrystalline diamond coatings by fibroblast cell cultures.* Acta Biomaterialia, 2009. **5**(2): p. 755-763.

106. Chai, F., et al., *Osteoblast interaction with DLC-coated Si substrates.* Acta Biomaterialia, 2008. **4**(5): p. 1369-1381.

107. Ismail, F.S.M., et al., *The influence of surface chemistry and topography on the contact guidance of MG63 osteoblast cells.* Journal of Materials Science-Materials in Medicine, 2007. **18**(5): p. 705-714.

108. Lechleitner, T., et al., *The surface properties of nanocrystalline diamond and nanoparticulate diamond powder and their suitability as cell growth support surfaces.* Biomaterials, 2008. **29**(32): p. 4275-4284.

109. Yang, L., B.W. Sheldon, and T.J. Webster, *Orthopedic nano diamond coatings: Control of surface properties and their impact on osteoblast adhesion and proliferation.* Journal of Biomedical Materials Research Part A, 2009. **91A**(2): p. 548-556.

110. Kalbacova, M., et al., *Nanoscale topography of nanocrystalline diamonds promotes differentiation of osteoblasts.* Acta Biomaterialia, 2009. **5**(8): p. 3076-3085.

111. Benoit, D.S., A.R. Durney, and K.S. Anseth, *The effect of heparin-functionalized PEG hydrogels on three-dimensional human mesenchymal stem cell osteogenic differentiation.* Biomaterials, 2007. **28**(1): p. 66-77.

112. Mirmalek-Sani, S.H., et al., *Characterization and multipotentiality of human fetal femur-derived cells: implications for skeletal tissue regeneration.* Stem Cells, 2006. **24**(4): p. 1042-53.

113. Boyan, B.D., et al., *Role of material surfaces in regulating bone and cartilage cell response.* Biomaterials, 1996. **17**(2): p. 137-46.

114. Black, J., *Biological performance of tantalum.* Clin Mater, 1994. **16**(3): p. 167-73.

115. Kato, H., et al., *Bonding of alkali- and heat-treated tantalum implants to bone.* J Biomed Mater Res, 2000. **53**(1): p. 28-35.

116. Balla, V.K., et al., *Direct laser processing of a tantalum coating on titanium for bone replacement structures.* Acta Biomater, 2010. **6**(6): p. 2329-34.

117. Schildhauer, T.A., et al., *Bacterial adherence to tantalum versus commonly used orthopedic metallic implant materials.* J Orthop Trauma, 2006. **20**(7): p. 476-84.

118. Findlay, D.M., et al., *The proliferation and phenotypic expression of human osteoblasts on tantalum metal.* Biomaterials, 2004. **25**(12): p. 2215-27.

119. Roy, M., et al., *Comparison of Tantalum and Hydroxyapatite Coatings on Titanium for Applications in Load Bearing Implants.* Advanced Engineering Materials, 2010. **12**(11): p. B637-B641.

120. Jafari, S.M., et al., *Do Tantalum and Titanium Cups Show Similar Results in Revision Hip Arthroplasty?* Clinical Orthopaedics and Related Research, 2010. **468**(2): p. 459-465.

121. Sagomonyants, K.B., et al., *Porous tantalum stimulates the proliferation and osteogenesis of osteoblasts from elderly female patients.* J Orthop Res, 2011. **29**(4): p. 609-16.

122. Lu, T., Y.Q. Qiao, and X.Y. Liu, *Surface modification of biomaterials using plasma immersion ion implantation and deposition.* Interface Focus, 2012. **2**(3): p. 325-336.

123. Ruckh, T., et al., *Nanostructured tantala as a template for enhanced osseointegration.* Nanotechnology, 2009. **20**(4): p. 045102.

124. Dolatshahi-Pirouz, A., et al., *Fibronectin Adsorption, Cell Adhesion, and Proliferation on Nanostructured Tantalum Surfaces.* Acs Nano, 2010. **4**(5): p. 2874-2882.

125. Oh, S., et al., *Significantly accelerated osteoblast cell growth on aligned TiO2 nanotubes.* J Biomed Mater Res A, 2006. **78**(1): p. 97-103.

126. Bjursten, L.M., et al., *Titanium dioxide nanotubes enhance bone bonding in vivo.* J Biomed Mater Res A, 2010. **92**(3): p. 1218-24.

127. Bauer, S., et al., *Improved attachment of mesenchymal stem cells on super-hydrophobic TiO2 nanotubes.* Acta Biomater, 2008. **4**(5): p. 1576-82.

128. Balla, V.K., et al., *Porous tantalum structures for bone implants: fabrication, mechanical and in vitro biological properties.* Acta Biomater, 2010. **6**(8): p. 3349-59.

129. Stiehler, M., et al., *Morphology, proliferation, and osteogenic differentiation of mesenchymal stem cells cultured on titanium, tantalum, and chromium surfaces.* J Biomed Mater Res A, 2008. **86**(2): p. 448-58.

130. Feng, B., et al., *Characterization of surface oxide films on titanium and adhesion of osteoblast.* Biomaterials, 2003. **24**(25): p. 4663-70.

131. Sharma, C.P. and W. Paul, *Protein interaction with tantalum: changes with oxide layer and hydroxyapatite at the interface.* J Biomed Mater Res, 1992. **26**(9): p. 1179-84.

132. Lian, J.B. and G.S. Stein, *Concepts of osteoblast growth and differentiation: basis for modulation of bone cell development and tissue formation.* Crit Rev Oral Biol Med, 1992. **3**(3): p. 269-305.

133. Owen, T.A., et al., *Progressive development of the rat osteoblast phenotype in vitro: reciprocal relationships in expression of genes associated with osteoblast proliferation and differentiation during formation of the bone extracellular matrix.* J Cell Physiol, 1990. **143**(3): p. 420-30.

134. Martinez, E., et al., *Effects of artificial micro- and nano-structured surfaces on cell behaviour.* Ann Anat, 2009. **191**(1): p. 126-35.

135. Hayashi, M., et al., *In vitro characterization and osteoblast responses to nanostructured photocatalytic TiO2 coated surfaces.* Acta Biomater, 2012. **8**(6): p. 2411-6.

136. Frandsen, C.J., et al., *Zirconium oxide nanotube surface prompts increased osteoblast functionality and mineralization.* Materials Science & Engineering C-Materials for Biological Applications, 2011. **31**(8): p. 1716-1722.

137. Dalby, M.J., et al., *Polymer-demixed nanotopography: control of fibroblast spreading and proliferation.* Tissue Eng, 2002. **8**(6): p. 1099-108.

138. Zigmond, S.H., *Signal transduction and actin filament organization.* Curr Opin Cell Biol, 1996. **8**(1): p. 66-73.

139. Welldon, K.J., et al., *Primary human osteoblasts grow into porous tantalum and maintain an osteoblastic phenotype.* Journal of Biomedical Materials Research Part A, 2008. **84A**(3): p. 691-701.

140. McCafferty, E. and J.P. Wightman, *Determination of the acid-base properties of metal oxide films and of polymers by contact angle measurements.* Journal of Adhesion Science and Technology, 1999. **13**(12): p. 1415-1436.

141. Ross, S. and I.D. Morrison, *Colloidal Dispersions*. 2002, New York: Wiley Interscience.

142. Parfitt, G.D., *Surface-Chemistry of Oxides.* Pure and Applied Chemistry, 1976. **48**(4): p. 415-418.

143. Kaysinger, K.K. and W.K. Ramp, *Extracellular pH modulates the activity of cultured human osteoblasts.* J Cell Biochem, 1998. **68**(1): p. 83-9.

144. Liang, H.-c., X.-z. Li, and J. Nowotny, *Photocatalytical Properties of TiO2 Nanotubes.* Solid State Phenomena, 2010. **162**: p. 295-328.

145. Feng, B., et al., *Characterization of titanium surfaces with calcium and phosphate and osteoblast adhesion.* Biomaterials, 2004. **25**(17): p. 3421-3428.

146. Sul, Y.T., et al., *Oxidized, bioactive implants are rapidly and strongly integrated in bone. Part 1 - experimental implants.* Clinical Oral Implants Research, 2006. **17**(5): p. 521-526.

147. Miyazaki, T., et al., *Induction and acceleration of bonelike apatite formation on tantalum oxide gel in simulated body fluid.* Journal of Sol-Gel Science and Technology, 2001. **21**(1-2): p. 83-88.

148. Yang, Y.Z., R. Cavin, and J.L. Ong, *Protein adsorption on titanium surfaces and their effect on osteoblast attachment.* Journal of Biomedical Materials Research Part A, 2003. **67A**(1): p. 344-349.

149. Moller, K., et al., *The Influence of Zeta-Potential and Interfacial-Tension on Osteoblast-Like Cells.* Cells and Materials, 1994. **4**(3): p. 263-274.

150. Zeng, Q., et al., *Surface modification of titanium implant and in vitro biocompatibility evaluation.* Asbm6: Advanced Biomaterials Vi, 2005. **288-289**: p. 315-318.

151. Gough, J.E., J.R. Jones, and L.L. Hench, *Nodule formation and mineralisation of human primary osteoblasts cultured on a porous bioactive glass scaffold.* Biomaterials, 2004. **25**(11): p. 2039-2046.

152. Kokubo, T., H.M. Kim, and M. Kawashita, *Novel bioactive materials with different mechanical properties.* Biomaterials, 2003. **24**(13): p. 2161-2175.

153. Oh, S.H., et al., *Growth of nano-scale hydroxyapatite using chemically treated titanium oxide nanotubes.* Biomaterials, 2005. **26**(24): p. 4938-4943.

154. Liao, H.H., et al., *Response of rat osteoblast-like cells to microstructured model surfaces in vitro.* Biomaterials, 2003. **24**(4): p. 649-654.

155. Di Silvio, L., M.J. Dalby, and W. Bonfield, *Osteoblast behaviour on HA/PE composite surfaces with different HA volumes.* Biomaterials, 2002. **23**(1): p. 101-107.

156. Cyster, L.A., et al., *The effect of surface chemistry and nanotopography of titanium nitride (TiN) films on 3T3-L1 fibroblasts.* Journal of Biomedical Materials Research Part A, 2003. **67A**(1): p. 138-147.

157. Sharma, C.P. and W. Paul, *Protein-Interaction with Tantalum - Changes with Oxide Layer and Hydroxyapatite at the Interface.* Journal of Biomedical Materials Research, 1992. **26**(9): p. 1179-1184.

158. Donkov, N., Mateev, E, Zykova, A, Safonov, V, and Luk'yanchenko, V, *Biocompatibility of dielectric Ta2O5 coatings in in vitro tests*, in *International Summer School on Vacuum, Electron, and Ion Technologies*. 2010, IOP Publishing.

159. Clarke, I.C., et al., *Current status of zirconia used in total hip implants.* J Bone Joint Surg Am, 2003. **85-A Suppl 4**: p. 73-84.

160. Tsukamoto, R., et al., *Improved wear performance with crosslinked UHMWPE and zirconia implants in knee simulation.* Acta Orthop, 2006. **77**(3): p. 505-11.

161. Chevalier, J., L. Gremillard, and S. Deville, *Low-temperature degradation of Zirconia and implications for biomedical implants.* Annual Review of Materials Research, 2007. **37**: p. 1-32.

162. Blaise, L., F. Villermaux, and B. Cales, *Ageing of zirconia: Everything you always wanted to know.* Bioceramics, 2000. **192-1**: p. 553-556.

163. Gioe, T.J., et al., *Why are total knee replacements revised?: analysis of early revision in a community knee implant registry.* Clin Orthop Relat Res, 2004(428): p. 100-6.

164. Paxton, E.W., et al., *The Kaiser Permanente National Total Joint Replacement Registry.* The Permanente Journal, 2008. **12**(3): p. 5.

165. Sundfeldt, M., et al., *Aseptic loosening, not only a question of wear: a review of different theories.* Acta Orthop, 2006. **77**(2): p. 177-97.

166. Bassett, R.W., *Results of 1,000 Performance knees: cementless versus cemented fixation.* J Arthroplasty, 1998. **13**(4): p. 409-13.

167. Gandhi, R., et al., *Survival and clinical function of cemented and uncemented prostheses in total knee replacement: a meta-analysis.* J Bone Joint Surg Br, 2009. **91**(7): p. 889-95.

168. Khaw, F.M., et al., *A randomised, controlled trial of cemented versus cementless press-fit condylar total knee replacement. Ten-year survival analysis.* J Bone Joint Surg Br, 2002. **84**(5): p. 658-66.

169. Bettinger, C.J., R. Langer, and J.T. Borenstein, *Engineering substrate topography at the micro- and nanoscale to control cell function.* Angew Chem Int Ed Engl, 2009. **48**(30): p. 5406-15.

170. Wang, D., et al., *TiO2 Nanotubes with Tunable Morphology, Diameter, and Length: Synthesis and Photo-Electrical/Catalytic Performance.* Chemistry of Materials, 2009. **21**(7): p. 9.

171. Miyauchi, T., et al., *The enhanced characteristics of osteoblast adhesion to photofunctionalized nanoscale TiO2 layers on biomaterials surfaces.* Biomaterials, 2010. **31**(14): p. 3827-39.

172. Ishizaki, T., N. Saito, and O. Takai, *Correlation of cell adhesive behaviors on superhydrophobic, superhydrophilic, and micropatterned superhydrophobic/superhydrophilic surfaces to their surface chemistry.* Langmuir, 2010. **26**(11): p. 8147-54.

173. Zhao, L., et al., *The influence of hierarchical hybrid micro/nano-textured titanium surface with titania nanotubes on osteoblast functions.* Biomaterials, 2010. **31**(19): p. 5072-82.

174. Yin, H., H. Liu, and W.Z. Shen, *The large diameter and fast growth of self-organized TiO2 nanotube arrays achieved via electrochemical anodization.* Nanotechnology, 2010. **21**(3).

175. Albu, S.P. and P. Schmuki, *TiO2 nanotubes grown in different organic electrolytes: Two-size self-organization, single vs. double-walled tubes, and giant diameters.* Physica Status Solidi-Rapid Research Letters, 2010. **4**(8-9): p. 215-217.

176. Paulose, M., et al., *TiO2 nanotube arrays of 1000 mu m length by anodization of titanium foil: Phenol red diffusion.* Journal of Physical Chemistry C, 2007. **111**(41): p. 14992-14997.

177. Mor, G.K., et al., *Transparent highly ordered TiO2 nanotube arrays via anodization of titanium thin films.* Advanced Functional Materials, 2005. **15**(8): p. 1291-1296.

178. Sadek, A.Z., et al., *Anodization of Ti Thin Film Deposited on ITO.* Langmuir, 2009. **25**(1): p. 509-514.

179. Varghese, O.K., M. Paulose, and C.A. Grimes, *Long vertically aligned titania nanotubes on transparent conducting oxide for highly efficient solar cells.* Nature Nanotechnology, 2009. **4**(9): p. 592-597.

180. Ortiz, G.F., et al., *TiO2 nanotubes manufactured by anodization of Ti thin films for on-chip Li-ion 2D microbatteries.* Electrochimica Acta, 2009. **54**(17): p. 4262-4268.

181. Berger, S., et al., *Transparent TiO2 Nanotube Electrodes via Thin Layer Anodization: Fabrication and Use in Electrochromic Devices.* Langmuir, 2009. **25**(9): p. 4841-4844.

182. Zhang, Z.K., et al., *Fabrication of open-ended TiO2 nanotube arrays by anodizing a thermally evaporated Ti/Au bilayer film.* Applied Surface Science, 2011. **257**(9): p. 4139-4143.

183. Mor, G.K., et al., *Use of highly-ordered TiO2 nanotube arrays in dye-sensitized solar cells.* Nano Letters, 2006. **6**(2): p. 215-218.

184. Yang, D.J., et al., *Vertically oriented titania nanotubes prepared by anodic oxidation on Si substrates.* Ieee Transactions on Nanotechnology, 2008. **7**(2): p. 131-134.

185. Roy, P., S. Berger, and P. Schmuki, *TiO2 Nanotubes: Synthesis and Applications.* Angewandte Chemie-International Edition, 2011. **50**(13): p. 2904-2939.

186. Okazaki, Y. and E. Gotoh, *Comparison of metal release from various metallic biomaterials in vitro.* Biomaterials, 2005. **26**(1): p. 11-21.

187. Katti, K.S., *Biomaterials in total joint replacement.* Colloids and Surfaces B-Biointerfaces, 2004. **39**(3): p. 133-142.

188. Brammer, K.S., et al., *Improved bone-forming functionality on diameter-controlled TiO2 nanotube surface.* Acta Biomaterialia, 2009. **5**(8): p. 3215-3223.

189. Dalby, M.J., et al., *Optimizing HAPEX topography influences osteoblast response.* Tissue Eng, 2002. **8**(3): p. 453-67.

190. Lim, J.Y., et al., *The regulation of integrin-mediated osteoblast focal adhesion and focal adhesion kinase expression by nanoscale topography.* Biomaterials, 2007. **28**(10): p. 1787-97.

191. Lim, J.Y., et al., *Human foetal osteoblastic cell response to polymer-demixed nanotopographic interfaces.* J R Soc Interface, 2005. **2**(2): p. 97-108.